UDK 621.3:(53+54+621+66)(05)(497.1)=00 ISSN 0352-9045

INFORMACIJE MIDEM 1·2010

Strokovno društvo za mikroelektroniko elektronske sestavne dele in materiale

Strokovna revija za mikroelektroniko, elektronske sestavne dele in materiale
Journal of Microelectronics, Electronic Components and Materials

INFORMACIJE MIDEM, LETNIK 40, ŠT. 1(133), LJUBLJANA, marec 2010

UDK 621.3:(53+54+621+66)(05)(497.1)=00 ISSN 0352-9045

INFORMACIJE MIDEM 1 ◦ 2010

INFORMACIJE MIDEM LETNIK 40, ŠT. 1(133), LJUBLJANA, MAREC 2010
INFORMACIJE MIDEM VOLUME 40, NO. 1(133), LJUBLJANA, MARCH 2010

Revija izhaja trimesečno (marec, junij, september, december). Izdaja strokovno društvo za mikroelektroniko, elektronske sestavne dele in materiale - MIDEM.
Published quarterly (march, june, september, december) by Society for Microelectronics, Electronic Components and Materials - MIDEM.

Naslov uredništva
Headquarters
Uredništvo Informacije MIDEM
MIDEM pri MIKROIKS
Stegne 11, 1521 Ljubljana, Slovenija
tel.: + 386 (0)1 51 33 768
faks: + 386 (0)1 51 33 771
e-pošta: Iztok.Sorli@guest.arnes.si
http://www.midem-drustvo.si/

Letna naročnina je 100 EUR, cena posamezne številke pa 25 EUR. Člani in sponzorji MIDEM prejemajo Informacije MIDEM brezplačno.
Annual subscription rate is EUR 100, separate issue is EUR 25. MIDEM members and Society sponsors receive Informacije MIDEM for free.

Znanstveni svet za tehnične vede je podal pozitivno mnenje o reviji kot znanstveno-strokovni reviji za mikroelektroniko, elektronske sestavne dele in materiale. Izdajo revije sofinancirajo JAKRS in sponzorji društva.
Scientific Council for Technical Sciences of Slovene Research Agency has recognized Informacije MIDEM as scientific Journal for microelectronics, electronic components and materials.
Publishing of the Journal is financed by Slovenian Book Agency and by Society sponsors.

Znanstveno-strokovne prispevke objavljene v Informacijah MIDEM zajemamo v podatkovne baze COBISS in INSPEC.

Prispevke iz revije zajema ISI® v naslednje svoje produkte: Sci Search®, Research Alert® in Materials Science Citation Index™

Scientific and professional papers published in Informacije MIDEM are assessed into COBISS and INSPEC databases.

The Journal is indexed by ISI® for Sci Search®, Research Alert® and Material Science Citation Index™

Po mnenju Ministrstva za informiranje št.23/300-92 šteje glasilo Informacije MIDEM med proizvode informativnega značaja.

Grafična priprava in tisk
Printed by
BIRO M, Ljubljana

Naklada
Circulation
1000 izvodov
1000 issues

Poštnina plačana pri pošti 1102 Ljubljana
Slovenia Taxe Percue

UDK621.3:(53+54+621+66), ISSN0352-9045 Informacije MIDEM 40(2010)1, Ljubljana

VSEBINA CONTENT

Obnovitev članstva v strokovnem društvu MIDEM in iz tega izhajajoče ugodnosti in obveznosti

Spoštovani,

V svojem več desetletij dolgem obstoju in delovanju smo si prizadevali narediti društvo privlačno in koristno vsem članom.Z delovanjem društva ste se srečali tudi vi in se odločili, da se v društvo včlanite. Življenske poti, zaposlitev in strokovno zanimanje pa se z leti spreminjajo, najrazličnejši dogodki, izzivi in odločitve so vas morda usmerili v povsem druga področja in vaš interes za delovanje ali članstvo v društvu se je z leti močno spremenil, morda izginil. Morda pa vas aktivnosti društva kljub temu še vedno zanimajo, če ne drugače, kot spomin na prijetne čase, ki smo jih skupaj preživeli. Spremenili so se tudi naslovi in način komuniciranja.

Ker je seznam članstva postal dolg, očitno pa je, da mnogi nekdanji člani nimajo več interesa za sodelovanje v društvu, se je Izvršilni odbor društva odločil, da stanje članstva uredi in **vas zato prosi, da izpolnite in nam pošljete obrazec priložen na koncu revije.**

Naj vas ponovno spomnimo na ugodnosti, ki izhajajo iz vašega članstva. Kot član strokovnega društva prejemate revijo »Informacije MIDEM«, povabljeni ste na strokovne konference, kjer lahko predstavite svoje raziskovalne in razvojne dosežke ali srečate stare znance in nove, povabljene predavatelje s področja, ki vas zanima. O svojih dosežkih in problemih lahko poročate v strokovni reviji, ki ima ugleden IMPACT faktor.S svojimi predlogi lahko usmerjate delovanje društva.

Vaša obveza je plačilo članarine 25 EUR na leto. Članarino lahko plačate na transakcijski račun društva pri A-banki : 051008010631192. Pri nakazilu ne pozabite navesti svojega imena!

Upamo, da vas delovanje društva še vedno zanima in da boste članstvo obnovili. Žal pa bomo morali dosedanje člane, ki članstva ne boste obnovili do konca leta 2009, brisati iz seznama članstva.

Prijavnice pošljite na naslov:

MIDEM pri MIKROIKS

Stegne 11

1521 Ljubljana

Ljubljana, marec 2010

Izvršilni odbor društva

SEM AND XRD CHARACTERIZATIONS OF NANOGRANULAR COPPER METAL FILMS

Kah-Yoong Chan*, Jegenathan Krishnasamy, Teck-Yong Tou

Centre for Advanced Devices and Systems, Faculty of Engineering, Multimedia University, Persiaran Multimedia, Selangor, Malaysia

Key words: Copper; Sputtering; Film thickness; Structural properties; Morphological properties

Abstract: This paper reports on the influence of film thickness on the morphological and structural properties of direct current (DC) magnetron sputter-deposited nanogranular copper (Cu) metal films. Cu metal films with thicknesses of 130 nm to 1800 nm were deposited on silicon substrates at sputtering power of 125 W in argon working gas pressure of 3.6 mTorr at room temperature. The morphological and structural properties of the nanogranular Cu metal films were investigated by scanning electron microscopy (SEM) and X-ray diffractometer (XRD). Results from our experiment show that the Cu nanograins grow with increasing film thickness, along with enhanced film crystallinity. Possible mechanisms of film thickness dependent microstructure formation of the nanogranular Cu metal films are discussed in the paper, which explain the interrelationship of grain growth with increasing Cu metal film thickness.

SEM and XRD Characterizations of Nanogranular Copper Metal Films

Kjučne besede: baker, nanašanje, debelina filma, strukturne značilnosti, morfološke značilnosti

Izvleček: Članek poroča o vplivu debeline filma na morfološke in strukturne značilnosti z DC magnetronom nanešenega nanozrnatega bakrenega filma. Bakreni kovinski filmi z debelino od 130nm do 1800nm so bili nanešeni na silicijeve podlage z močjo 125 W v atmosferi argona pri pritisku 3.6m tora pri sobni temperaturi. Morfološke in strukturne značilnosti nanozrnatih bakrenih kovinskih filmov smo pregledovali z vrstično elektronsko mikroskopijo (SEM) in difraktometrom za X-žarke (XRD). Rezultati naših poskusov kažejo, da bakrena nanozrna rastejo s povečevanjem debeline skupaj s povečano kristalnostjo filma. V članku obravnavamo tudi možne mehanizme, ki povzročajo odvisnost mikrostrukture nanozrnatih bakrenih filmov od njegove debeline.

1. Introduction

Copper (Cu) metal thin films with nano geometric and microstructural dimensions are ubiquitous of modern technology, with applications spanning the range from the catalysis to microelectronic devices. In ultralarge scale integrated (ULSI) circuits, achievement of maximum signal transmission with minimum signal propagation delay along metal interconnects in emerging chip and system architectures requires minimizing the resistance-capacitance (RC) time delay. Minimizing RC delay in thinner interconnects has forced a transition from aluminum (Al) based interconnects to Cu metallization schemes owing to the higher conductance of Cu, which not only reduces the delay time but also enables higher current densities at lower voltages, minimizing heat generation and power requirements and increasing the packaging densities per metallization level. Apart from reduction in RC time delay, Cu is more promising than Al for metallization in terms of electromigration (transport of atoms of the metal interconnects subjected to high current densities) resistance and mechanical elasticity stress /1/. Cu exhibits superior resistance to electromigration and stress-induced voiding open-circuit failure as its atoms are more strongly bounded together which account for less likely to fracture under stress comparing to Al.

Due to the noticeable advantages as interconnection candidate in terms of low electrical resistivity, good electromigration resistance and high melting temperature /2/, the studies of Cu thin films have been generally centered on the electrical and microstructural properties of the Cu films deposited with various deposition techniques. Among these, magnetron sputter deposition is a well established technology and offers an attractive alternative to diode techniques, due to lower working gas pressure employed which makes possible higher sputtering rate /3/. Also, magnetron sputtering is an attractive mass production technique due to the possibility of large area deposition /4/, which makes it an effective economic approach in microelectronics manufacturing.

In our previous research work, we studied the influence of sputtering power, deposition pressure and substrate temperature on the material properties of direct current (DC) magnetron sputter-deposited Cu metal films /5,6/. We have also examined the influence of Cu film thickness using atomic force microscopy (AFM) /7/. In this paper we present the investigation results on the effect of film thickness on the morphological and structural properties of nanogranular Cu metal films using scanning electron microscopy (SEM) and X-ray diffractometer (XRD).

2. Experimental

All Cu films were deposited with a DC magnetron sputtering system (Fig. 1) using a circular 5.08 cm diameter Cu

target of 99.995 % purity. The target to substrate distance was 9 cm. The substrates for the deposition were 6 mm x 12 mm p-type silicon (Si) and were cleaned follow standard cleaning procedure. The base pressure was lower than 2 x 10^{-6} Torr, achieved with a cryo pump coupled with a rotary pump. The sputtering deposition was carried out at a working pressure of 3.6 m Torr in high purity argon (Ar) gas (99.999%) with DC sputtering power of 125 W, which led to a deposition rate of approximately 50 nm/min. In order to study the influences of the film thickness, a series of Cu metal film samples with thicknesses controlled at around 130 nm to 1800 nm were fabricated at room temperature. The thicknesses of these Cu films were checked in situ with a quartz crystal monitor located near the substrate during the sputtering process, and was quantified with the Mahr surface profilometer after the deposition process by measuring the step height between masked and unmasked regions on the substrate. The surface morphology and microstructure of the Cu metal films were examined by means of SEM. XRD analyses in the θ-2θ mode using Cu Kα X-rays were carried out to investigate the crystallinity and orientation of the Cu metal films with different thicknesses. The deposition conditions of the Cu metal films presented in this work are summarized in Table 1.

Table 1. Deposition parameters for the Cu metal films.

Target	Cu
Substrate	p-type Si
Target-substrate distance	9 cm
Ar working gas pressure	3.6 m Torr
Sputtering power	125 W
Deposition rate	~50 nm/min
Film thickness	130 nm - 1800 nm

3. Results and discussion

The influence of the thickness on the surface morphology of the nanogranular Cu metal films was examined by the SEM, as shown in Fig. 2a-d. The SEM images show the features of structural change and grain growth for nanogranular Cu metal films with different thicknesses ranging from 130 nm to 1800 nm. The SEM image of the 130 nm thick Cu metal film deposited at room temperature (Fig. 2a) exhibits uniform surface, indicating its amorphous-like behavior /8/. Fig. 2b, 2c, and 2d show the SEM images for Cu metal films with thicknesses of 275 nm, 500 nm and 1800 nm, respectively. In these images, nanograin features develop in the Cu metal films and are enhanced with increasing film thickness. The nanograins are smaller and less definable producing smoother surface in image of Fig. 2b, and larger and evenly scattered in Fig. 2c. In Fig. 2d, the grains were observed to have agglomerated together and formed smaller number of bigger grains. The nanograins are homogeneously distributed all over the substrate surfaces. Comparing the SEM images in Fig. 2, Cu metal film with higher thickness clearly exhibits profound grain features. This can be explained by the film structural evolution with thickness, in which the grains grow with increasing film thickness /9/. The transformation from the uniform smooth amorphous-like film structure to the fine nanogranular features, followed by the growth in the nanograins for the Cu metal films with increasing film thickness as demonstrated in Fig. 2 can be attributed to the surface energy minimization during the growth process to achieve thermodynamical equilibrium. As the growth proceeds, those grains with preferred growth direction survive due to surface tends to evolve towards a situation of low surface energy. This results in evolution of large grained columnar morphology from a much larger number of fine grains which were originally nucleated on the substrate / 10/, and improved film texture according to following equations /11/:

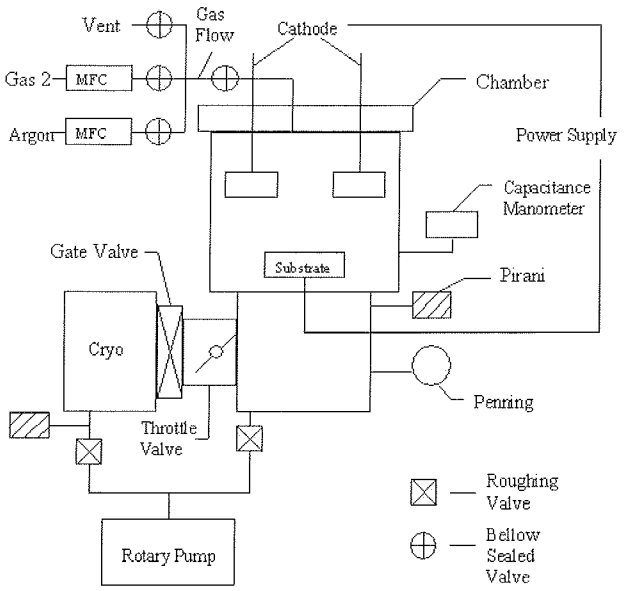

Fig. 1: Schematic diagram of the magnetron sputtering deposition system.

$$\frac{dr_i}{dt} = K[\gamma(t) - \gamma_i], \quad (1)$$

where r_i, g_i and $g(t)$ are the radius, the surface energy of i grain and mean surface energy of the surrounding grain of i. K can be described as:

$$K = (\frac{v_o L}{kT}) V_{at}^{\frac{2}{3}} \exp(\frac{-E}{kT}), \quad (2)$$

where v_o, L, k, T, $V_{at}^{2/3}$ and E are the attempt frequency, the thickness of a small layer near the surface, Boltzmann factor, the temperature, the surface change in each grain for a single jump and the mean activation energy.

The improved film texture is in agreement with the XRD patterns for these nanogranular Cu metal films with different thicknesses, as shown in Fig. 3. The intensity of a peak in X-ray diffraction pattern is a direct measure of the film crystallinity. From the intensity of the diffraction peaks (Fig. 4), Cu metal film with higher thickness exhibits enhanced

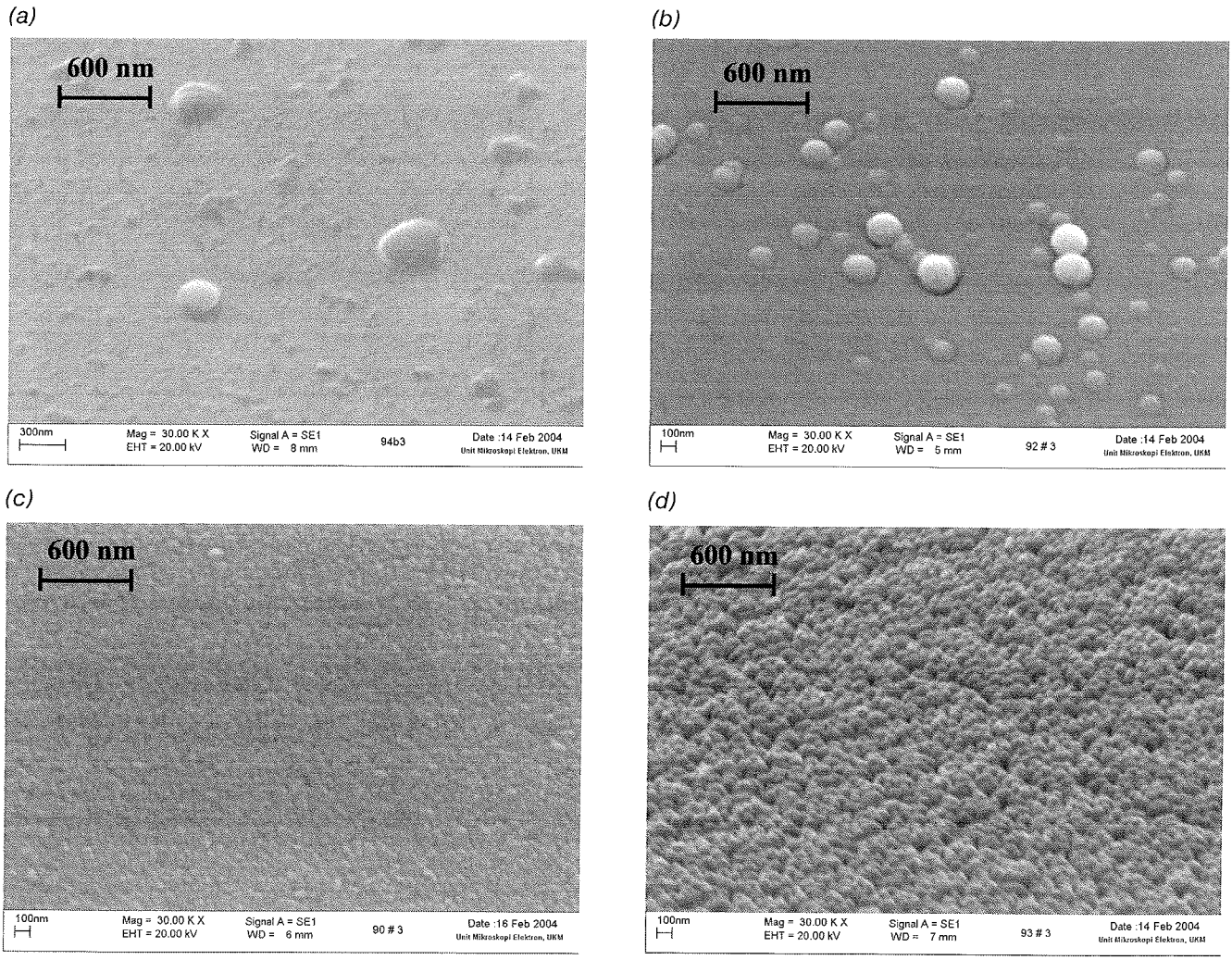

Fig. 2: Scanning electron microscopy (SEM) images of nanogranular copper (Cu) metal films with thicknesses of (a) 130 nm, (b) 275 nm, (c) 500 nm, and (d) 1800 nm.

crystalline nature than thinner metal film with preferential orientation of (111) observed at 2θ = 43 °. The film thickness has no significant influence on the preferred (200) orientation for the DC magnetron sputter-deposited Cu metal films. The increasing film thickness promotes the

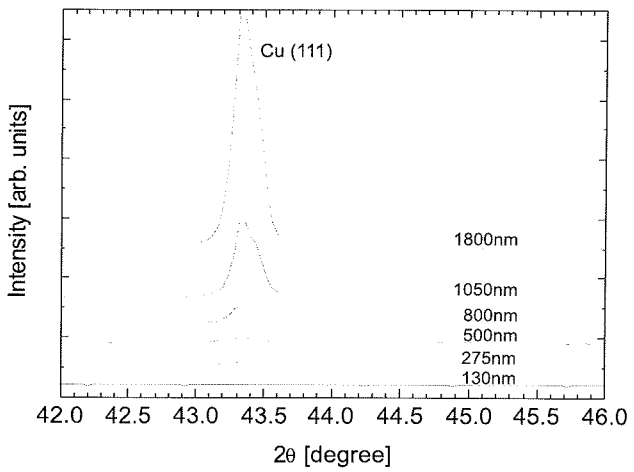

Fig. 3: X-ray diffraction (XRD) patterns of the copper (Cu) metal films with different thicknesses.

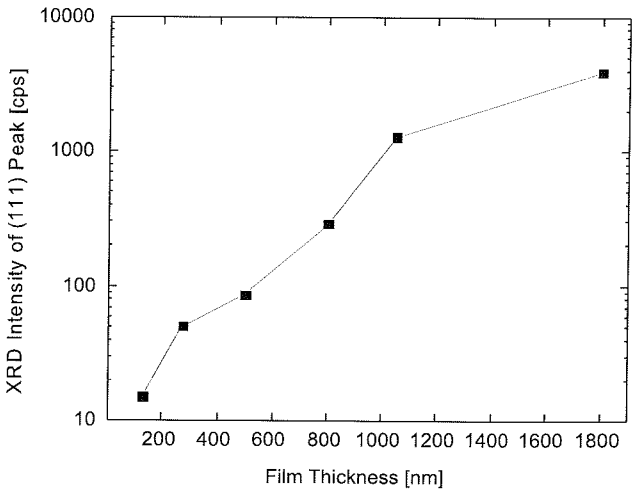

Fig. 4: Intensity of X-ray diffraction (XRD) (111) peaks of the copper (Cu) metal films as a function of the film thickness.

preferred (111) orientation but not (200) orientation because Cu has the face centered cubic (FCC) crystal structure and for this structure (111) face has the lowest surface energy /12/.

In order to obtain deeper insight into the influence of film thickness on the microstructure, we calculated the grain size of the Cu metal films with different thicknesses. Grains or crystallites are crystal units in a material that diffract in phase. When related to metallic films, the term 'grain' is also used to represent the crystal units in metallic films. In principle, the analysis of the grain size in XRD diffraction patterns is performed by measuring the broadening of a particular peak in a diffraction pattern associated with a particular planar reflection from within the crystal unit cell. The grain size (G) of the Cu metal films was deduced from the (111) diffraction peak using Scherrer's formula:

$$G = \frac{K \cdot \lambda}{FWHM \cdot \cos\theta}, \qquad (3)$$

where K is the shape factor of the average grain (0.9), λ is the X-ray wavelength (0.154056 nm for Cu $K\alpha_1$), FWHM is the full width at half maximum of the diffraction peak, θ is the diffraction peak angle. From the Eqn. (3), the grain size is inversely related to the FWHM of the diffraction peak. The more narrow the diffraction peak, the larger the grain size is. This is due to the periodicity of the individual grain domains which are in phase, reinforcing the X-ray beam, and results in a narrow diffraction peak. Most thin films have some degree of preferred orientation. For Cu, it is usually (111) crystallographic direction that has the greatest degree of preferred orientation. Therefore, the measured grain size of the (111) diffraction peak represents the grain size in the columnar direction, normal to the surface of the substrate. Fig. 5 demonstrates the dependence of the Cu metal grain size and FWHM on the film thickness. In general, the grain size increases with increasing Cu metal film thickness and the FWHM acts in opposite way. For the Cu metal films with thicknesses of 130 nm, 275 nm, 500 nm, 800 nm, 1050 nm, and 1800 nm, the corresponding nanograin sizes are 27 nm, 36 nm, 39 nm, 44 nm, 48 nm, and 51 nm, respectively, while the corresponding FWHM are 0.40 °, 0.30 °, 0.28 °, 0.25 °, 0.22 °, and 0.21 °, respectively. The grain size of the Cu metal films deduced using Scherrer's formula is consistent with the intensity of the corresponding diffraction peak of the films.

4. Conclusions

We have qualitatively evaluated the thickness dependence of the morphological and structural properties of DC magnetron sputter-deposited nanogranular Cu metal films. The surface morphological study with SEM shows the enhanced microstructure, while the XRD patterns reveal the improved crystalline quality for the thicker Cu metal films. The grain size of the Cu metal films was found to increase with increasing film thickness, which is due to the surface energy minimization when the film gets thicker.

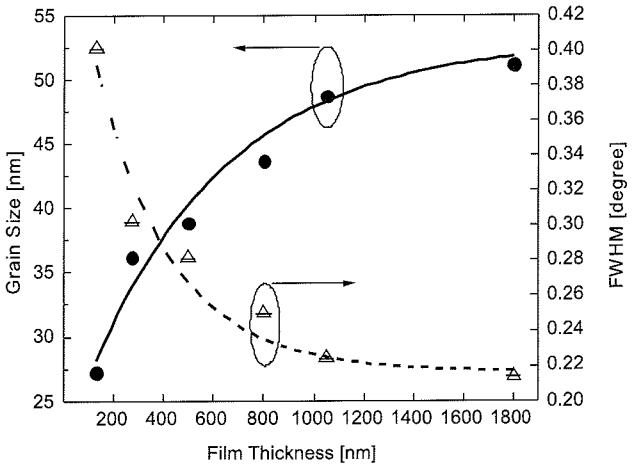

Fig. 5: Grain size and full width at half maximum (FWHM) of X-ray diffraction (XRD) (111) peaks of the copper (Cu) metal films as a function of the film thickness.

Acknowledgement

This research work was financially supported by Multimedia University (MMU) through its R&D Internal Fundings.

References

/1/ J. P. Chu, C. H. Lin, V. S. John, Barrier-free Cu metallization with a novel copper seed layer containing various insoluble substances, Vacuum 83 (2009) 668-671.

/2/ H. Qiu, F. Wang, P. Wu, L. Pan, Y. Tian, Structural and electrical properties of Cu films deposited on glass by DC magnetron sputtering, Vacuum 66 (2002) 447-452.

/3/ Y. Mikami, K. Yamada, A. Ohnari, T. Degawa, T. Migita, T. Tanaka, K. Kawabata, H. Kajioka, Effect of DC bias voltage on the deposition rate for Ni thin films by RF-DC coupled unbalanced-magnetron sputtering, Surface and Coatings Technology 133-134 (2000) 295-300.

/4/ L. Kim, J. Kim, D. Jung, C.Y. Park, C.W. Yang, Y. Roh, Effects of deposition parameters on the crystallinity of CeO_2 thin films deposited on Si(100) substrates by r.f.-magnetron sputtering, Thin Solid Films 360 (2000) 154-158.

/5/ K.-Y. Chan, B.-S. Teo, Sputtering power and deposition pressure effects on the electrical and structural properties of copper thin films, Journal of Materials Science 40(22) (2005) 5971-5981.

/6/ K.-Y. Chan, T.-Y. Tou, B.-S. Teo, Effects of substrate temperature on electrical and structural properties of copper thin films, Microelectronics Journal 37(9) (2006) 930-937.

/7/ K.-Y. Chan, T.-Y. Tou, B.-S. Teo, Thickness dependence of the structural and electrical properties of copper films deposited by dc magnetron sputtering technique, Microelectronics Journal 37(7) (2006) 608-612.

/8/ R. Sivakumar, M. Jayachandran, C. Sanjeeviraja, Studies on the effect of substrate temperature on (VI-VI) textured tungsten oxide (WO_3) thin films on glass, SnO_2:F substrates by PVD:EBE technique for electrochromic devices, Materials Chemistry and Physics 87 (2004) 439-445.

/9/ D.B. Knorr, D.P. Tracy, A review of microstructure in vapor deposited copper thin films, Materials Chemistry and Physics 41 (1995) 206-216.

/10/ A. Wagendristel, Y. Wang, An Introduction to Physics and Technology of Thin Films, World Scientific, Singapore 1994. p. 135.

/11/ G. Knuyt, C. Quaeyhaegens, J. D'Haen, L.M. Stals, A quantitative model for the evolution from random orientation to a unique texture in PVD thin film growth, Thin Solid Films 258 (1995) 159-169.

/12/ N. Joshi, A.K. Debnath, D.K. Aswal, K.P. Muthe, M. Senthil Kumar, S.K. Gupta, J.V. Yakhmi, Morphology and resistivity of Al thin films grown on Si (111) by molecular beam epitaxy, Vacuum 79 (2005) 178-185.

Kah-Yoong Chan,
Jegenathan Krishnasamy, Teck-Yong Tou,
Tel.: +60-3-8312 5438; fax: +60-3-8318 3029.

Centre for Advanced Devices and Systems, Faculty of Engineering, Multimedia University, Persiaran Multimedia, 63100 Cyberjaya, Selangor, Malaysia
E-mail address: kychan@mmu.edu.my (K.Y. Chan).

Prispelo (Arrived): 24.07.2009 *Sprejeto (Accepted): 09.03.2010*

THE APPLICATION OF RUTILE NANO - CRYSTALLINE TITANIUM DIOXIDE AS UV ABSORBER

Jerneja Godnjavec[1], Bogdan Znoj[1], Peter Venturini[1], Andrej Žnidaršič[2]

[1]Helios Domžale, d.d., Domžale, Slovenia
[2]Nanotesla Institut, Ljubljana, Slovenia

Key words: titanium dioxide, rutile, co-precipitation method, UV absorber, surfactant

Abstract: Nano - crystalline titanium dioxide (TiO_2) in rutile crystal form, generally used to indicate particles less than 100 nm in diameter, is mainly applied as pigment, adsorbent and UV absorber. The incorporation of a nano-sized titanium dioxide powder into a liquid media is made by dispersion process, that the final product consists of fine particles distribution throught the medium. So it is regarded as necessary for us to investigate in detail the factors which may have important effect upon the homogenious distribution of TiO_2 nanoparticles in clearcoat as liquid media.

In this work, titanium dioxide nano-powders were prepared by the co-precipitation method. Using various techniques, including transmission electron microscopy (TEM) and X-ray diffraction (XRD), obtained powders were studied in order to find the possible elements of affecting the microstructures and grain size. The aim of this study is to determine the photostabilisation efficiency of TiO_2 in a clear coat as UV absorber considering the preparation of stable dispersions by using different surfactants and percentage of TiO_2.

Uporaba titanovega dioksida v rutilni kristalinični obliki kot UV absorber

Kjučne besede: titanov dioksid, rutil, koprecipitacijska metoda, UV absorber, surfaktant

Izvleček: Nanodelci titanovega dioksida (TiO_2) v rutilni kristalinični obliki so delci premera velikosti pod 100 nm, ki se večinoma uporabljajo kot pigment, adsorbent in UV absorber. Ko nanodelce TiO_2 vgradimo v tekoč medij z dispergiranjem, mora imeti disperzija ozko porazdelitev velikosti delcev. Analizirali smo dejavnike, ki vplivajo na homogenost porazdelitve velikosti nanodelcev TiO_2 v transprentnem premazu.

Nanodelce TiO_2 smo pripravili z koprecipitacijsko metodo. Da bi ugotovili, kaj vpliva na mikrostrukturo in velikost nanodelcev TiO_2, smo uporabili različne analizne metode, meddrugim tudi presevno elektronsko mikroskopijo (TEM) in rentgensko praškovno difrakcijo (XRD). Cilj študija je bil določiti učinkovitost transparentenga premaza z nanodelci TiO_2 kot UV absorber v odvisnosti od priprave stabilne disperzije z uporabo različnih surfaktantov in deleža nanodelcev TiO_2.

1. Introduction

The ultraviolet (UV) protection of organic and biological materials against photodestruction is of high practical interest. The protection can be realized by use of UV absorbers. UV absorbers are organic or inorganic compounds which absorb in the best case all UV light and are transparent for all visible light. UV absorbers are most frequently used in cosmetics to prevent sunburns and skin cancer /1-3/. Beside the protection of human skin, UV absorbers are often to protect materials properties of polymers or textiles /4, 5/.

Lignin in wood for instance highly absorbs ultraviolet light, which leads to radical induced depolymerisation of both lignin and cellulose or in other words to photodegradation of the wood substrate. Wood colour change is the first sign of its chemical modification when exposed to UV light /6 - 8/. One possibility of wood protection is the usage of pigmented coatings, where the pigments reflect the UV - radiation. However, in this case, the natural colour of the wood is changed. Consequently, for the last decade inorganic UV absorbers have received a great deal of attention in transparent wood coatings because of their function as UV blockers. One of the reasons for the limited commercial use of certain nanoadditives is that they greatly affect the transparency of clearcoats because of its high tendency to agglomeration in dispersions. This is clearly undesirable in a treatment design to improve the longevity of clear varnishes, since the appeal of such finishes lies in their ability to maintain the natural appearance of wood /6/.

UV absorbers, based on fine nanoparticled titanium dioxide and zinc oxide (ZnO) have proved to be efficient /9/. Both TiO_2 and ZnO are commonly used as white pigments. TiO_2 in the rutile form is the most common white pigment due to its extremely high refractive index (n = 2, 8). Ultrafine TiO_2 and ZnO nanoparticles lose their capability to scatter visible light, but retain the ability to absorb UV light. The bandgap of ZnO (3,2 eV) is similar to that of TiO2 in the anatase modification and a little larger than the rutile type. When using TiO_2 for UV protection the rutile type is more suitable due to its lower photocatalytic activity, which could destroy the organic surrounding matrix. The small particle of nano - crystalline titanium dioxide UV absorber can be synthesized using several methods. e.g. the sol - gel organic method /10, 11/, co-precipitation and microemulsion methods /12/ and hydrothermal method /13/. In this paper, titanium dioxide nano-powders were prepared by the liquid phase co-precipitation routes, typically involved

titanium dioxide particle growth steps, followed by aggregation, from high temperature treatment and control finished product particle size at the optimum required for performance. As already mentioned the biggest challenge of stable nanoparticle dispersion development is to prevent nanoparticles tendency to form agglomerates resulting in poor dispersion within the carrier matrix with low UV absorption efficiency. One of the ways to overcome this drawback is the addition of compatible surfactants.

The aim of our study was to determine the influence of the concentration of TiO_2 nanoparticles and different surfactants on dispersion homogeneity resulting as UV absorption efficiency of clearcoating.

2. Methods

Synthesis of titanium dioxide Nano Crystalline Particles in rutile crystal structure

Synthesis of titanium (IV) oxide nanoparticles with rutile crystal structure takes place as described below /15, 16/. Regarding the stoichiometry of reaction (eq. /1/) an appropriate amount of 12.5 % titanyl sulfate ($TiOSO_4$) acid solution with density 1.4 g/cm^3 was hydrolyzed in a stirred tank and precipitated with an excess amount of 2.4-M aqueous solution of dialkilamide, which served as a precipitating reagent.

$$TiOSO_4 + 2H_2O \xrightarrow{\text{hydrolysis}} TiO(OH)_2 + \\ + H^+ + SO_4^{2-} \xrightarrow{\text{precipitation}} Ti(OH)_2(\downarrow) \quad (1)$$

Precipitation was conducted for 6 hours at a constant temperature of 100 ± 2 °C. Pigmented nanoparticles of hydrolyzed titanium (IV) oxide (TiO2·xH2O·ySO3) obtained after the precipitation were sedimented with the addition of 0.33 % aqueous solution of anionic polyacrylic flocculent, separated from mother liquor in the next step and finally dried at temperature 120±2 °C. Dried nanoparticels of hydrolyzed titanium (IV) oxide were annealed for 2 hours at 900 °C in air in order to obtain pure rutile crystal structure. After annealing, rutile nanoparticles were deagglomerated in a high-energy horizontal zirconium attrition mill for 8 hours. Obtained nanoparticles were analyzed with X-ray powder diffraction (XRD), transmission electron microscopy (TEM) and specific surface area (BET) measurements.

Deagglomerated rutile nanoparticles were surface treated with organic surface active agents (Byk 333, ethilen glicol) in high-energy horizontal attrition mill. The pH value was sustained between 8 and 9 using 25 % of ammonia aqueous solution in order to prepare stable and transparent pigmented aqueous dispersion of titanium (IV) oxide with rutile crystal form. The pH of a coating, in which we mixed in water dispersion of nanoparticles, was approximatly 8.

Preparation of clearcoat with integrated rutile crystalline particles of TiO_2

We prepared clearcoat in the laboratory by mixing pure acrylic resin with styrene acrylic copolymer resin for 20 minutes. Commercial polysiloxane defoamer from Byk Additives&Instruments and previously prepared premix of chemical additives were added for optimal coating application properties like leveling and wetting. Than we add different glycols as coalescents, water, wax emulsion and flatting aqueous wax dispersion, both from Byk Additives&Instruments, during the mixing process. At the end nonionic rheology modifier from Rohm and Haas was mixed in for 20 minutes to achieve appropriate viscosity (100-200 mPas).

The dispersions of TiO_2 nanoparticles in liquid media were prepared by milling 30 wt.% of TiO_2 nanoparticles in rutile crystal form, water and different surfactants (Table 1). Water based dispersions of TiO2 nanoparticles were then added to clearcoat and prepared for the testing.

Table 1: Samples and their composition.

Sample	Composition
1	clearcoating
2	clearcoating with TiO2 nanoparticles ethilen glicol octanol 2
3	clearcoating with TiO2 nanoparticles Byk 333 Byk 024

Transparency and photostabilization performance assessments

Wood blocks measuring 15x7 cm^2 (longitudinal x tangential) x 0,5 cm width were cut from air dried boards from the specie pine. Two layers of clear coat of thickness of 200 µm were applied on pine blocks. Coated wood plates were used to assess weathering exposure degradation (QUV accelerated weathering tester, Q - PANEL LAB PRODUCTS, standard SIST EN ISO 11507:2002). Simulation of exterior use was done by six weeks weathering by an optimised cycle defined: 4h at (60±3) °C and 4h water shower at (50±3) °C. Only light of the solar type was activated on the QUV with sources type UVA-340 nm.

Color evaluation was done in the CIE L*, a*, b* system. The initial value of the sample colour before exposure and after coating application was compared. Color difference (ΔE*) was calculated with the following formula (eq. 1):

$$\Delta E^* = \sqrt{(\Delta a^*)^2 + (\Delta b^*)^2 + (\Delta L^*)^2} \quad (1)$$

where L* is the lightness from the black (0) to the blank (100), a* (from green colour to red) and b* (from blue to yellow) are the chromatic coordinates. The colour measurement of coated wood specimens was conducted using spectrophotometer (Datacolor SF600).

3. Results and discussion

Nano TiO_2 powders were calcined at different temperatures and taken XRD (Fig. 1). It can be obviously seen that partial crystallization appears just after drying and the phase structure of the powder calcined at temperature bellow 600 °C is mainly of anatase type. The phase transformation from anatase to rutile occurred at about 600 °C and completed at about 900 °C.

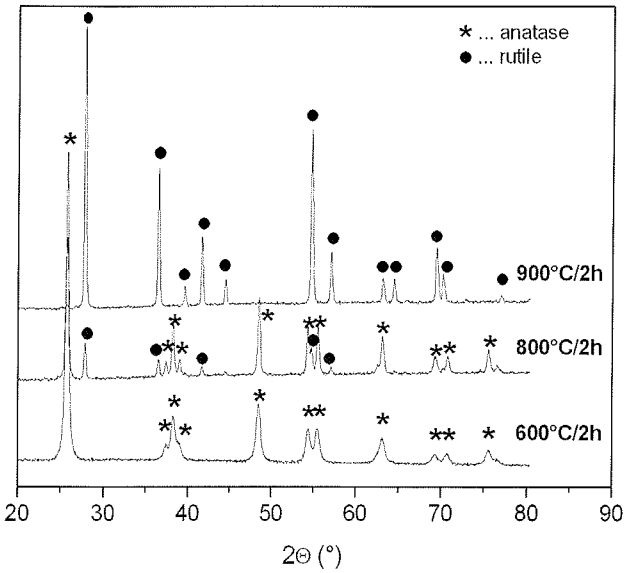

Fig. 1: The XRD pattern of nano-crystalline TiO_2 at different calcination temperatures.

From the TEM images of the milled TiO2 powders presented in Fig. 2, finally dispersed particles with a relatively wide distribution of sizes, ranging from 20-70 nm for rutile and from 10-30 nm for anatase, together with almost the rounded shapes thereof, typical for milling treatments in general, can be observed.

Changes in colour of painted pine wood samples (wood discolouration) during UV exposure have been widely used to asses wood degradation /11, 17 - 20/. By measuring the colour change of the coated wood with different UV absorbers during artificial weathering is there possible to obtain information on their efficiency. We prepared three different samples of clearcoating with and without addition of TiO_2 nanoparticles as defined in Table 1. The concentration of TiO_2 nanoparticles in clearcoat was also varied. For weathering simulation colour changes ΔE^* during the UV irradiation of samples of UV protection clear coat on wood substrate are displayed in Fig 3. The data revealed a number of interesting features. Sample 3 with polyether modified dimethylpolysiloxane copolymer surfactant proved to be the most efficient in inhibiting colour change. We also noticed that different concentration of TiO_2 nanoparticles does not have an significant influence on photostabillity of the clear coat.

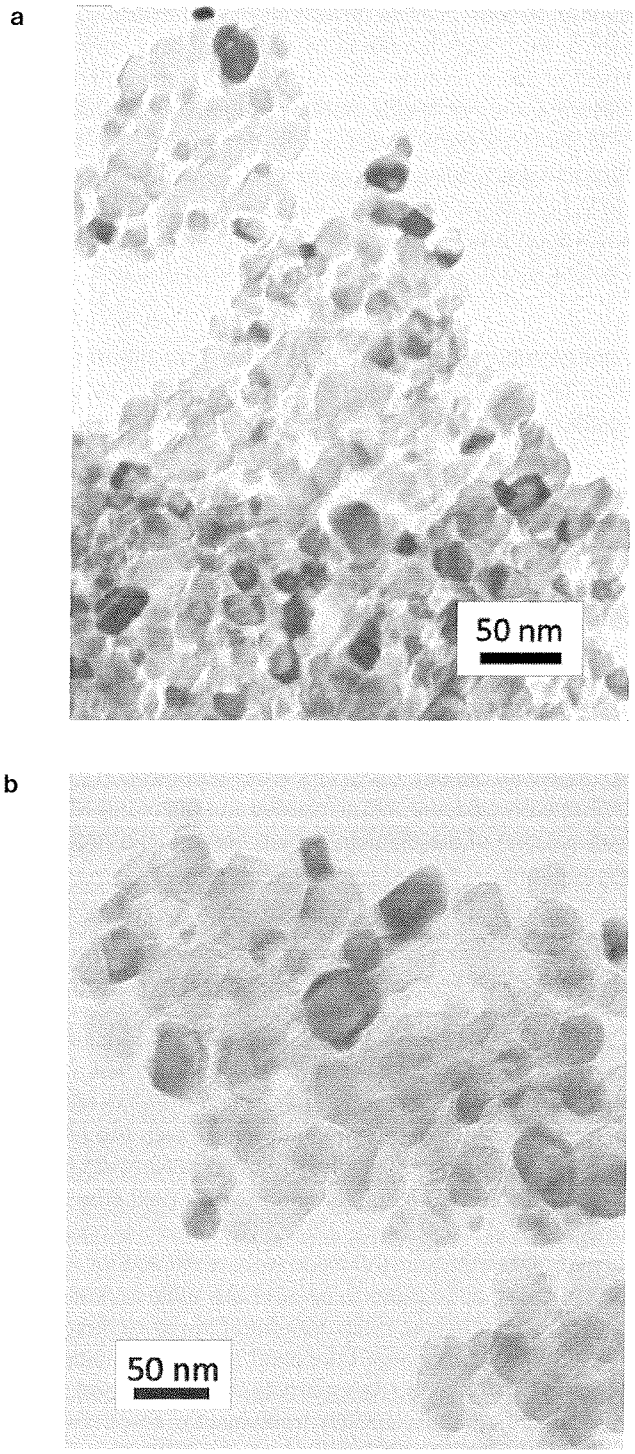

Fig. 2: The typical TEM micrographs of the nano – TiO_2 powders calcined at a.) 600 °C (anatase crystal form) and b.) 900 °C (rutile crystal form).

4. Conclusion

A successful pathway for the preparation of titanium (IV) oxide in rutile crystal form and some of the basic properties of a material, such as UV-absorbance and photostabilization, have been presented. Hydrolysis of titanyl sulfate ($TiOSO_4$) followed by a precipitation with dialkilamide, and the subsequent calcinations in air at 900 °C for 2h, com-

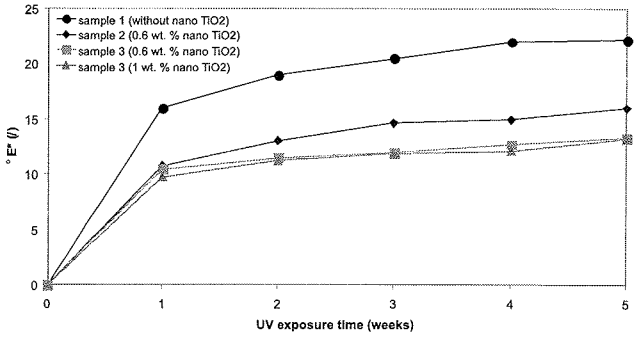

Fig. 3: Colour change vs. UV irradiation (weeks) in QUV apparatus for different samples of UV protection clearcoating.

prised the basic synthesis steps toward the final material. The pure rutile particles produced at 900 °C were in the range of 40-100 nm, whereas the final anatase nanoparticles were almost uniformly ~ 20 nm in size.

By measuring the colour change of the clear coated wood with different UV absorbers during artificial weathering we revealed that the clearcoating with 0,6 and 1 wt. % of rutile TiO_2 nanoparticles stabilized by polyether modified dimethylpolysiloxane copolymer surfactant surface additive (Byk 333) has the best photostabilization performance of UV protection clear coat. We also noticed that UV efficiency did not improve when the concentration of TiO_2 nanoparticles was higher. We assume that higher concentration of TiO_2 nanoparticles leads to agglomeration. Nevertheless we improve the photostability of the clear coat by the addition of stable dispersion of TiO_2 nanoparticles in rutile crystal form for more than 40 % according to colour change of protected wood panels.

References

/1./ N. Lapidost, O. Gans, F. Biagini, L. Sosonkin, C. Rottman, J. Sol-Gel Sci. Technol., 26, 67, (2003)

/2./ B. Herzog, D. huglin, E. Borsos, A. Stehlin, H. Luther, Chimia 58, 554, (2004).

/3./ D. Avnir, L.D. Cohen, U.S. Patent, No 6159453, 15. 7. 1999.

/4./ F.A. Bottina, G. di Pasquale, A. Polliciano, A. Recca, J. Appl. Polym. Sci., 69, 1251, (1998).

/5./ E.G. Tsatsaroni, I.C. Eleftheriadis, Dyes Pigm., 61, 141, (2004).

/6./ M. Kiguchi, P. D. Evans, J. Ekstedt, R. S. Williams, Y. Kataoka, Surf. Coat. Int. Part B Coat. Trans. 84 (B4), 243-336, (2004).

/7./ H.E. Ashton, Proceedings of the Joint Symposium of the Montreal and Toronto Societies for coatings Technology, 52, 663, (1980).

/8./ P. Hayoz, W. Peter, D. Rogez, Prog. Org. Coat., 48(2-4), 297-309, (2003).

/9./ Nanocoatings 2007, nanoposts.com.

/10./ A. Linsebigler, G. Lu, J. Yates, Chem. Rev., 95, 735, (1995).

/11./ T. Thurston, J. Wilcoxon, J. Phys. Chem B, 103, 11, (1999).

/12./ A. Košak, D. Makovec, A. Žnidaršič, M. Drofenik., *J. Eur. Ceram. Soc.*., 24, 959-962, (2004).

/13./ D. Makovec, M. Drofenik, A. Žnidaršič, *J. Eur. Ceram. Soc.*, 21, 1945-1949. (2001).

/14./ Mari de Meijer, Prog. Org. Coat., 43, 217-225, (2001).

/15./ Žnidaršič, A., Košak, A., Rajnar, N., Patent 22625, (2007).

/16./ A. Košak, A. Žnidaršič, N. Rajnar, Patent application - P 200800131, (2008).

/17./ J. Hocken, K. Pipplies, K. Schulte, Proceedings of the Fifth Nurnberg Congress, Nurnberg, Germany, April 2-14, (1999).

/18./ L. Tolvaj, E. Barta, G. Papp, Cost E 18, Seminar 2-wood photodegradation and stabilization, Paris France, June 18-19, (2001).

/19./ P. Hayoz, W. Peter, D. Rogez, Prog. Org. Coat., 48, 297-309, (2003).

/20./ J. Custodio, I. eusebio, L. Nunes, , COST-E18, Coatings on Wood Symposium on Measuremnt Methods, Coating Consultancy Copenhagen, February 16-17, (2004).

/21./ G. Buxbaum, Industrial Inorganic Pigments, VCH Verlagsgesellschaft mbH, D-69451 Weinheim, (1993).

mag. Jerneja Godnjavec
Helios Domžale, d.d.,
Količevo 2, p.p. 127, 1230 Domžale, Slovenia
e-mail: Jerneja.godnjavec@helios.si
Telefon: (01) 722 7376

dr. Bogdan Znoj
Helios Domžale, d.d.,
Količevo 2, p.p. 127, 1230 Domžale, Slovenia
e-mail: bogdan.znoj@helios.si
Telefon: (01) 722 4055

doc. dr. Peter Venturini
Helios Domžale, d.d.,
Količevo 2, p.p. 127, 1230 Domžale, Slovenia
e-mail: peter.venturini@helios.si
Telefon: (01) 722 4373

doc. dr. Andrej Žnidaršič
Nanotesla Institut,
Stegne 29, 1521 Ljubljana, Slovenia
e-mail: andrej.znidarsic@nanotesla.si
Telefon: +386 1 5833 122

Prispelo (Arrived): 21.09.2009 *Sprejeto (Accepted): 09.03.2010*

TOKOVNO VODENJE TRIFAZNEGA MOTORJA S FPGA VEZJEM

Horvat Robert, Jezernik Karel

Univerza v Mariboru, FERI, Maribor, Slovenija

Kjučne besede: dogodkovno vodenje, histereznik, napetostni vektor, napetostni sektor, FPGA vezje

Izvleček: V delu je opisana primerjava histereznega in dogodkovnega tokovnega vodenja trifaznega motorja. Primerjali smo dogodkovno vodenje s tremi in dvema aktivnima napetostnima vektorjema. Prikazane so prednosti in slabosti histereznih regulatorjev pred linearnimi. Ocenjevanje uporabnosti različnih metod je prikazano glede na valovitost izhodnega toka in število preklopov tranzistorskega mostu, kar neposredno vpliva na stikalne izgube pretvornika. Tokovna regulacija je preizkušena na eksperimentalnem modelu s FPGA vezjem, ki ga programiramo s pomočjo VHDL kode z orodjem ISE. FPGA vezje je polje programabilnih logičnih vrat. Logična vrata omogočajo dogodkovno vodenje, ki ni vezano na čas urinega cikla. V delu so predstavljene še vse ostale prednosti FPGA vezja v primerjavi z DSP sistemom.

Current direction of three-phase motor with FPGA circuit

Key words: event direction, hysteresis, voltage vector, voltage sector, FPGA circuit

Abstract: In this paper difference of conventional and event driven AC current control of AC motor is described. We compare of the use three and two voltage vectors in discrete event current control. Assessment of usability of different procedures is showed considering waviness of output current and number of overlaps. Current regulation is tested on experimental model with FPGA (field-programmable gate arrays) circuit. FPGA is allowing event drive that is independently from clock. The paper presents new embedded switching control properties of FPGA-based techniques. Simple implementation makes concept of switching control very attractive in power electronic systems, like control of inverter. Results are showing that discrete event control with three active voltage vectors is proper that conventional hysteresis control because of lesser number of overlaps and less waviness of output current. Discrete event control with just two active voltage vectors allowing lesser number of overlaps, considering of method with three active voltage vectors, but increase waviness of output current.

1. Uvod

Za implementacijo zelo hitrih sistemov, kjer frekvenca delovanja digitalnega signalnega procesorja (DSP) ne zadostuje več, vedno pogosteje uporabljamo polja programabilnih logičnih vrat (Field-programmable gate array - FPGA). Prednost FPGA vezja glede na DSP sistem je v paralelnem načinu izvajanja, ki omogoča, da se vsi procesi izvajajo istočasno, torej s številom procesov ne vplivamo na frekvenco delovanja. Pri DSP sistemih (zaporedni način izvajanja) se s kompleksnostjo programa (večje število vrstic) zmanjšuje frekvenca delovanja. Na ta način lahko s FPGA vezjem dosegamo 100 krat višje frekvence delovanja. FPGA je elektronsko vezje sestavljeno iz logičnih vrat, kar je zelo primerno za dogodkovno vodenje. O dogodkovnem vodenju govorimo takrat, ko za spremembo izhodnega stanja ne potrebujemo čas urinega cikla, ampak se to zgodi takoj, ko imamo pogoj za drugo stanje. Primer takšnega vodenja so logična vrata. Pri logičnih vratih (Slika 1) se izhodno stanje OUT spremeni glede na vrednosti IN1 in IN2, ne da bi za to potrebovali čas (urin cikel).

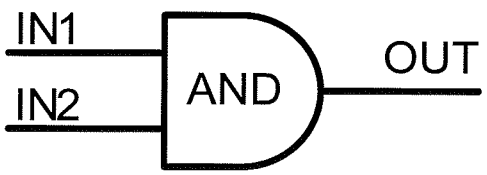

Slika 1. Logična vrata AND

Slabost FPGA vezja pa predstavlja izvajanje računskih operacij. Za razliko od DSP sistema, kjer računamo s CPU enoto, se pri FPGA vezju računa s celimi števili (fix point). Oba sistema je možno reprogramirati. Poleg vseh zgoraj opisanih lastnosti, pa FPGA vezje predstavlja tudi ekonomsko zanimivo orodje, ki je finančno zelo ugodno, programska oprema pa je brezplačno na voljo na spletu.

V nadaljevanju je opisana tokovna regulacija trifaznega motorja s pomočjo histereznega regulatorja. Opisane so lastnosti histereznega regulatorja, kot tudi princip dogodkovnega tokovnega vodenja. Simulacijsko dobljeni rezultati obravnavajo primerjavo med konvencionalnem histereznem vodenjem in dogodkovnim tokovnim vodenjem. Z dvema ali tremi aktivnimi vektorji. Rezultati prikazujejo vpliv različnih možnosti preklapljanja na valovitost toka in hitrost preklapljanja tranzistorjev.

2. Eksperimentalni model

Za izvedbo eksperimenta uporabimo razvojno ploščo Nexys Digilent, ki je namenjena izvajanju algoritmov s pomočjo VHDL kode, ki jo programiramo s pomočjo orodja ISE. Testna plošča vsebuje 100 prosto dostopnih vhodno izhodnih lokacij, 8 stikal, 8 LED, 4 tipke in 4 sedem segmentni LED prikazovalnik,.. (Slika 2). Programiranje plošče Nexys izvajamo enostavno in hitro s pomočjo osebnega računalnika, ki ga s ploščo povežemo preko USB komunikacije.

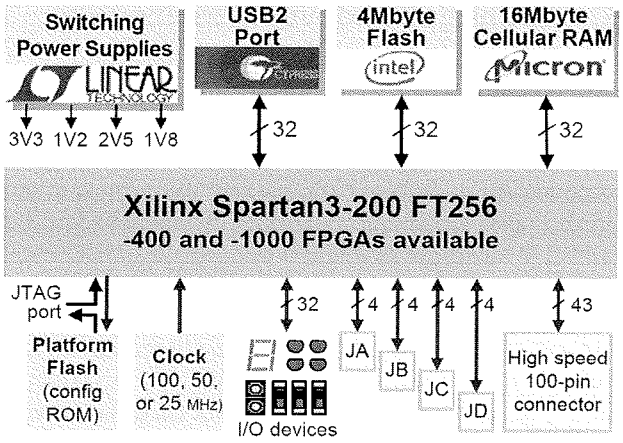

Slika 2. Blokovni diagram Nexys Digilent

Uporabljamo lahko izvedbo vezja z 400.000 ali 1.000.000 logičnimi vrati.

3. Primerjava linearnih in histereznih regulatorjev

Slabost linearnih regulatorjev je predvsem v tem, da so njihove zmožnosti odvisne od ujemanja nastavljenih parametrov regulatorja z dejanskimi parametri motorja. Z uporabo linearnih regulatorjev se težko izognemo sledilnemu pogrešku, še posebej pri motorjih z nizko električno časovno konstanto. Histerezni regulatorji spadajo med nelinearne regulatorje in se največkrat uporabljajo predvsem zaradi svojih dobrih lastnosti. Prednosti histereznih regulatorjev je v enostavni izvedbi, visoki robustnosti, zelo dobri dinamiki (omejen je z hitrostjo stikalnega pretvornika in časovno konstanto bremena), odpravlja pa tudi sledilni pogrešek. Seveda pa ima histerezni regulator tudi slabosti, kot so spremenljiva stikalna frekvenca in možnost pojava limitnih ciklov. Pojav limitnih ciklov povzroča zelo visoke stikalne frekvence, kar povzroča večje izgube in v skrajnem primeru tudi uničenje stikalnega pretvornika.

4. Stikalni pretvornik

Za izvedbo tokovnega vodenja izmeničnih motorjev potrebujemo električni izvor, ki mu lahko poleg amplitude spreminjamo tudi frekvenco in fazo. Takšen izvor dobimo s pretvorniki, ki pretvarjajo enosmerni v izmenični izvor. Izvor enosmerne napetosti lahko dobimo direktno iz akumulatorske baterije ali z usmerjanjem omrežne napetosti. V primeru, da motor deluje v generatorskem režimu je potrebno biti pozoren na vračanje energije v enosmerni vir. Za manjše moči se lahko zanesemo kar na zaviralni upor, sicer pa moramo uporabiti tranzistorski usmernik, ki energijo vrača nazaj v omrežje. Napetostni stikalni pretvornik za napajanje trifaznih motorjev je sestavljen iz enosmerne zbiralke Udc (enosmerni izvor s konstantno napetostjo DC) in šest polprevodniških stikalnih elementov (Slika 3). V vsaki od treh vej pretvornika je lahko v prevodnem stanju le en tranzistor, saj bi sicer prišlo do kratkega stika.

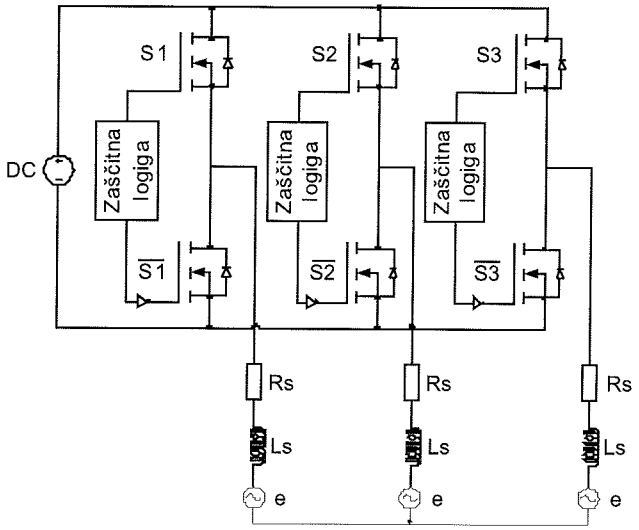

Slika 3. Trifazni izmenični most za vodenje izmeničnega motorja

Za preprečevanje kratkega stika uporabljamo zaščitno logiko, ki implementira mrtve čase. Mrtvi čas predstavlja časovni interval med izklopom enega in vklopom drugega tranzistorja v eni veji. Tako lahko s šestimi stikalnimi elementi realiziramo osem različnih stikalnih stanj (Tabela 1).

Tabela 1: Statorska napetost pri različnih stikalnih stanjih

S1	*S2*	*S3*	*Us1*	*Us2*	*Us3*
0	0	0	0	0	0
1	1	1	0	0	0
1	0	0	$\frac{2}{3}Udc$	$-\frac{1}{3}Udc$	$-\frac{1}{3}Udc$
1	1	0	$\frac{1}{3}Udc$	$\frac{1}{3}Udc$	$-\frac{2}{3}Udc$
0	1	0	$-\frac{1}{3}Udc$	$\frac{2}{3}Udc$	$-\frac{1}{3}Udc$
0	1	1	$-\frac{2}{3}Udc$	$\frac{1}{3}Udc$	$\frac{1}{3}Udc$
0	0	1	$-\frac{1}{3}Udc$	$-\frac{1}{3}Udc$	$\frac{2}{3}Udc$
1	0	1	$\frac{1}{3}Udc$	$-\frac{2}{3}Udc$	$\frac{1}{3}Udc$

Glede na dovoljena stikalna stanja generiramo fazne napetosti (Tabela 1). Stanje 0 pomeni, da stikalni element ni v prevodnem stanju, stanje 1 pa pomeni, da je v prevodnem stanju. Fazne napetosti določimo tako, da predpostavimo, da imamo breme (motor) popolnoma simetrično v zvezdo vezano simetrično breme z omsko in induktivno komponento. Z vektorsko vsoto faznih napetosti *us*1, *us*2, *us*3 oziroma trifazno-dvofazno transformacijo (Clarkova transformacija) dobimo v dvofaznem (*a,b*) sistemu osem napetostih vektorjev.

$$\begin{bmatrix} u_{sa} \\ u_{sb} \end{bmatrix} = \begin{bmatrix} 1 & -\frac{1}{2} & -\frac{1}{2} \\ 0 & \frac{\sqrt{3}}{2} & \frac{\sqrt{3}}{2} \end{bmatrix} \begin{bmatrix} u_{s1} \\ u_{s2} \\ u_{s3} \end{bmatrix} \quad (1)$$

Od osmih napetostnih vektorjev ima šest vektorjev (V1 – V6) dolžino napetosti enosmerne zbiralke Udc, medtem ko sta vektorja V0 in V7 ničelna vektorja z dolžino 0 (Slika 4).

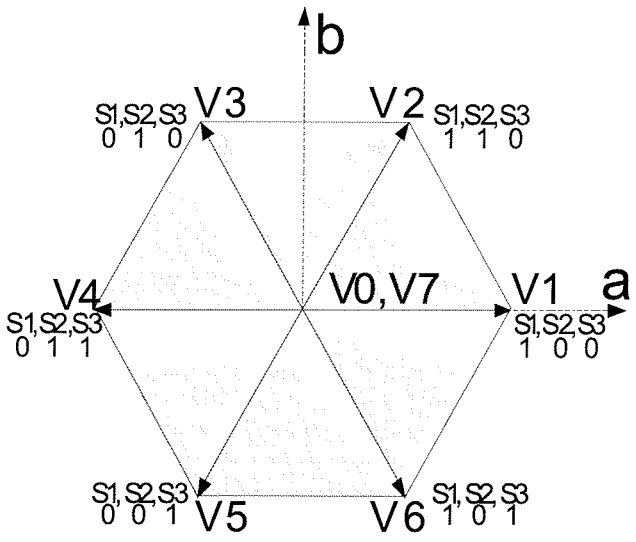

Slika 4. Šest aktivnih in dva ničelna vektorja v a-b koordinatnem sistemu

V dvofaznem a-b sistemu dobimo s pomočjo osmih različnih stanj stikalnih elementov vrednosti napetosti Usa in Usb (Tabela 2).

Tabela 2: Statorska napetost pri različnih stikalnih stanjih v a-b koordinatnem sistemu

S1	S2	S3	Usa	Usb	Vektor napetosti
0	0	0	0	0	0
1	1	1	0	0	V7
1	0	0	Udc	0	V1
1	1	0	$\frac{1}{2}Udc$	$\frac{\sqrt{3}}{2}Udc$	V2
0	1	0	$-\frac{1}{2}Udc$	$\frac{\sqrt{3}}{2}Udc$	V3
0	1	1	$-Udc$	0	V4
0	0	1	$-\frac{1}{2}Udc$	$-\frac{\sqrt{3}}{2}Udc$	V5
1	0	1	$\frac{1}{2}Udc$	$-\frac{\sqrt{3}}{2}Udc$	V6

5. Primerjava konvencionalnega z dogodkovnim histereznim vodenjem

Pri konvencionalnem tokovnem histereznem vodenju so najpogosteje uporabljeni dvo-nivojski histerezniki s konstantno histerezo. Samo delovanje dvo-nivojskega histereznika si lahko predstavimo s pomočjo diagrama stanj, kjer vidimo, da lahko ima izhod histereznika dve stanji 0 ali 1 (Slika 5). Za prehod iz enega v drugo stanje je potrebno doseči pogoj, ki pa je odvisen od širine histereze. Ko smo v stanju y=1, mora vhodni signal doseči manjšo vrednost od '-h' , da se pomaknemo v stanje y=0. Da lahko pridemo iz stanja y=0 v stanje y=1, pa mora vhodna vrednost preseči vrednost 'h'.

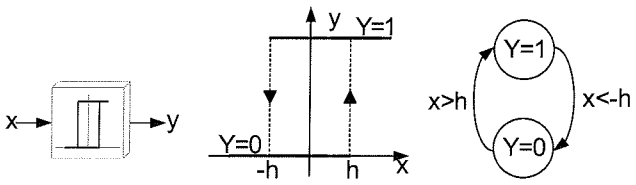

Slika 5. Delovanje dvo-nivojskega histereznika

V našem primeru je izhod posameznega histereznega regulatorja y_{hi} krmilni signal za tranzistorski stikali v pripadajoči veji pretvornika (Slika 6).

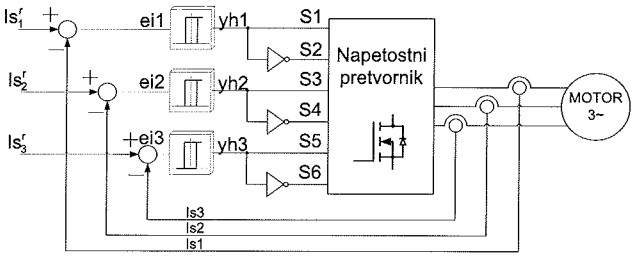

Slika 6. Blokovna shema konvencionalnega tokovnega vodenja

Stanje stikal v i-ti veji pretvornika je odvisno od tokovnega pogreška $e_{ii} = i_{si}^r - i_{si}$ in velikosti širine nastavljene histereze. Če je rezultat $i_{si}^r - i_{si} < -h$, potem je i-ta faza motorja priključena na pozitivni priključek enosmernega vira (prevaja zgornji tranzistor). Če pa je rezultat $i_{si}^r - i_{si} > h$, potem je i-ta faza motorja priključena na negativni priključek enosmernega vira (prevaja spodnji tranzistor). Glede na referenčno vrednost vidimo, da dejanski tok niha okoli referenčnega za velikost histereze. Tako lahko določimo valovitost toka, ki je v tem primeru enaka dvojni širini histereze 2h (Slika 7).

Takšen način vodenja lahko izvedemo tudi s pomočjo vpogledne tabele, pri čemer so vhodi v tabelo, ustrezno uteženi in sešteti, izhodi iz histereznih regulatorjev. Na izhodu tabele dobimo ustrezne krmilne signale za stikala S1 do S6, oziroma napetostne vektorje (Tabela 3).

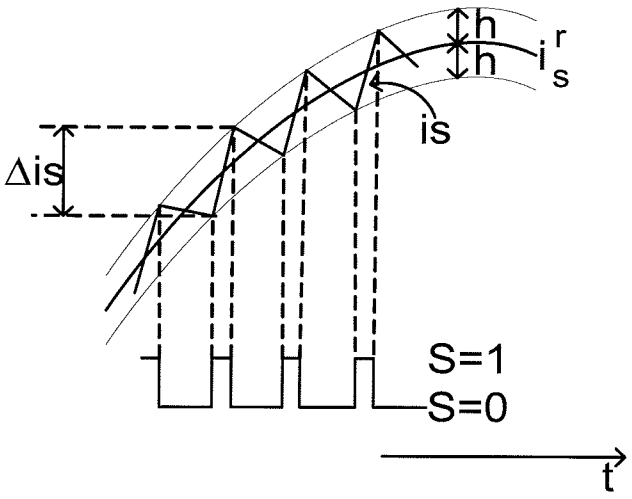

Slika 7. Referenčni in dejanski tok ter časovni potek preklopov stikala

Tabela 3: Določanje napetostnega vektorja iz izhodnih stanj histereznikov

$y_h = 4y_{h1} + 2y_{h2} + y_{h3}$	0	1	2	3	4	5	6	7
Napetostni vektor	V0	V5	V3	V4	V1	V6	V2	V7

Takšno histerezno vodenje je zelo preprosto in ne vsebuje zapletenih matematičnih operacij. Pri tem vodenju ne potrebujemo niti modulatorja, saj izhodi histereznikov neposredno krmilijo stikalni pretvornik. Zaradi vseh teh lastnosti pri histereznem vodenju ne potrebujemo zmogljivega mikroprocesorja, digitalnega signalnega procesorja ali kompleksnih električnih vezij. Poleg teh prednosti velja izpostaviti tudi dobro robustnost, neodvisnost delovanja od spremembe parametrov bremena, visoka dinamika in odsotnost sledilnega pogreška. Slaba lastnost pa je spremenljiva stikalna frekvenca, ki lahko povzroči tudi limitne cikle, ki pa povečujejo večje izgube pretvornika. Prav zaradi teh slabih lastnosti uvedemo dogodkovno histerezno vodenje.

6. Dogodkovno histerezno vodenje

Ko govorimo od dogodkovnem vodenju je potrebno najprej razložiti pojem dogodek. Opisano konvencionalno histerezno vodenje s tremi dvo-nivojskimi histereznimi regulatorji na statorskih tokovih lahko razumemo kot preprost primer dogodkovnega vodenja. Histerezni regulator v *i*-ti fazi detektira dva dogodka in sicer tokovni pogrešek je večji od histereze *h* in tokovni pogrešek je manjši od histereze -*h*. Na podlagi teh dogodkov pride do preklopa med tranzistorskima stikaloma v *i*-ti veji napetostnega pretvornika. Da bi lahko znižali število preklopov in odpravili limitne cikle bi morali nadzorovano preklapljati med napetostnimi vektorji. Z dogodkovnim vodenjem, ki temelji na konvencionalni izvedbi histereznega vodenja, zagotovimo nadzorovano preklapljanje med napetostnimi vektorji z novega dogodka, ki daje informacijo o napetostnem sektorju, v katerem se nahaja vektor referenčne napetosti u_s^r. To realiziramo tako, da vektor referenčne napetosti, ki predstavlja izhode tokovnih regulatorjev, realiziramo s pomočjo različnih časov dveh sosednjih aktivnih in ničelnima vektorjema. Katera dva aktivna vektorja bomo izbrali, pa določimo s pomočjo napetostnega sektorja v katerem se nahaja vektor referenčne napetosti. Izhod histereznikov y_n prav tako določa napetostni sektor, ki ga realizira napetostni pretvornik. Vendar pa imamo sedaj dodaten pogoj (stanje referenčne napetosti), ki odloči kateri vektorji bodo realizirani.

7. Dogodkovno histerezno vodenje s tremi aktivnimi vektorji

Aktivni so lahko le tisti trije vektorji, ki so znotraj referenčnega napetostnega sektorja (Slika 8).

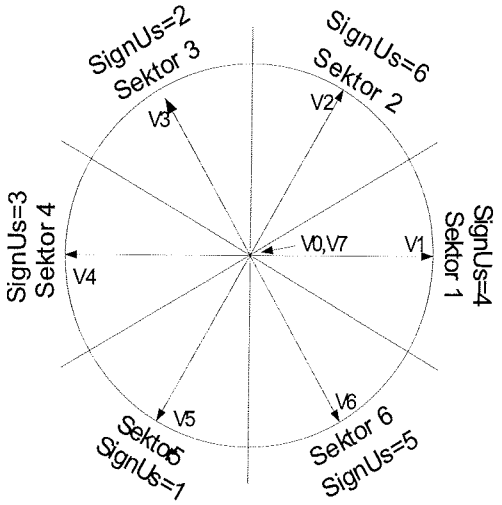

Slika 8. Napetostni vektorji in sektorji pri dogodkovnem vodenju s tremi aktivnimi vektorji

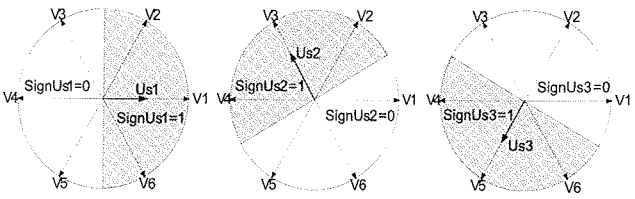

Slika 9. Predznaki napetosti prve, druge in tretje faze pri treh aktivnih vektorjih

Napetostni sektor kodiramo s spremenljivko Sign*Us* in predstavlja kar predznak faznih napetosti $u_{s1}^r, u_{s2}^r, u_{s3}^r$. Ko spremenljivke Sign*Us* ustrezno utežimo in seštejemo dobimo:

$$SignUs = 4 \cdot sign(u_{s1}) + 2 \cdot sign(u_{s2}) + sign(u_{s3}) \qquad (2)$$

Na ta način lahko izdelamo tabelo, ki nam prikazuje napetostne vektorje, ki jih uporabljamo v posameznem sektorju (Tabela 4).

Tabela 4: Trije aktivni vektorji v posameznem sektorju

Napetostni sektor	SignUs	Napetostni vektorji
Sektor 1	4	V0,V1,V2,V6,V7
Sektor 2	6	V0,V1,V2,V3,V7
Sektor 3	2	V0,V2,V3,V4,V7
Sektor 4	3	V0,V3,V4,V5,V7
Sektor 5	1	V0,V4,V5,V6,V7
Sektor 6	5	V0,V1,V5,V6,V7

Za stanja, ki so prepovedana pa uporabimo kar ničelne vektorje V0 ali V7.

8. Dogodkovno histerezno vodenje z dvema aktivnima vektorjema

Aktivna sta lahko le tista dva vektorja ki se nahajata znotraj referenčnega napetostnega sektorja, ki je zamaknjen za 30°. S tem dosežemo da lahko v sektorju 1 uporabljamo samo dva napetostna vektorja V1 in V2.

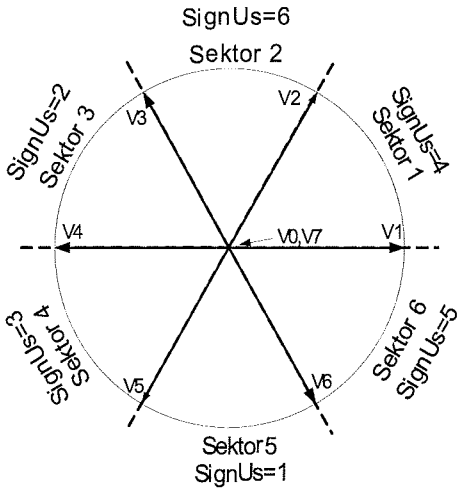

Slika 10. Napetostni vektorji in sektorji pri dogodkovnem vodenju z dvema aktivnima vektorjema

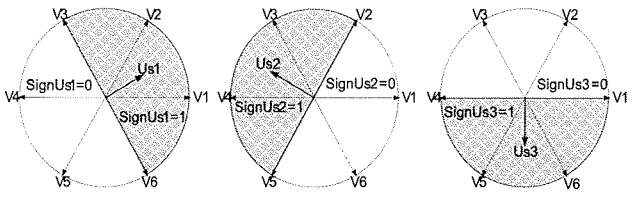

Slika 11. Predznaki napetosti prve, druge in tretje faze pri dveh aktivnih vektorjih

Napetostni sektor ponovno kodiramo s spremenljivko Sign*Us*, ki sedaj predstavlja predznak faznih napetosti **5**, ki so zamaknjene za 30°. Spremenljivke Sign*Us* ponovno ustrezno utežimo in seštejemo.

Tabela 5: Dva aktivna vektorja v posameznem sektorju

Napetostni sektor	SignUs	Napetostni vektorji
Sektor 1	4	V0, V1, V2, V7
Sektor 2	6	V0, V2, V3, V7
Sektor 3	2	V0, V3, V4, V7
Sektor 4	3	V0, V4, V5, V7
Sektor 5	1	V0, V5, V6, V7
Sektor 6	5	V0, V1, V6, V7

Na ta način lahko izdelamo novo tabelo, ki nam prikazuje aktivne vektorje, ki jih uporabljamo v posameznem sektorju (Tabela 5).

9. Rezultati simulacij in eksperimenta

Izvedeni so bili simulacijski rezultati na dveh različnih bremenih. Za simulacijsko orodje smo uporabili Matlab Simulink.

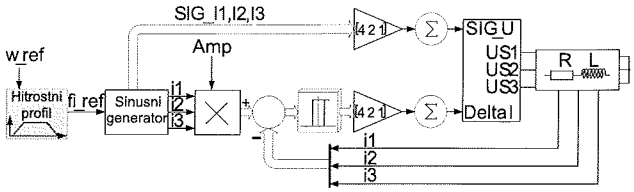

Slika 12. Blokovna shema dogodkovnega vodenja s tremi aktivnimi vektorji (Tabela 4)

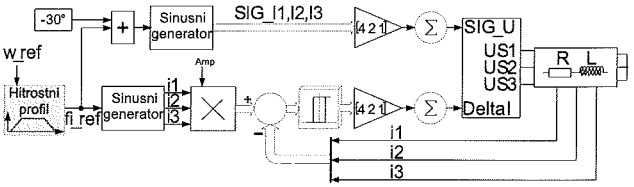

Slika 13. Blokovna shema dogodkovnega vodenja z dvema aktivnima vektorjema (Tabela 5)

Uporabili smo RL breme s parametri Rs=5Ω in Ls=1mH. Izmerili smo odzive tokov pri frekvenci 20Hz, amplitudi toka 0.4A in velikostjo histereze 20mA. Iz grafov je razvidno, da lahko s pomočjo dogodkovnega vodenja s tremi aktivnimi vektorji dosežemo zmanjšanje števila preklopov iz 14250 na samo 5606. Pri dogodkovnem vodenju z dvema aktivnima vektorjema pa število preklopov reduciramo na vrednost 3779. Ker so te meritve samo v eni delovni točki, smo naredili še meritve pri različnih referenčnih amplitudah toka (0.1A do 1.5A). Rezultati prikazujejo srednje število preklopov in srednji kvadratični pogrešek na časovno enoto 1ms. Srednje število preklopov definirano kot

$$SP_{1ms} = 10^{-3} \cdot f_{ref} \cdot SP \qquad (3)$$

Spremenljivka SP pa predstavlja število preklopov napetostnega vektorja. Srednji kvadratični pogrešek definiramo kot

$$SKP = \frac{1}{N}\sum_{n=1}^{N}(i_1^{*}[n] - i_1[n])^2 \quad (4)$$

kjer N predstavlja število odtipkov.

Zanesljivost simulacijskih rezultatov smo preverili tudi na eksperimentalnem modelu s pomočjo RL bremena. Rezultati eksperimentalnega modela (FPGA vezje) se ujemajo s simulacijskimi.

10. Sklep

Iz zgoraj podanih rezultatov je razvidno, da glede na konvencionalno histerezno vodenje pri dogodkovnem vodenju vsekakor zmanjšamo število preklopov v enakem časovnem intervalu. Vendar pa moramo biti pozorni tudi na valovitost toka, ki se zaradi manjšega števila preklopov poveča. Zato smo izvedli tudi analizo srednjega kvadratičnega pogreška, kjer vidimo, da pri dogodkovnem vodenju s tremi aktivnimi vektorji srednji kvadratični pogrešek celo zmanjšamo. V primeru dogodkovnega vodenja z dvema aktivnima vektorjema pa se manjše število preklopov pozna že tudi na srednjem kvadratičnem pogrešku, ki se precej poveča.

Tako lahko zaključimo z ugotovitvijo da je za zmanjšanje izgub zaradi velikega števila preklopov pri histereznem tokovnem vodenju smiselno uporabiti metodo dogodkovnega vodenja, ki pa mora vsebovati vsaj tri aktivne vektorje, ker se pri manj aktivnih vektorjih začne povečevati srednji kvadratični pogrešek.

Literatura

/1/ Frank Vahid, Roman Lysecky, VHDL for digital design, University of California, Riverside, University of Arizona, 2007

/2/ Digilent Nexys Board Reference Manual, Februar 2007

/3/ Pong P. Chu, FPGA prototyping by vhdl examples, Cleveland State University, 2008

/4/ Drago Dolinar, Gorazd Štumberger, Modeliranje in vodenje elektromehanskih sistemov, 2. izdaja, Maribor: FERI, 2004

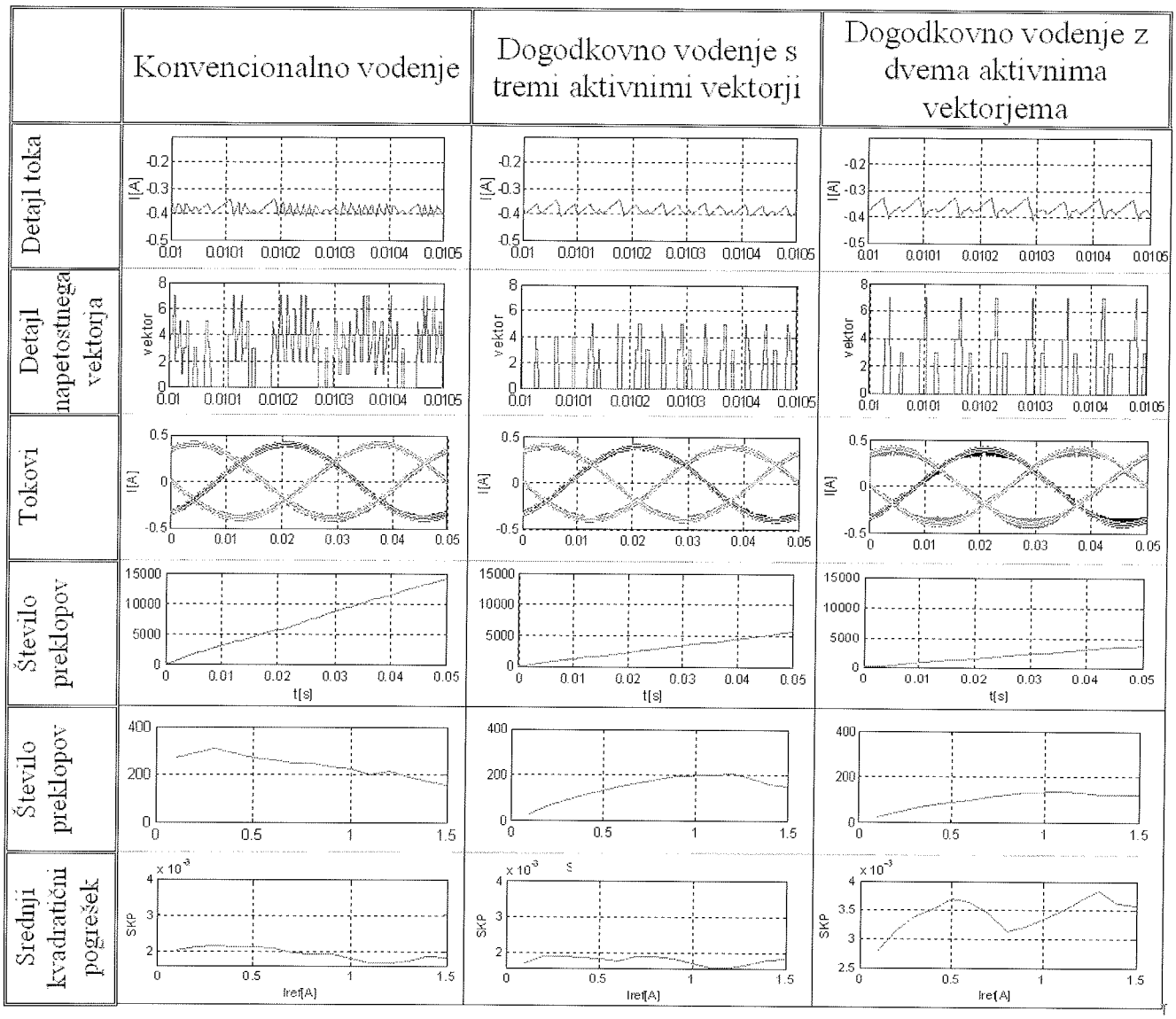

Slika 14. Primerjava rezultatov konvencionalnega in dogodkovnega vodenja z dvema in tremi aktivnimi vektorji

/5/ Ramadge P JG, Wonham W M, The Control of Discrete Event Systems, IEEE Tran. Ind. Electronics, 1989

/6/ C. Rossi, A. Tonielli, Robust Current Controller for Three-Phase Inverter using Finite State Automation, IEEE Tran. Ind. Electronics, Vol. 42, No.2, pp. 169-178, 1998

/7/ A. Polic, K Jezernik, Matrix based Event-Driven Approach for Current Control design of VSI, Proc. Of ISIE'05, Dubrovnik, pp. 917-922, Piscataway, New Jersej, IEEE, 2005

/8/ A. Tilli, A. Tonielli, Sequentional Design of Hysteresis Current Controller for Three-Phase Inverter, IEEE, Tran. Ind. Electronics, Vol. 45, No. 5, pp. 771-781, 1998

/9/ S. Berto, A.Paccagnella, M. Ceschia, S. Bolognani, M. Zigliotto, Potential and pitfalls of FPGA application in inverter drives - a case study, IEEE, Int. Conf. on Industrial Technology, ICIT'03, Vol.1, pp. 500-505, Dec. 2003

/10/ P.J.G., Ramadge, W.M. Wonham, The Control of Discrete Event Systems, Proceedings of the IEEE, Vol. 77, No. 1, pp. 81-99, 1989

/11/ E. Monmasson, M. N. Cirstea, FPGA Design Methodology for Industrial Control Systems - A Review, IEEE Trans. On Industrial Electronics, pp. 1824-1842, 2007

/12/ K. Zhou, D. Wang, Relationship Between Space-Vector Modulation and Three-Phase Carried-Based PWM: A Comprehensive Analysis, IEEE Transaction on Industrial Electronics, Vol. 49, No. 1, pp. 410-420, 2002

/13/ J. Boecker, Discrete-Event Converter Control, Proc. Of EPE, Toulouse, France, 2003

/14/ A. Polič, M. Rodič, K Jezernik, Matrix Based Approach to Overall Functionality Description of Drives, Proc. Of EPE-PEMC, Riga, Latvia, 2004

/15/ A. Polič, K Jezernik, Closed-Loop Matrix based Model of Discrete Event Systems for machine logic control design, IEEE Trans. Industrial Informatics, Vol. 1, No. 1, pp. 39-46, 2005

Robert Horvat, uni. dipl. inž. ,
Tel.: 00 386 2 220 7311, Fax: 00 386 2 220 7315,
e-mail: robert.horvat@uni-mb.si

redni prof. dr. Karel Jezernik
Tel.: 00 386 2 220 7300, Fax: 00 386 2 220 7315,
e-mail: karel.jezernik@uni-mb.si
Univerza v Mariboru, FERI,
Smetanova ulica 17, 2000 Maribor, Slovenija

Prispelo (Arrived): 10.07.2009 *Sprejeto (Accepted): 09.03.2010*

SYNTHESIS AND CHARACTERIZATIONS OF ZINC OXIDE NANOSTRUCTURES

Sharul Ashikin Kamaruddin[1,2], Mohd Zainizan Sahdan[1,3], Kah-Yoong Chan[2], Mohamad Rusop[3], Hashim Saim[1]

[1]Faculty of Electrical and Electronic Engineering, Universiti Tun Hussein Onn Malaysia, Johor, Malaysia.
[2]Faculty of Engineering, Multimedia University, Selangor, Malaysia.
[3]Faculty of Electrical Engineering, Universiti Teknologi MARA, Selangor, Malaysia.

Key words: Zinc oxide; ZnO; Nanostructures; Sol-gel; Large area electronics.

Abstract: Zinc oxide (ZnO) is an emerging optoelectronic material in large area electronic applications. We present the synthesis and the characterization of ZnO nanostructures. The ZnO nanostructures were synthesized using sol-gel hydrothermal technique on oxidized silicon substrates. The surface morphologies of the ZnO nanostructures were examined using scanning electron microscope (SEM) and atomic force microscope (AFM). The optical properties were measured using photoluminescence (PL) and ultraviolet-visible (UV-Vis) spectroscopies. The fabrication process and preliminary characterizations of the ZnO nanostructures will be described in this paper.

Sinteza in karakterizacija nanostruktur cinkovega oksida

Kjučne besede: cinkov oksid, nanostrukture, sol-gel, elektronika velikih površin

Izvleček: Cinkov oksid je nov optoelektronski material z možnostjo uporabe na področju elektronike velikih površin. V prispevku predstavljamo sintezo in karakterizacijo nanostruktur cinkovega oksida. Nanostrukture so bile sintetizirane z uporabo sol-gel hidrotermalne tehnike na oksidiranih silicijevih substratih. Površinske morfologije ZnO nanostruktur smo pregledovali s pomočjo vrstičnega elektronskega mikroskopa (SEM) in mikroskopa na atomsko silo (AFM). Optične lastnosti smo merili z uporabo fotoluminiscence (PL) in ultravijolične spektroskopije (UV-Vis). V članku so opisani tudi proces proizvodnje in preliminarne karakteristike nanostruktur cinkovega oksida.

1. Introduction

One-dimensional (1-D) zinc oxide (ZnO) nanostructures such as nanorods, nanoneedles, nanobelts and nanowires of desirable dimension have lately attracted significant attentions due to their unique electronic and optical properties compared to bulk structure /1-11/. The functional nanostructures posses excellent physical properties, owing to their geometry with high aspect ratio which modifies the light-matter interaction. The ZnO material has wide band-gap energy of 3.37 eV and large exciton binding energy of 60 meV, which make ZnO a promising candidate for many applications such as electronic, optoelectronic and information technology devices including sensors, displays, and solar cells /12/. However, in many applications both the size and the shape of the ZnO particles determine the material properties and therefore the performance of the devices /6,12/.

The 1-D nanostructured ZnO with different morphologies have been reported, for instances, nanorods, nanowires, nanobelts and quantum dots /1-11/. Several techniques have been employed to grow 1-D ZnO nanostructures, such as sol-gel technique, hydrothermal or solvothermal treatment, chemical precipitation method, molecular beam epitaxy and chemical vapor deposition. Among these techniques, the sol-gel method has distinctive advantages due to its lower crystallization temperature, ability to tune microstructure via sol-gel chemistry, conformal deposition ability, compositional control and large surface area coating capability /1/.

In this work, we realized the ZnO nanostructures using the sol-gel hydrothermal technique. The ZnO nanostructures were characterized using scanning electron microscope (SEM), atomic force microscope (AFM), photoluminescence (PL) and ultraviolet-visible (UV-Vis) spectroscopies. The ZnO nanostructures were formed on the oxidized silicon (100) substrates. The fabrication process and preliminary characterizations of the ZnO nanostructures will be described in this paper.

2. ZnO Fabrication Process

The fabrication process of the ZnO nanostructures is depicted in Figure 1. Silicon (Si) (100) substrate used for the growth of ZnO nanostructures was cleaned and etched in diluted hydrofluoric acid. The Si substrate was then rinsed and cleaned with de-ionized water. After that, the seed layer of silicon oxide (SiO_2) was grown on the Si substrate. The SiO_2 seed layer is necessary in order to enhance the growth of the ZnO nanostructures on the Si substrate, since there is a lattice mismatch between Si and zinc /13/. The oxidation process was carried out in 1 atmospheric ambi-

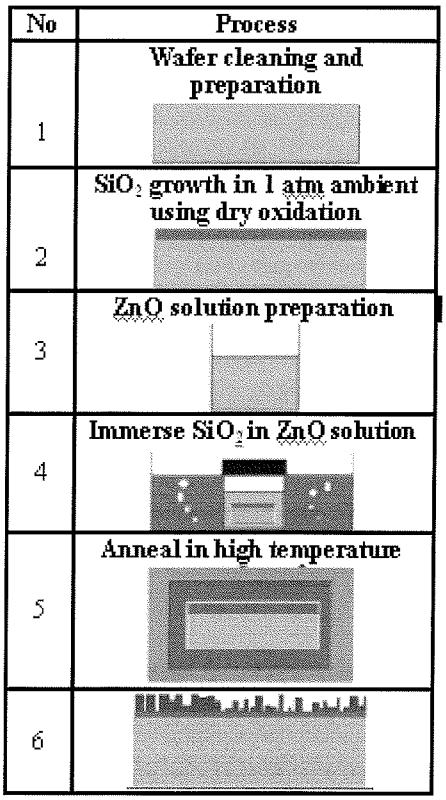

Fig. 1: Sol-gel hydrothermal fabrication process of the ZnO nanostructures.

ent and 900 °C for 20 minutes. Solution for ZnO nanostructures growth was prepared using an aqueous solution of zinc nitrate hexahydrate [$Zn(NO_3)_2.6H_2O$] mixed with hexamethylenetetramine [$C_6H_{12}N_4$] at molarity (M) of 0.01 M. The solution was diluted in 200 ml de-ionized water. The solution was then stirred at 60 °C for 2 hours and aged at room temperature for 24 hours. The oxidized Si substrate was immersed in the solution at 95 °C for 5 hours. After drying, the ZnO nanostructures coated oxidized Si sample was annealed at 500 °C for 1 hour.

The ZnO nanostructures coated sample was characterized for surface morphologies using scanning electron microscope (SEM) (JOEL JSM6380LA) and atomic force microscope (AFM) (Nanosurf EasyScan 2). The optical properties were measured using photoluminescence (PL) spectrometer (Horiba Jobin Vyon FluoroMax-3) and ultraviolet-visible (UV-Vis) spectroscopy.

3. Results and Discussion

The three-dimensional (3-D) surface morphological behavior of the nanostructured ZnO is demonstrated in the AFM micrograph, given in Figure 2 (a). Figure 2 (b) shows the SEM image of surface morphology of the ZnO nanostructures realized on oxidized Si substrate using precursor concentration of 0.01 M. The flower-shaped and rod-shaped ZnO nanostructures were observed in the SEM image. However, the ZnO nanorods apparently dominate

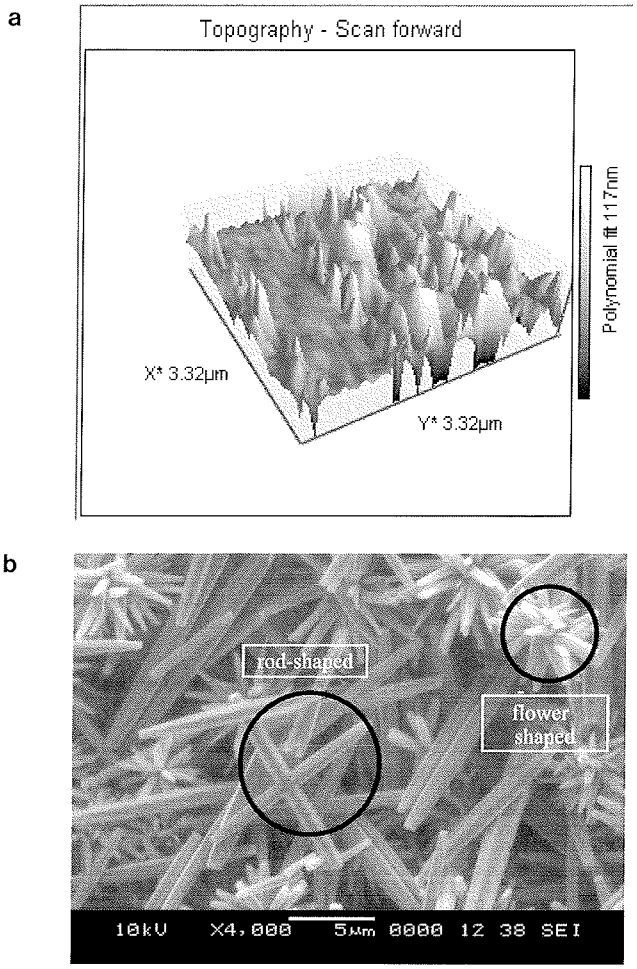

Fig. 2: a) AFM and b) SEM images measured for the ZnO nanostructures.

the surface of the sample. ZnO nanorods with moderate sizes were observed in the SEM image. The diameter of the nanorods is about 600 nm to 1 µm. Besides, the estimated length of the ZnO nanorods is around 5 µm and above.

Photoluminescene spectrum of ZnO nanostructures was measured at room temperature for wavelength ranging from

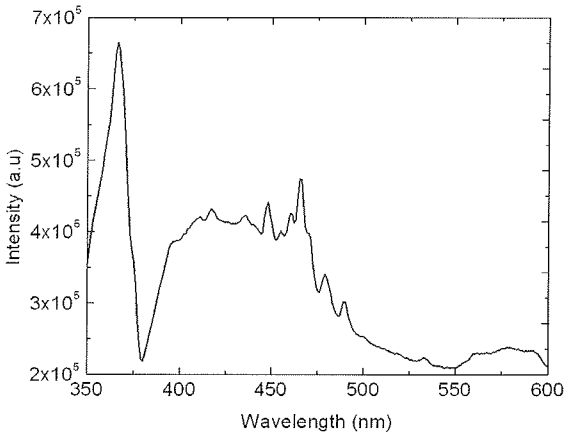

Fig. 3: The room temperature PL spectrum measured for the ZnO nanostructures.

350 nm to 600 nm, as shown in Figure 3. The PL spectrum contains sharp ultraviolet (UV) emission band at approximately 362 nm, which implies that the ZnO nanostructures exhibit high excitation at UV region. It is originated from recombination of exciton corresponding to the near-band gap emission of ZnO /2,5,8/. Figure 3 also shows that the PL spectrum exhibits the broad peak in the visible light range between around 400 nm to 500 nm. The broad band in the visible region is generally believed to associate with the intrinsic defects such as oxygen vacancies, zinc (Zn) interstitials or impurities /5,8,12/.

Figure 4 demonstrates the ultraviolet-visible absorption spectrum measured for the ZnO nanostructures for wavelength ranging from 200 nm to 800 nm. The sample in general has high absorption at UV region (below 400 nm), verifying the presence of the ZnO phases in the realized nanostructures, as shown in PL spetrum.

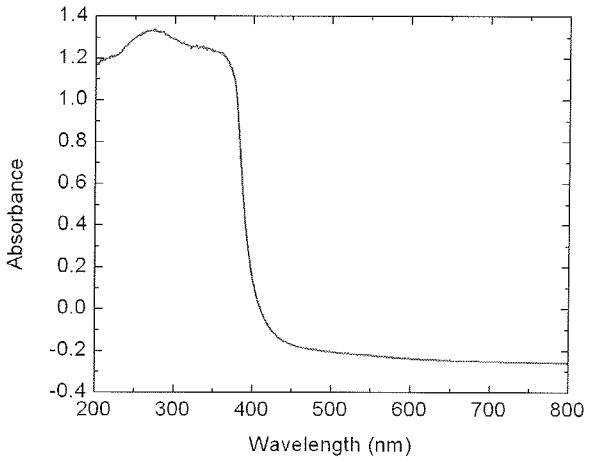

Fig. 4: The UV-Vis spectrum measured for the ZnO nanostructures.

4. Conclusion

ZnO nanostructures have been synthesized using low cost sol-gel hydrothermal technique on oxidized silicon substrates using a precursor's concentration of 0.01 M. The morphological and optical properties of the synthesized ZnO nanostructures were characterized. The scanning electron microscope and atomic force microscope images reveal flower-shaped and rod-shaped ZnO nanostructures, which are confirmed by the photoluminescence (PL) spectrometer and ultraviolet-visible (UV-Vis) spectroscopy measurements. The sol-gel processed ZnO nanostructures are promising material system for many emerging electronic and optoelectronic devices.

Acknowledgement

The Authors thank M. T. Nasir from Material Science Laboratory of University Tun Hussein Onn Malaysia (UTHM) for the technical assistances during the research project. This work is financially supported by Fundamental Research Grant (Vot No. 0214) from UTHM.

References

/1/ C. H. Bae, S. M. Park, S.-E. Ahn, D.-J. Oh, G. T. Kim, J. S. Ha, Sol-gel synthesis of sub-50 nm ZnO nanowires on pulse laser deposited ZnO thin films, Applied Surface Science 253 (2006) 1758-1761.

/2/ H. Zhong, J. Wang, M. Pan, S. Wang, Z. Li, W. Xu, X. Chen, W. Lu, Preparation and photoluminescence of ZnO nanorods, Materials Chemistry and Physics 97 (2006) 390-393.

/3/ Y. W. Heo, L. C. Tien, D. P. Norton, B. S. Kang, F. Ren, B. P. Gila, S. J. Pearton, Electrical transport properties of single ZnO nanorods, Applied Physics Letters 85 (2004) 2002-2004.

/4/ S. H. Lee, H. J. Lee, T. Goto, M.-W. Cho, T. Yao, Optical properties of porous ZnO nanorods grown by aqueous solution method, Materials Research Society Symposium Proceedings 957 (2007) 0957-K10-12.

/5/ G. Kenanakis, M. Androulidaki, E. Koudoumas, C. Savvakis, N. Katsarakis, Photoluminescence of ZnO nanostructures grown by the aqueous chemical growth technique, Superlattices and Microstructures 42 (2007) 473-478.

/6/ U. Pal, J. Garcia Serrano, P. Santiago, G. Xiong, K. B. Ucer, R. T. Williams, Synthesis and optical properties of ZnO nanostructures with different morphologies, Optical Materials 29 (2006) 65-69.

/7/ N. Lepot, M. K. Van Bael, H. Van den Rul, J. D'Haen, R. Peeters, D. Franco, J. Mullens, Synthesis of ZnO nanorods from aqueous solution, Materials Letters 61 (2007) 2624-2627.

/8/ M. A. Reshchikov, H. Morkoc, B. Nemeth, J. Nause, J. Xie, B. Hertog, A. Osinsky, Luminescence properties of defects in ZnO, Physica B 401-402 (2007) 358-361.

/9/ Z. Tao, X. Yu, J. Liu, L. Yang, S. Yang, A facile synthesis and photoluminescence of porous S-doped ZnO architectures, Journal of Alloys and Compounds 459 (2008) 395-398.

/10/ Q. Li, Z. Kang, B. Mao, E. Wang, C. Wang, C. Tian, S. Li, One-step polyoxometalate-assisted solvothermal synthesis of ZnO microspheres and their photoluminescence properties, Materials Letters 62 (2008) 2531-2534.

/11/ C. Wu, X. Qiao, L. Luo, H. Li, Synthesis of ZnO flowers and their photoluminescence properties, Material Research Bulletin 43 (2008) 1883-1891.

/12/ Klaus Ellmer, Andreas Klein, Bernd Rech, Transparent Conductive Zinc Oxide: Basics and Applications in Thin Film Solar Cells, Springer Series in Materials Science 104, published by Springer, Berlin, Germany (2008).

/13/ Y. Shen, W. Hu, T. Zhang, X. Xu, J. Sun, J. Wu, Z. Ying, N. Xu, Arsenic-doped ZnO films fabricated on silicon substrates by pulsed laser ablation, Materials Science and Engineering A 473 (2008) 201-205.

Sharul Ashikin Kamaruddin[1,2], Mohd Zainizan Sahdan[1,3], Kah-Yoong Chan[2], Mohamad Rusop[3], Hashim Saim[1]
[1]Faculty of Electrical and Electronic Engineering, Universiti Tun Hussein Onn Malaysia, 86400 Batu Pahat, Johor, Malaysia.
[2]Faculty of Engineering, Multimedia University, 63100 Cyberjaya, Selangor, Malaysia.
[3]Faculty of Electrical Engineering, Universiti Teknologi MARA, 40450 Shah Alam, Selangor, Malaysia.

Prispelo (Arrived): 27.07.2009 Sprejeto (Accepted): 09.03.2010

ASK COMPATIBLE CMOS RECEIVER FOR 13.56 MHZ RFID READER

Nissar Mohammad Karim[1], Mohd. Alauddin Mohd. Ali[1,2], Mamun Bin Ibne Reaz, Selina Abdul Samad

Institue of Microengineering and Nanoelectronics, Department of Electrical, Electronic and Systems Engineering, Universiti Kebangsaan Malaysia, Bangi, Selangor D.E., Malaysia.

Key words: ASK, RFID, Receiver, 13.56 MHZ, ISO/IEC 14443, CMOS.

Abstract: This study concerns about a high frequency companionable receiver architecture for RFID application, which is capable of dealing with most of the previous inadequacies. In this paper, an assessment of different receiver systems is shown and a simulated design of an integrated receiver for 13.56 MHz RFID Reader is proposed for 0.18μm CMOS technology. The design is mainly composed of amplifier, detector and digitizer. The system uses fewer components then that of other CMOS based RFID receivers and consumes a power of 0.325 mWatt at 1V biasing. Synthesized Results show smaller ripple (<0.0002%) than that of existing systems.

ASK kompatibilen CMOS sprejemnik za 13.56 MHz RFID bralnik

Kjučne besede: ASK, RFID, sprejemnik, 13.56 MHZ, ISO/IEC 14443, CMOS

Izvleček: Prispevek obravnava novo arhitekturo visokofrekvenčnega sprejemnika za RFID aplikacijo, ki odpravlja večino prejšnjih pomanjkljivosti. V tem članku je presojamo različne sprejemne sisteme in simuliramo koncept integriranega sprejemnika za 13.56 MHz RFID čitalnik izvedenega z 0.18μm CMOS tehnologijo. Sistem je sestavljen iz ojačevalnika, detektorja in digitalizatorja. Naprava uporablja manj komponent kot RFID sprejemnik na osnovi CMOS tehnologije ter porabi 0.325 mWatt moči pri napetosti 1V. Rezultati pokažejo manjši šum (<0.0002%) kot pri obstoječih sistemih.

1 Introduction

Radio Frequency Identification (RFID) system has been heralded as a technology fit for the 21st century, offering variety of applications. In modern time, there has been an escalating impact on the expansion of RFID technology for the localization and the identification of objects. RFID is a broadly used technology, which employs radio signals for the identification of people or objects. Its utility is to facilitate data to be transmitted into devices, which is interpreted by an RFID reader. Among the three focal constituents of RFID, reader is one which transmits the signal and processes the received data from the tag. Processing and receiving of data is carried out by the receiver. To do this, RFID reader needs to extract the message signal from the carrier and to digitize the resulting data. Our research goal is to design 13.56 MHz compatible receiver for RFID reader. For the design of a complimentary-metal-oxide-semiconductor (CMOS) based 13.56 MHz RFID receiver, one of the basic requirements is to follow ISO/IEC 14443 standardization.

According to ISO/IEC 14443 standardization, a design of an RFID receiver is proposed in this study. The carrier signal from the RFID tag will be 13.56 MHz with a subcarrier frequency of 847.5 KHz. The modulation index has to be either ASK(Amplitude Shift Keying) 10% or ASK 100%. On the other hand, low ripple, faster settling time and low power consumption are vital criterions in designing the system. So, the ultimate design challenge is to implement a receiver, which is compatible with ISO/IEC 14443 standardization, consumes less power, uses fewer components and shows low ripple.

From the recent literatures, we found, there were few researches on RFID receiver for high frequency (1MHz~20MHz) RFID operation. Though, till now, there are scopes to reduce ripple in detection and improve the performance in power consumption. Choi *et al.*, 2006 is one of those who accentuated on multi tag recognition and anti-collision protocols rather than focusing on detection and power consumption /2/. N.Roy *et al.*, 2006 delineated a mixed mode system by combining both digital and analogue components, which also overlooks the power criteria /3/. Meill'ere *et al.*, 2006 delineated a CMOS based 13.56 MHz RFID reader, whereas the receiver consists of rectifier, amplifier and comparator /4/. But, the number of MOSFETs used here is higher than those of the other receiver systems. The proposed demodulator by Y.Liu *et al.*, 2007 focused on FPGA implementation of receiver/5/ and like /2/, it did not consider the issue of detection. C. Mutti *et al.*, 2007 compared different detection algorithms, but this work was more towards theoretical implementation rather than real time nature /6/. One of the significant research execution was done by Alegre *et al.*, 2008 where a detector was designed, which can be

also used as a part of an RFID receiver /7/. This research is noteworthy because of its low ripple at the output. System designed by Seo *et al.*, 2008 showed an RFID reader, compatible for different standardization, though regarding ripple and settling time, it stated nothing /8/. From the literature review, we found that most of the researches went through either FPGA (Field Programmable Gate Array) implementation or theoretical execution. From the preceding literature review, we can say that, only few of these papers went through the practical design of receiver for 13.56 MHz RFID reader. So, our aim is to design a CMOS based RFID receiver which attunes with ISO/IEC 14443 standardization, employs fewer components, consumes less power and confirms less ripple.

2 Proposed Methodology

Fig 1 depicts the block diagram of the proposed receiver, which is mainly comprised of an amplifier, a detector, and a digitizer. The ASK modulated signal, coming from the tag has a carrier frequency of 13.56 MHz with a subcarrier frequency of 847.5 KHz. The OpAmp(Operational Amplifier) used in the amplifier, takes the ASK signal and boosts it up. The boosted up signal is then sent to the detector, which detects the peak and free the wave from the carrier. The digitizer compares the signal coming from the detector, with a reference voltage and shapes the wave. The output of the digitizer is set to a digital OR gate, which completely digitizes the wave. In the upcoming sections we are going to discuss the whole system in details.

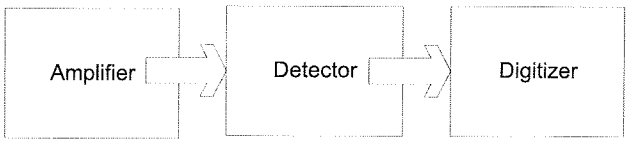

Fig 1 Block Diagram of the Proposed Receiver

2.1 Amplifier

We used amplifier in the receiver circuit to increase the power of the RF signal. It takes the signal from the tag via an antenna and a bypass capacitor. The bypass capacitor *C1* is used here to illuminate the DC component. This capacitor is connected with the positive terminal of the OpAmp/9/, whereas the OpAmp is constructed by transistors (*M1-M10*). The OpAmp mainly consists of three different components; which are 1. Differential Amplifier Block 2. Single Ended Conversion Block and 3. Gain Stage. The 1st block contains a differential pair (*M4,M5*), a current mirror (*M1,M3,M7,M8*) and a current source (*M2*). Current source is aided by active resistors (*M1 and M6*) to generate reference current for the current mirror. For obtaining high voltage gain, we used the current mirror. *M4* and *M5* are those inputs, which are used for inverting and non-inverting mode respectively. Capacitor *C0* is used to ensure stability for the feedback. The Single Ended Conversion Block produces a single output and gives necessary gain for the Gain Stage. The gain stage is comprised of *M3* and *M10*. The high output resistance of these two transistors brings a large gain. The OpAmp works in non-inverting mode. In case of non-inverting amplification in OpAmp, the gain can be given as,

$$G = 1 + R1/R2 \quad (1)$$

In equation (1), R1 is the feedback resistance and R2 is connected with ground and R1. The values of the resistors are set in such a way that, the gain gets attuned at a compatible range, which can give a proper amplification of power for the detector. Fig 2 shows the schematic of the amplifier.

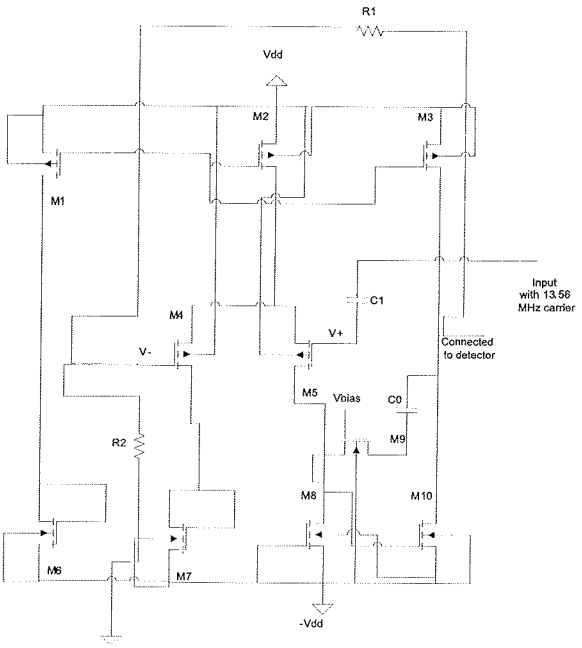

Fig 2 Schematic for the Amplifier

Table 1 shows the type, width and length of the MOSFETs used in the amplifier, where *M2* works as a current source and its' width (*W*) and length (*L*) are set in such a way that the reference current coming from *M2 is* 50 μA. At the same time, same amount of current passes through *M1,* as the *W* and *L* of *M1* is equal to that of *M2.* To obtain a higher current (twice of reference current) at *M3*, the width must be double than that of *M2.*The *W/L* ratio for *M7* and *M8* is set identical to obtain a mirror of the input current at output. *M3* and *M10* have a higher *W/L* ratio which helps to obtain a higher gain.

2.2 Detector

The detector illuminates the carrier and keeps only the message signal in an analogue form. The circuit mainly contains a PMOS *M11*, a resistor *R3* with two capacitors *C2* and *C3* respectively as depicted in Fig 3. *C3* acts as a bypass capacitor. Source and gate of the PMOS *M11* are shorted together, which forms a p-n junction. Its drain is connected to resistor *R3* and Capacitor *C3*.

Table 1 Type, Width and Length Of The MOSFETS

MOSFET	Type	Width(μm)	Length(μm)
M1	p-type	35.64	0.96
M2	p-type	35.64	0.96
M3	p-type	72	0.96
M4	p-type	7.44	0.96
M5	p-type	7.44	0.96
M6	n-type	1.56	3.12
M7	n-type	5.28	0.96
M8	n-type	5.28	0.96
M9	n-type	2.64	2.16
M10	n-type	21.12	0.96

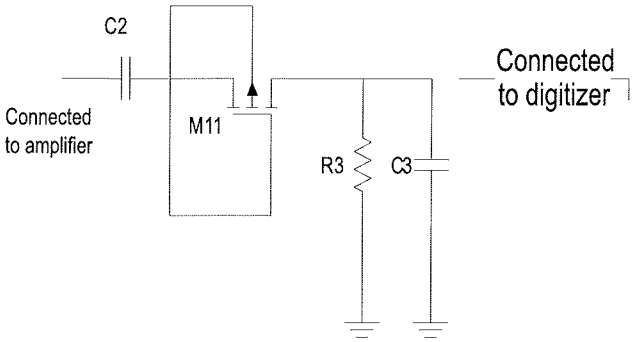

Fig 3 Schematic for the detector.

The configuration of detector is similar to a conventional envelope detector with a change in width (*W*) and length (*L*) for PMOS. To obtain a high drain current, *W/L* ratio is kept high. As *W/L* ratio is directly proportional to the drain current, when there is a high frequency input signal, the rectification and detection process become more accurate. On the other hand, the output of the detector is connected with an amplifier. Amplifier needs a high input current to be boosted up. Increasing *W/L* will give high output current for the detector. This can be explained by

$$I_{ds} = uC_{ox}(W/L)[(V_{gs} - V_t)V_{ds} - (V_{ds}/2)V_{ds}] \quad (2)$$

When

$0 < V_{ds} < V_{gs} - V_t$

Where,

I_{ds} = *Drain Current,*
u = *Mobility (Carrier),*
C_{ox} = *Oxide Capacitanc e,*
V_{gs} = *Gate to Source Voltage,*
V_t = *Threshold Voltage,*
V_{ds} = *Drain to Source Voltage*

From (2), it can be stated that I_{ds} is directly proportional to *W/L* ratio. Hence, increasing *W/L* will increase the drain current, which also provides high input current for the amplifier.

2.3 Digitizer

The digitizer compares the detected signal with respect to a reference voltage and passes the signal to an OR gate. In our proposed design, we employed an OpAmp(constructed of *M1-M10* in Fig 4) to execute the function of comparator, whereas the reference voltage was set with an inverting terminal of the OpAmp. The non-inverting terminal receives the signal coming from the detector. The endpoint of the comparator is affixed with an input of an OR gate. When the compared value is higher than that of reference voltage, the comparator gives a high signal. On the other hand, the comparator shows a lower signal; when the compared value is lower than that of reference voltage. The output generated from the comparator is sent to the OR gate to smooth the signal. The *W* and *L* of the transistors are equal to that of amplifier.

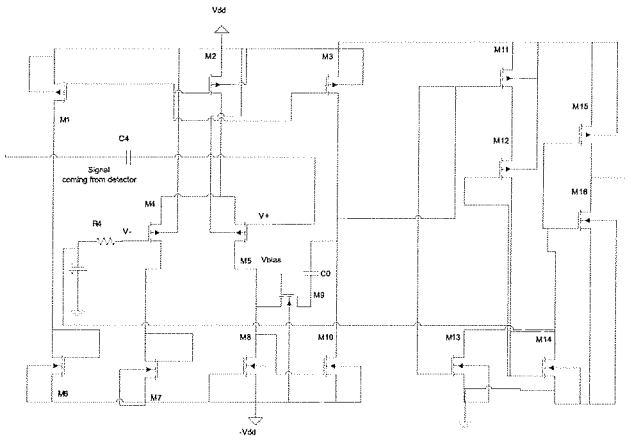

Fig 4 Schematic for the Digitizer

3 Results and Discussions

Mentor Graphics EldoSpice is used to simulate the proposed circuit in 0.18 μm CMOS technology, with one poly and two metal layers. Thick oxide layer is used to shield the transistors from high current. Each transistor is enclosed within its own individual deep well. The proposed

receiver is designed with the following component values: C0=100 fF, C1=10 nF, C2= 1000nF, C3=1nF, R1= 1K, R2= 1K and R3= 10K. Fig 5 shows the chip micrograph with an active area of 0.440200 mm2 (Including bonding pads).

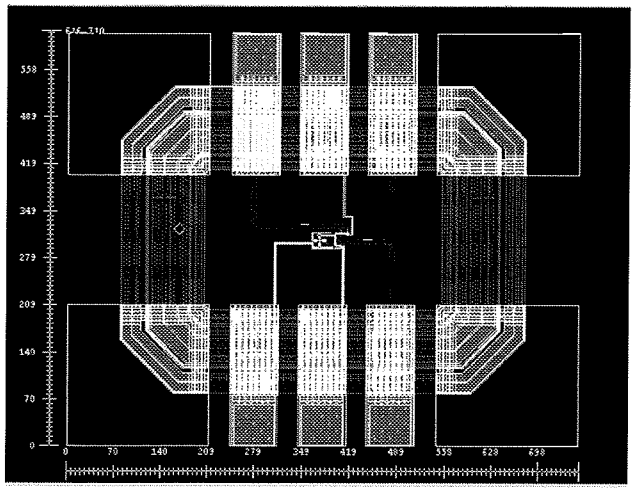

Fig 5 Chip Micrograph

The system is evaluated by using ASK modulated signal with a square-wave baseband and sine wave carrier signal. Fig 6(a) and 6(b) shows the representation for input and output voltage waveforms respectively. In simulation, it has been considered that the input waveform has 0.2V amplitude, 13.56 MHz carrier and 200 KHz baseband signal.

a

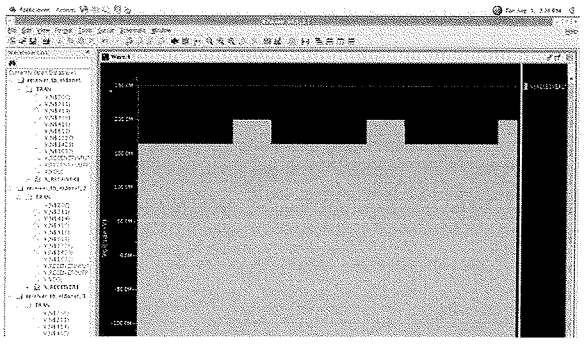

b

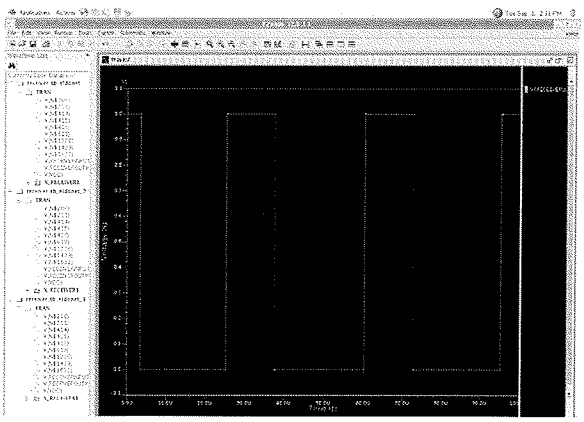

Fig 6 (a) Modulated Waveform (b) Receiver Output.

When this signal is used as an input, the output signal obtains a ripple of 0.005%. The ripple is appraised by taking the ratio of ripple voltage and dc voltage of the output waveform as shown in equation (3), where r stands for ripple, V_r is the ripple voltage and V_{dc} is the dc voltage.

$$r = \frac{V_r}{V_{dc}} \tag{3}$$

(3)Fig 7 shows the transfer characteristics, where noise (in dbc) vs. frequency graph is plotted. From this graph it is visible that at a very low frequency noise is high. As the frequency increases, the noise decreases. The frequency compatibility for the system is 5 KHz to 20 MHz.

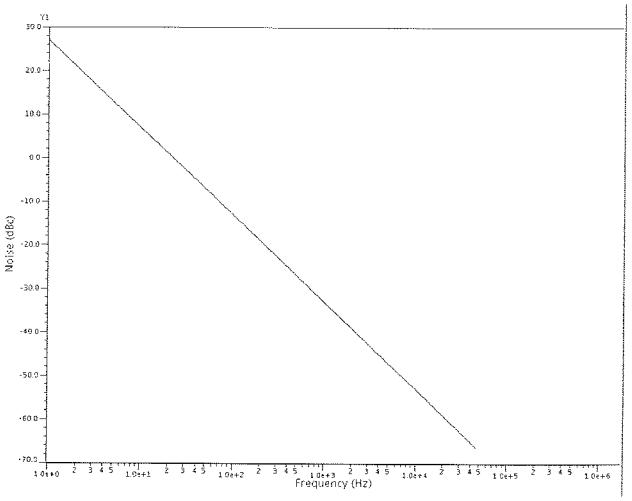

Fig 7 Noise Vs Frequency Graph

The receiver can extract the baseband signal from the carrier signal at 10% modulation index consuming 0.325 mWatt power. The total power consumption can be explicated by equation (4),

$$P_{tot} = P_s + P_d + P_{sc} \tag{4}$$

Here,

P_S = Static Power Consumption = n(Leakage Current X Supply Voltage)

P_d = Dynamic Power Consumption = $C_L V_{dd}^2 f_r$

P_{SC} = Short Circuit Power Consumption =

Where, n = Number of MOSFETs, C_L = Load Capacitance, V_{dd} = Biasing Voltage, f_r = Repetition Frequency, μ = Effective Surface Mobility, C_{ox} = Oxide Capacitance, V_t = Threshold Voltage.

Based on these facts and accessible data, Table 2 has been constructed which portrays the comparison between this work and the prior works in which our implemented demodulator shows better performance and accomplishes the requirements of ISO 14443 standardization.

Table 2 Comparison of the Prior Works

Source	Modulation Index(%)	Carrier (MHz)	Data Rate (Kbps)	Number of MOS	Power Consumption	Ripple Voltage at HF
Meill`ere *et al.* [6]	100	13.56	106	>40	5.3 mWatt	-
Alegre *et al.* [7]	100	10	-	>50	2.49 mWatt	0.3%
Seo et al. [8]	10, 100	13.56	106	>30	-	>1%
This Work	10	0.5 -13.56	106	21	0.325 mWatt	0.00019%

4 Conclusion

In this paper, an integrated receiver structure has been proposed for the use in a 13.56 MHz RFID reader. At 13.56 MHz frequency, the design shows less ripple and faster settling time than that of existing systems. Experimental results from the post-layout simulation are with good agreement on modulation index, frequency and data rate. So, it can be concluded that, the proposed system gives high-quality performance in terms of ripple and power consumption by following the standardization of ISO/IEC 14443.

References

/1/ N. Choi, H. Lee, S. Lee, and S. Kim, "Design of a 13.56 MHz RFID System," in Proceedings of the 8th International Conference on Advanced Communication Technology, Innsbruck, Austria, Vol. 1, pp.840 - 843, October 2006, DOI: 10.1109/ICACT.2006.206094.

/2/ N. Roy, A. Trivedi, and J. Wong, "Designing an FPGA-Based RFID Reader," XCell Journal, pp. 26-29, Second Quater 2006.

/3/ S. Meillčre, H. Barthélemy, M. Martin, "13.56 MHz CMOS transceiver for RFID applications," Analog Integrated Circuits and Signal Processing archive, Vol. 49, pp 249-256, December 2006, DOI: 10.1007/s10470-006-0392-8.

/4/ C. H. Y. Liu and H.Min, "Digital Correlation Demodulator Design for RFID Reader," in Wireless Communications and Networking Conference, WCNC 2007, Hingham, MA, USA, p.1664 - 1668, March 2007, DOI: 10.1109/WCNC.2007.313.

/5/ C. Mutti and A. Wittneben, "Robust Signal Detection in Passive RFID Systems," in Proceedings of the First International EURASIP Workshop on RFID Technology, Vienna, Austria, p.39 - 42, September 2007.

/6/ Alegre, J.P. Celma, S. Calvo, B. del Pozo, J.M.G., "Design of a Novel Envelope Detector for Fast-Settling Circuits,", IEEE Transaction on Instrument and Measurement, Volume 57, pp. 4-9, 2008. DOI: 10.1109/TIM.2007.909618.

/7/ Min-Woo Seo Yong-Chang Choi Young-Han Kim Hyung-Joun Yoo , "A 13.56MHz receiver SoC for multi-standard RFID reader" IEEE International Conference on Electron Devices and Solid-State Circuits, 2008. EDSSC 2008., Hong Kong, pp. 1-4, Dec. 2008. DOI: 10.1109/EDSSC.2008.4760718.

/8/ Pavan K Alli, "Testing a CMOS Operational Amplifier Circuit Using a ombinational of Oscillation and IDDQ Test Methods.", Master thesis, Agriculture and Mechanical College, Louisiana State University, 2004.

Nissar Mohammad Karim[1], Mohd. Alauddin Mohd. Ali[1,2], Mamun Bin Ibne Reaz, Selina Abdul Samad

Institue of Microengineering and Nanoelectronics, Department of Electrical, Electronic and Systems Engineering, Universiti Kebangsaan Malaysia, Bangi,Selangor D.E., Malaysia.
nissarkarim@yahoo.com

Prispelo (Arrived): 26.10.2009 *Sprejeto (Accepted): 09.03.2010*

AVTOMATIZIRANA PRETVORBA ZNAKOV ARABSKE ABECEDE IZ KODNEGA SISTEMA 0600-06FF V KODNI SISTEM PREZENTACIJSKE OBLIKE FE70-FEFF

Saša Klampfer, Peter Šamperl, Zdenko Mezgec, Amor Chowdhury

Margento R&D d.o.o., Maribor, Slovenija

Kjučne besede: mPOS, kodni sistemi, arabska abeceda, arabski znaki, pretvorbe, translacijska matrika, pravila, plačilni terminal, zaslon, hexadecimalni zapis, inverzna pretvorba, terminalsko orodje, translacijsko orodje, enostopenjsko pravilo, večstopenjsko pravilo.

Izvleček: Razširjenost brezgotovinskega plačevanja z mobilnimi telefoni preko mPOS plačilnih terminalov postaja vse bolj aktulno in priročno. Razvite rešitve se lansirajo tako na domače, kot tuje trge. Z lansiranjem rešitev na tržišča bližnjega vzhoda, pa so se pojavile specifične potrebe po podpori arabskih jezikov v menijih mPOS plačilnih terminalov. Članek opisuje enega izmed možnih načinov pretvarjanja arabskih znakov iz kodnega sistema 0600-06FF v prezentacijske forme arabskih znakov, ki se nahajajo v kodnem sistemu FE70-FEFF. V prvem delu smo se omejili predvsem na problematiko prikazovanja arabskih znakov na zaslonu terminala, ki se nahajajo v kodnem zapisu 0600-06FF. Iz tega razloga smo predstavili rešitev, ki se navezuje na pretvorbo arabskih znakov kodnega sistema 0600-06FF v kodni sistem arabskih prezentacijskih form FE70-FEFF. Na osnovi tega smo v nadaljevanju na praktičnih primerih predstavili rešitev pretvorbe v dveh korakih. Najprej se pretvorba izvrši preko translacijske matrike, v drugem koraku pa se pretvorjen zapis preko translacijske matrike primerja z ekvivalentnim originalnim arabskim zapisom. Na osnovi primerjave in ugotovljenih odstopanj se zasnujejo pravila po katerih se izbirajo oblike črk, glede na predhodno črko v besedi. Vsak predstavljen korak smo obrazložili na številnih praktičnih primerih. V članku predstavljamo tudi koncept izbire in aktivacije pravila, ki je povsem identičen ekspertnim sistemom, ki temeljijo na osnovi produkcijskih pravil. V drugem delu smo se osredotočili na jasno predstavitev posameznih rešitev, ki jih uporabljamo za konfiguracijo mPOS plačilnega terminala, kamor smo umestili tudi razvit produkt in njegove funkcionalnosti. V zadnjem delu smo se omejili predvsem na prikaz pretvorjenih besed v kodni zapis FE70-FEFF na zaslonu mPOS terminala.

Arabic characters automatic translation from 0600-06FF code system to Arabic presentation forms code system FE70-FEFF

Key words: mPOS, code systems, Arabic alphabet, Arabic signs, conversions, conversions matrix, rules, payment terminal, screen, hexadecimal record, inverse conversion, terminal tool, conversion tool, single rule, multiple rule.

Abstract: Prevalence of non-cash payment with mobile phones via mPOS payment terminal is becoming increasingly important and convenient. The developed solutions are ready to launch on the domestic and foreign markets. With the launch of a different solutions to the Middle Eastern markets, have emerged to support the specific needs upon the Arab language in the menus of mPOS payment terminals. This paper describes one possible way to convert the Arab characters from code page 0600-06FF into the Arabic presentation forms which are specified in FE70-FEFF code page. In the first part of the article, we are limited primarily to the problems which concerns correct displaying Arabic words (written in 0600-06FF code system) on the terminal screen. For this reason, we presented a solution which is tightly connected with the transformation of the Arab characters from 0600-06FF code system into the FE70-FEFF Arabic presentation form code page. On this basis, we present a solution on practical examples which is constructed with two steps. First step presets conversion over conversion matrix, meanwhile in second step we compare converted word (FE70-FEFF) with the original one (0600-06FF). Based on a comparison of the anomalies the rules are created and written into conversion setup file. The rules are created on the following way: for temporary char (FE70-FEFF), system observe char which is before it and then temporary char compares with original (0600-06FF) one shape. If there are differences in shape, then system produces rule which contains proper shape of temporary char correspond to char before it. All described is explain on practical examples. During this paper we present the concept of rules creation, selection and activation, which is completely identical to the expert system based on production rules. In the second part, we focused on a clear presentation of individual solutions that are used to configure mPOS payment terminal, where we place our well-developed product and its functionality. In the last part, we have limited primarily to see how the converted words (FE70-FEFF) looks like on the screen of the mPOS terminal.

1. Uvod

Brezgotovinsko plačevanje z mobilnim telefonom je zaradi razširjenosti mobilne telefonije postalo tržno zanimivo. Razvile so se različne tehnologije, ki omogočajo mobilno plačevanje. MPay je eden od sistemov mobilnega plačevanja, ki ga je razvilo podjetje Ultra d.o.o.. Sistem temelji na osnovi prenosa podatkov po govornem kanalu različnih mobilnih omrežij, kot so GSM, CDMA in UMTS. Glede na različne plačilne storitve, ki jih omogoča MPay sistem, se na trgu uporabljata dva tipa terminalov, in sicer aPOS ter mPOS. Osnova obeh terminalov je enaka, razlika je v tem, da ima mPOS terminal vgrajen uporabniški vmesniki (tipkovnica, zaslon, tiskalnik). aPOS terminal se najpogosteje uporablja v restavracijah, trgovinah, taksiji,..., in ne vsebuje grafičnega uporabniškega vmesnika, zato za našo razvito aplikacijo ni primeren. aPOS terminal ima vgrajene različne komunikacijske vmesnike, ki omogočajo priklop na razne prodajne avtomate, parkirne ure, igralne avtomate,... Na novo razvita aplikacija se seveda nanaša na mPOS plačilne terminale, ki razpolagajo z uporabniškim vmesnikom s sposobnostjo prikazovanja različnih jezikov.

Ideja za strokovni prispevek je nastala na podlagi vse večje potrebe podjetja Margento R&D d.o.o., ki razvija sisteme brezgotovinskega plačevanja z mobilnimi telefoni preko mPOS terminalov za celotno svetovno tržišče. V večini priemerov se na mPOS terminalih podpre večjezična podpora. S pridobitvijo razvojnih projektov za področje Združenih Arabskih Emiratov se je v podjetju pojavila potreba implementacije arabskega jezika na plačilne terminale. Problematika s katero smo se srečali se nanaša na sposobnost prikazovanja arabskih znakov na plačilnem terminalu T4000.

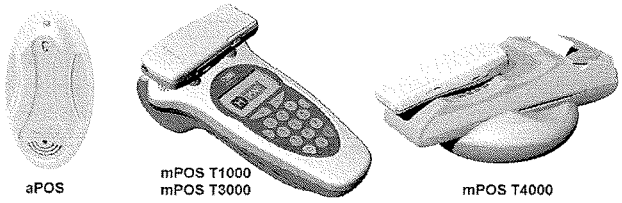

Slika 1: Prikaz aPOS in mPOS terminalov

Postopek priprave izpisov, ki se prikazujejo na zaslonu plačilnega terminala se prične z osnovno excel datoteko. Npr. V koloni 'A' se nahajajo npr. angleški izrazi, v koloni 'G' pa arabski izrazi, ki jih preko arabske tipkovnice zapiše prevajalec. Privzeto se arabski znaki, ki se vnašajo preko arabske tipkovnice nahajajo v kodnem zapisu 0600-06FF /1/. Z združevanjem znakov iz omenjenega kodnega sistema, črke spreminjajo obliko, glede na lokacijo v besedi in glede na tip predhodne in zaporedne črke. To pomeni, da črka spremeni obliko, vendar v hexadecimalnem zapisu, le ta še vedno ohranja enako *'hexa'* vrednost, kljub temu, da se je črki spremenila oblika. To je tudi glavni problem na katerega naletimo pri implementaciji arabskega jezika na plačilni terminal (mPOS). Le ta ne pozna pretvorbe črk, glede na predhodnjo in naslednjo črko, zato jo prikaže nepovezano v obliki samostoječe črke (beseda kot končni produkt ne izgleda povezano, temveč vsaka črka stoji sama zase). Tekom študije smo prišli do zaključka, da je za pravilno prikazovanje arabskega jezika na plačilnem terminalu, potrebna pretvorba znakov arabske abecede iz kodnega sistema 0600-06FF v prezentacijsko obliko arabskega kodnega sistema FE70-FEFF /5/. Le ta vsebuje kodne znake, ki upoštevajo lokacijo črke v besedi. To pomeni, da za vsak znak arabske abecede v kodnem sistemu 0600-06FF obstajajo štiri različice zapisa istega znaka v prezentacijskem /2/ arabskem kodnem sistemu FE70-FEFF. Takšne štiri različice se navezujejo na lokacijo arabskega znaka v besedi, in sicer: začetna črka besede, vmesna črka besede, končna črka besede in osamljena (izolorana/samostoječa) črka abecede (vsaka ima svojo obliko).

Ker arabsko tržišče predstavlja enega izmed najpomembnejših področij uvajanja sodobnih načinov brezgotovinskega plačevanja, je bilo za nas izrednega pomena razviti avtomatizirano rešitev za pretvorbo znakov arabske abecede v prezentacijsko formo, saj podobne programske rešitve, ki bi bile sposobne izvesti opisano pretvorbo, ne obstajajo.

Pri razvoju tako imenovanega *'translacijskega'* orodja smo šli še korak dlje v smeri avtomatične priprave t.i. *'printout'* datotek, preko katerih v interni pomnilnik plačilnega terminala naložimo izraze različnih jezikov (npr. angleški in arabski jezik). Povzetek pregleda operabilnosti in funkcionalnosti sistema bomo na kratko predstavili v nadaljevanju.

V drugem poglavju predstavljamo definicijo problema in osnovno problematiko pretvorbe arabskih znakov iz enega kodnega sistema v drug kodni sistem. V okviru tretjega poglavja bomo predstavili metodologijo pretvorbe in t.i. 'translacijsko' matriko z upoštevanjem pozicij posameznih črk v besedi. Četrto poglavje je namenjeno predstavitvi drugega koraka, ki upošteva pravila predhodne in zaporedne črke glede na trenutno črko, in s tem pripomore k pravilni pretvorbi arabskih izrazov v kodni sitem FE70-FEFF. V petem poglavju predstavljamo pomembne korake od pretvorbe arabskih znakov do postopka naložitve le teh v flash pomnilnik mPOS terminala. Šesto poglavje je namenjeno predstavitvi funkcionalnosti razvite rešitve in njenih režimov delovanja. V sedmem poglavju so prikazani rezultati razvitega orodja, medtem ko z osmim sklepnim poglavjem zaključujemo članek.

2. Definicija problema in osnovna problematika

Kot smo že v uvodu nakazali, se osnovna problematika navezuje na razširitev trženja razvitih tehnologij na tuja tržišča, predvsem pa na tržišče Združenih Arabskih Emiratov. S prodorom na tuje trge se pojavlja potreba po več jezični podpori. Zaradi specifike arabskega jezika, in omejitev programske opreme mPOS terminala smo morali razviti univerzalno rešitev, ki nam bo v veliko pomoč pri lansiranju nadalnjih produktov na omenjeno tržišče.

Omejitev programske opreme plačilnega terminala mPOS se navezuje na nesposobnost prikazovanja znakov arabske abecede, ki se nahajajo v izvornem kodnem sistemu 0600-06FF (slika 2).

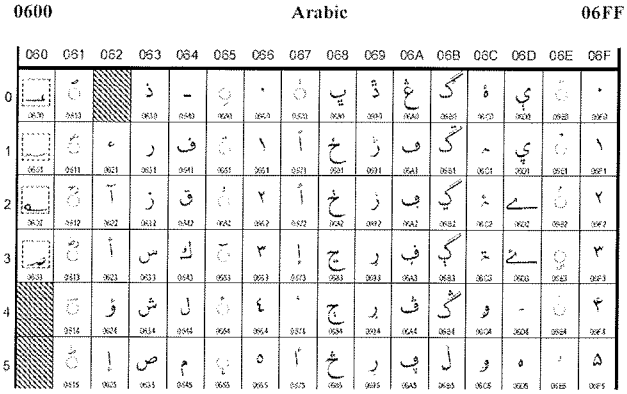

Slika 2: Izsek kodne tabele 0600-06FF z arabskimi znaki /7/

Uvodoma smo omenili, da osnovni element med nami in prevajalcem v arabski jezik predstavlja excel datoteka. Vsak preveden izraz v excel datoteki je zapisan v 0600-06FF kodnem zapisu (gledano hexadecimalno). Lastnost takšnega zapisa je avtomatsko prilagajanje in spreminjanje oblike črk /4/, glede na predhodno in zaporedno zapisasno črko. Naj spomnimo, da je lastnost arabske pisave tudi zapis od desne proti levi, za razliko od našega jezika, v katerem pišemo od leve proti desni. Da bo opisan princip čimbolj nazoren si poglejmo naslednji primer:

Tabela 1: Spreminjanje oblike arabskih črk pri proceduri združevanja

Samostojna črka (0600-06FF)	Samostojna črka (0600-06FF)	Združeni črki (0600-06FF)
ف	ي	في

Na zgornjem primeru je lepo razviden status in oblika samostoječih (skrajno levi in arabski znak na sredini - glej tabelo 1) arabskih črk iz kodnega sistema (0600-06FF), ter spremenjena oblika znakov v primeru zapisa obeh, enega za drugim. S pregledom hexadecimalnega zapisa /6/ združenih znakov v besedo, pa le ta še vedno ohranjata izvirni hexadecimalni zapis, kljub spremenjeni obliki črk.

Tabela 2: Hexadecimalna vrednost posameznih ter združenih arabskih znakov

Samostojna črka (0600-06FF)	Samostojna črka (0600-06FF)	Združeni črki (0600-06FF)
ف	ي	في
Hexadecimalni zapis arabskih znakov		
0641	064A	0641 064A

Iz zgornjega primera je že lepo razvidna problematika, s katero smo se srečali pri prikazovanju arabskih izrazov na zaslonu terminala. Kljub združenim črkam in spremenjeni obliki le te še vedno ohranjajo kodni hexadecimalni zapis v takšni formi, kot da črka stoji samostojno in ni vezana na druge črke v zapisani besedi (kljub avtomatski spremembi oblike ob zapisu dveh zaporednih arabskih znakov). Iz tega razloga je tudi prikaz na zaslonu terminala napačen.

Rešitev za takšen problem najdemo v arabskih prezentacijskih znakih, ki so zapisani v kodnem zapisu FE70-FEFF. Takšen kodni zapis vsebuje za vsak znak iz 0600-06FF vse oblike tovrstnega znaka glede na pozicijo v besedi (samostojni zank, na začetku besede, na koncu v sredini). Da bo razlaga še bolj jasna, si oglejmo primer za arabski znak *FEH* (0641):

Marsikomu se na tem mestu porodi ideja, da je potrebno spremljati pozicije črk v besedi iz kodnega sistema 0600-06FF, in na osnovi teh pozicij nato izbiramo črke iz kodnega sistema FE70-FEFF. To je deloma pravilno, in tudi to metodologijo, ki jo bomo razložili v nadaljevanju uporabljamo tudi mi. Vendar pa končna rešitev ni tako trivialna in enostavna, kot smo jo ravnokar navedli. Problematiko dodatno otežijo še dejstva, da je v FE70-FEFF kodnem sistemu potrebno upoštevati še dodatna pravila, katera črka je pred in za pretvorjeno.

Tabela 3: Primerjava hexadecimalnih zapisov oblike arabske črke FEH *v obeh kodnih tabelah*

Kodni sistem 0600-06FF				
Črka	*Osamljena*	*Začetek*	*Sredina*	*Konec*
FEH	ف			
0641	*0641*	*0641*	*0641*	*0641*
Kodni sistem FE70-FEFF				
FEH	ف	فـ	ـفـ	ـف
0641	*FED1*	*FED3*	*FED4*	*FED2*

Tipičen primer upoštevajoč samo pozicije znakov brez upoštevanja dodatnih pravil pretvorbe daje napačen rezultat (glej tabelo 4). Vendarle pa nam je bil takšen način v veliko pomoč pri postavljanju pravil za drugi način pretvorbe, ki upošteva tako pozicijo kot tudi pravila. Iz tega razloga je potrebno za pravilne pretvorbe zasnovati še dodatna pravila, ki pripomorejo k točnemu končnemu rezultatu. V sredinski koloni tabele 4 sta z rdečo barvo prikazani arabski črki zapisani v kodnem zapisu FE70-FEFF, ki sta bili vpeljani z upoštevanjem pozicije brez dodatnih pravil, le ti pa sta napačni.

Tabela 4: Pretvorba v FE70-FEFF kodni sistem z upoštevanjem samo pozicije (sredinska kolona) ter z uportevanjem pozicije in dodatnih pravil (desna kolona)

Originalen arabski izraz 0600-06FF	**Pretvorba z upoštevanjem pozicije FE70-FE77**	**Upoštevana dodatna pravila Pretvorbe FE70-FE77**
افخ	اﻓـخ	افخ
	Napačno	*Pravilno*

3. Potek pretvorbe z upoštevanjem pozicije

Logiko pretvarjanja izrazov iz 0600-06FF v FE70-FEFF smo zasnovali v programskem jeziku C# /3/.

Da bo predstava lažja, bomo potek tovrstne pretvorbe opisali na primeru arabske besede, ki jo sestavljajo arabski znaki iz 0600-06FF. Logika programa je v prvi fazi zasnovana tako, da besedo najprej razdeli na posamezne arabske znake, ki le to sestavljajo in jih zapiše v tako imenovane tipizirane liste, pri čemer ohranja zaporedje črk (od desne proti levi). V kolikor gre za stavek, le tega najprej razdruži na posamezne besede, nato pa vsako besedo v posamične črke, ki se ponovno zapišejo v pripravljene podatkovne strukture. Temelj pretvarjanja je torej razdružtev stavka na

besede in nadalje besede na posamične črke. Na tem mestu se marskomu pojavi vprašanje zakaj besedo razdeliti na posamezne črke? Odgovor je sila preprost. Za pretvorbo črke iz 0600-06FF v FE70-FEFF uporabljamo translacijsko matriko v naslednji obliki:

Tabela 5: Izsek iz sestavljne translacijske matrike

Original (hex)	Končna črka (hex)	Začetna črka (hex)	Vmesna črka (hex)	Izolirana črka (hex)
0641	*FED2*	*FED3*	*FED4*	*FED1*
0642	*FED6*	*FED7*	*FED8*	*FED5*
062B	*FE9A*	*FE9B*	*FE9C*	*FE99*
0635	*FEBA*	*FEBB*	*FEBC*	*FEB9*
0636	*FEBE*	*FEBF*	*FEC0*	*FEBD*
0643	*FEDA*	*FEDB*	*FEDC*	*FED9*
0645	*FEE2*	*FEE3*	*FEE4*	*FEE1*
0646	*FEE6*	*FEE7*	*FEE8*	*FEE5*
062A	*FE96*	*FE97*	*FE98*	*FE95*
...	...	...	...	...

Posamezno črko iz besede (0600-06FF), ki smo jo v predhodnem koraku razdelili pretvorimo v hexadecimalni zapis, in upoštevamo njeno pozicijo. Pozicije ovrednotimo s števili, kjer število *0* predstavlja začetno črko besede, število *x* pa končno črko besede. Vsa vmesna števila med *0* in *x* predstavljajo pozicije vmesnih črk. Po takšnem markiranju lahko pri nadalnji obdelavi ugotovimo, lokacijo posamezne črke.

V naslednji fazi implementirana logika v translacijski matriki (Tabela 5) v koloni *Original (hex)* poišče istoimensko hexadecimalno vrednost, kot jo ima npr. začetna črka besede. Ko logika najde ujemanje, preveri indeks pozicije, na osnovi katerega s podpravili oblike *if* in *then* poišče ustrezni hexadecimalni zapis črke v isti vrstici translacijske matrike. Če se ozremo na tabelo 5 in predpostavimo, da imamo opravka z začetno črko besede, ki ima hexadecimalno vrednost *0641* bo logika v isti vrstici glede na poznan indeks črke izbrala hexadecimalno vrednost iz kolone *Začetna črka (hex) FED3*. S podobno logiko operiramo tudi v primeru stavkov itd. V primeru osamljene črke pa je logika nekoliko drugačna, saj preveri ali osamljena črka vsebuje še kakšno črko, ki se nahaja za njo. Če takšna črka ne obstaja jo markira kot izolirano, in po enakem principu poišče ekvivalent FE70-FEFF preko translacijske matrike. Procedura se po takšnem principu ponavlja, dokler niso pretvorjeni vsi arabski izrazi, besede, stavki...

Rezultat takšne pretvorbe je prikazan v tabeli 4 - sredinska kolona.

4. Princip zasnove pravil s pomočjo rezultatov predhodne metode

Na osnovi primerjave rezultatov predhodne metode z arabskimi izrazi, ki se nahajajo v excel datoteki (originalni izrazi), lahko zasujemo tabelo pravil za vsako posamezno črko, glede na njeno zaporedno in predhodno črko. Logika snovanja matrike pravil je sledeča. Z orodjem za primerjavo datotek, primerjamo ustvarjeno 'printout' datoteko po prvi metodi z originalno excel datoteko. Na besedah, ki se razlikujejo izvršimo analizo in hkrati snujemo matriko pravil za posamezno črko. Naprimer, primerjajmo spodnja izraza, kjer je levi pravilen, desni pa po predhodni metodi brez pravil napačno pretvorjen.

افخ افخ

Desni izraz se tako že nahaja v prezentacijski obliki arabskih znakov. Vidimo pa, da je zadnja črka (od desne proti levi) desnega izraza napačna. Iz tega razloga lahko za rdečo kombinacijo črk zasnujemo naslednjo matriko pravila. Logika preverjanja deluje tako, da vzame hexadecimalno vrednost trenutne črke, in pregleda naslednjo črko. Če v pravilu trenutne črke najde še hexadecimalno vrednost naslednje črke, potem aktivira pravilo, ki vrne rezultat pravilne naslednje črke. Na enak princip deluje tudi iskanje in aktivacija drugih pravil, za druge kombinacije črk.

Poenostavljeno enostopenjsko pravilo za kombinacijo črk: فـخ

Trenutna črka	Naslednja črka	Rezultat pravila	Izraz po upoštevanju pravila
فـ	خ	خ	افخ

V naslednjem koraku si oglejmo primer kompleksnejšega pravila z več internimi stanji. Prejšnje pravilo je tako imenovano enkratno pravilo, saj vsebuje samo eno obliko naslednje črke.

Razširjeno sedem-stopenjsko pravilo za kombinacijo črk:
ا in vseh iz družine ع in družine غ

Trenutna črka	Naslednja črka (p1)	Naslednja črka (p2)	Naslednja črka (p3)
FE8D (ا)	FEC9 (ـعـ)	FECA (ـعـ)	FECB (ـغـ)
	Naslednja črka (p4)	**Naslednja črka (p5)**	**Naslednja črka (p6)**
	FECC (ـغـ)	FECD (ـغ)	FECE (ـغ)
	Naslednja črka (p7)	**Rezultat pravila družine** FEC9 (ـعـ)	**Rezultat pravila Družine** FECD (ـغ)
	FECF (غ)	FEC9 (ـعـ)	FECD (ـغ)

Podobna pravila ustvarimo za vse ostale kombinacije in družine črk. Princip prepoznave in aktivacije pravila je identičen tistemu, ki smo ga spoznali pri poenostavljenem enostopenjskem pravilu. Stopnja je odvisna od števila podpravil (p1), (p2), (p3),..., (p_n) za posamezno družino črke, ki se nahaja za trenutno. Družina podpravil npr. za črko *FECA* (ـعـ) je: FEC9 (ـعـ), FECB (ـغـ) in FECC (ـغـ). Ne glede na to, katera črka iz te družine se bo pojavila za črko FE8D (ا), vedno bo pravilo vrnilo rezultat FEC9 (ـعـ). Enako velja za

črke iz druge družine, ki so zajete v zgornjem sedem-stopenjskem pravilu.

Aplikacija, ki smo jo zasnovali v programskem jeziku C#, je zasnovana modularno in fleksibilno, saj omogoča dodajanje novih pravil po potrebi. Dodajanje pravil je izvedeno preko tako imenovane namestitvene (*ang. setup*) datoteke. Gledano dolgoročno se s tem izognemo nepotrebnim posegom v programsko kodo, ter hkrati uporabniku omogočimo ob vsakem trenutku kreacijo in dodajanje novih pravil. Namestitvena datoteka je običajna tekstovna datoteka z urejenimi tabelaričnimi zapisi pravil. To pomeni, da se mora uporabnik pri vnosu novih pravil držati samo tabelarične ureditve v datoteki. Ob zagonu okenske aplikacije za pretvorbo arabskih izrazov se pravila prenesejo iz namestitvene datoteke v interno dinamično strukturo programa, kjer jih le ta koristi po že opisanem postopku.

Iz tega vidika je razvita aplikacija na las podobna ekspertnemu sistemu, saj vsebuje večino ključnih gradnikov, kot so: uporabniški vmesnik, baza, pravila ipd. Da bi lahko aplikacijo uvrstili med ekspertne sisteme bi morali še vključiti mehanizme sklepanja, ki bi se navezovali na avtomatsko primerjavo orginalnih arabskih izrazov iz excel datoteke z izrazi, ki jih dobimo pri pretvorbi, katera upošteva samo pozicijo. V naslednji fazi bomo sistem nadgradili na stopnjo ekspertnega sistema, ki bo v navezi z mehanizmi sklepanja in avtomatske primerjave opravil avtomatsko generiranje pravil, katere smo v našem primeru definirali sami (empirično). V smislu obravnavanja pravil po principu *if* in *then*, kombinaciji le teh, ter aktivaciji, pa je delovanje razvitega *'translacijskega'* sistema povsem identično delovanju ekspertnih sistemov. Korelacijo med obema sistemoma je moč potrditi tudi pri načinu učenja preko dodajanja pravil.

5. Shematski prikaz postopka od pretvorbe do naložitve pretvorjenih zapisov v flash pomnilnik plačilnega terminala mPOS

Proces pretvorbe in posamezni koraki le tega, so prikazani na spodnji sliki. Ker smo proces pretvorbe že spoznali, si podrobneje oglejmo strukturo izhodne *'printout'* datoteke, ter nadaljnje postopke, kako vsebino *'printout'* datoteke prenesti v flash pomnilnik mPOS terminala.

'Printout' datoteka: Slednja služi kot vmesni člen med *Translacijskim orodjem* (1) in *Terminal Tool* orodjem (2). Omenjena datoteka predstavlja končni produkt pretvorbe, v njej pa se nahajajo tako angleški, kakor tudi arabski izrazi, ki so že v prezentacijski formi (FE70-FEFF). Vsaka kombinacija izrazov (angleški - arabski) se nahaja v svoji vrstici, pri čemer sta oba izraza medsebojno ločena z znakom tilda (~). Konec enega para je označen z znakom (¤). V naslednji vrstici je po enaki sintaksi zapisan drugi par itd. Označevanje in ločevanje zapisov z znakoma (~,¤) je pomembno zaradi kasnejšega poenostavljenega branja vsebine *'printout' hex* datoteke v *Terminalskem orodju*.

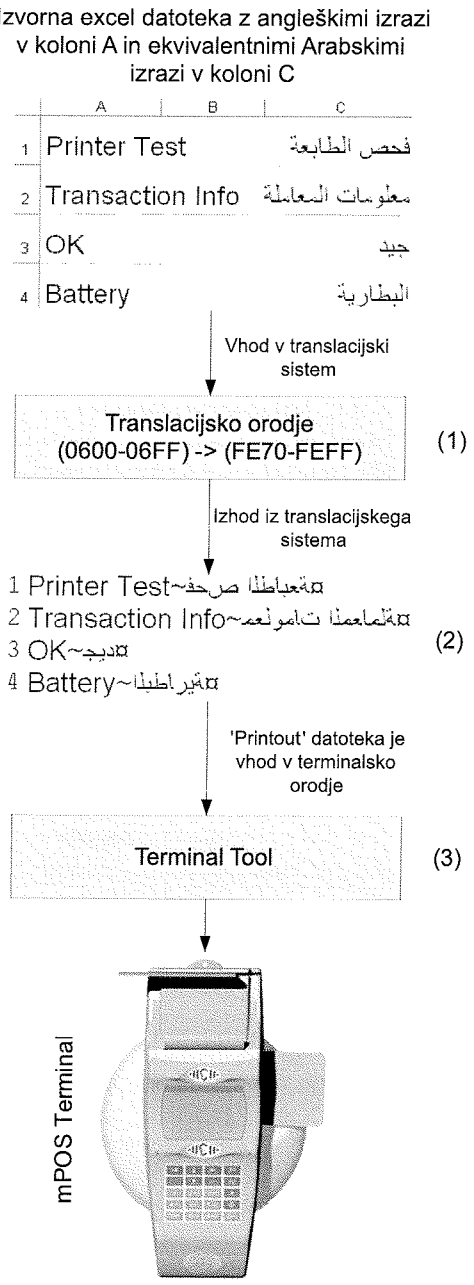

Slika 3: Procedura od pretvorbe do zapisa na flash pomnilnik mPOS terminala

Terminalsko orodje (Terminal Tool):

S pomočjo terminalskega orodja urejamo tako imenovane *M-Pay* konfiguracijske datoteke. Primarni namen orodja je nastavitev parametrov, ki se nato zapišejo v flash pomnilnik mPOS terminala. Dodajamo lahko tudi druge parametre, katerih vrednost lahko spremenimo preko uporabniškega vmesnika, brez posega na kodni nivo. Z enakim orodjem lahko naložimo tudi pripravljeno *'printout'* datoteko, ki predstavlja izhod in *translacijskega* orodja. Vse nastavljene in naložene vsebine v M-Pay konfiguracijski datoteki se nato preko Terminalskega orodja prenesejo in zapišejo na interni pomnilnik mPOS terminala. Terminalsko orodje se uporablja tudi za zapis konfiguracijskih parametrov na aPOS terminale (glej uvodno poglavje), vendar se v tem primeru

'printout' datoteka ne uporabi, saj aPOS terminal ne razpolaga z uporabniškim zaslonom, torej ne izpisuje in ne prikazuje nikakršnih vsebin. Če povzamemo funkcionalnosti terminalskega orodja; omogoča spreminajanje 'firmware-a', terminalskih nastavitev, logotipov, izpisov, fontov, zvočnih zapisov itd.

Inverzna pretvorba: Proces pretvorbe, ki smo ga spoznali v predhodnih poglavjih smo razširili tudi na pretvorbo v obratni (inverzni) smeri.

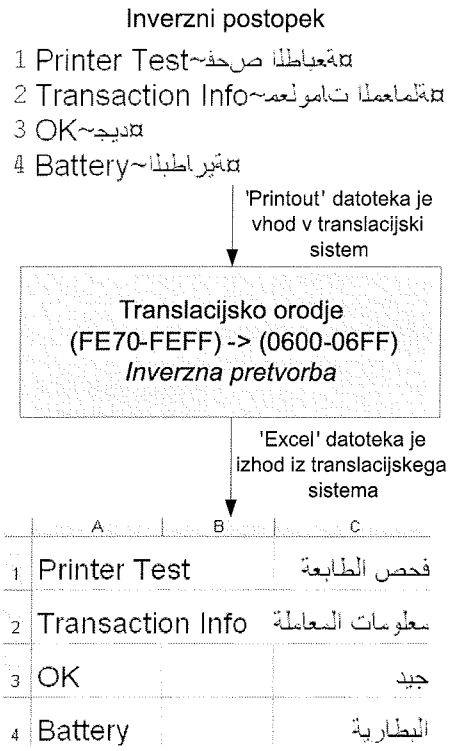

Slika 4: Inverzna pretvorba

Inverzno pretvorbo smo uvedli iz dveh razlogov: v kolikor poptrebujemo kakršne koli spremembe arabskih izrazov s strani prevajalca, je najenostavnejša rešitev izvoz v novo excel datoteko, ki jo lahko prevajalec enostavno spreminja. Na osnovi spremenjene datoteke lahko s translacijskim orodjem ponovno ustvarimo novo *'printout'* datoteko. Inverzna pretvorba, je enostavnejša v primerjavi z normalno pretvorbo, zaradi samo ene oblike arabskih črk v kodnem zapisu 0600-06FF. Naj spomnimo, da pri inverznem poteku pretvarjamo arabske črke iz kodnega sistema FE70-FEFF v kodni sistem 0600-06FF. Pretvorba poteka na sledeč način. Vsako arabsko besedo v prezentacijski formi (FE70-FEFF) razdelimo na posamezne črke, le te pa pretvorimo v *hexadecimalni* zapis. V naslednjem koraku za vsako črko besede s pomočjo preproste programske logike preiščemo translacijsko matriko. Ko algoritem najde ekvivalentno hexadecimalno vrednost črke besede kodnega sistema FE70-FEFF v translacijski matriki (Tabela 5), poišče istoležno originalno hexadecimalno vrednost (zapisano v hexadecimalni obliki sistema 0600-06FF), ki jo nato pretvori nazaj v črko iz kodnega sistema 0600-06FF. Črke posamičnih besed algoritem sestavi, in zapiše na ustrezno mesto ustrezne kolone excel datoteke. Enako storimo za vse ostale črke besed.

Drugi razlog, zakaj inverzna pretvorba, pa se nanaša na morebitno izgubo oziroma poškodovanje izvorne *.xls* datoteke s prevodi. Ker se le ti nahajajo v flashu terminala, jih lahko najprej s pomočjo *terminalskega orodja* izvozimo v *'printout' .hex* datoteko, nato pa s pomočjo *translacijskega* orodja v izvorno *.xls* datoteko.

6. Uporabniški vmesnik in funkcionalnosti

Uporabniški vmesnik temelji na dveh temeljnih korakih, ki hkrati poenostavljata uporabo razvite rešitve. Uporabniški korak tvorita ukaz *naloži*, s katerim uporabnik naloži izvorno datoteko *(.xls, .hex)* in ukaz *pretvori* s katerim sistem pretvori arabske zapise iz enega kodnega sistema v drugega. Z minimalnim številom korakov smo izpolnili pogoj uporabniške prijaznosti, z upoštevanjem minimalističnega oblikovanja pa poskrbeli za pregleden uporabniški vmesnik. Prebrane in pretvorjene izraze ispisujemo v dve ločeni tekstovni listi, predvsem iz razloga preverjanja ustreznosti

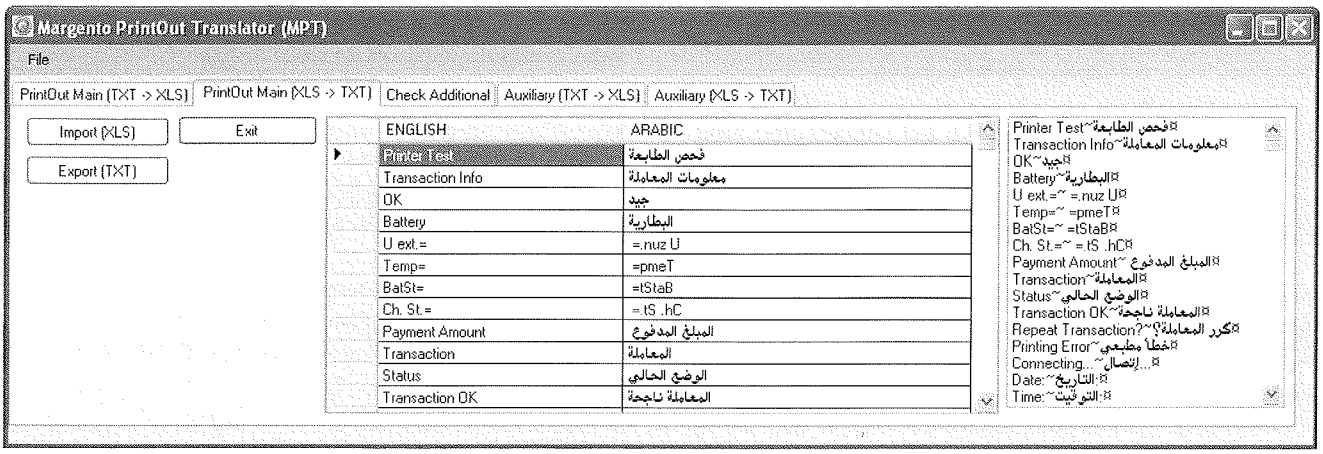

Slika 5: Uporabniški vmesnik in osnovne funkcije razvite rešitve

0,Unauthorized Terminal.|Please Call Mobily Support.	0، الجهاز غير مرخص|الرجاء الاتصال بخدمة العملاء
0,Transaction Denied.|Please Call Mobily Support.	0، المعاملة مرفوضة|الرجاء الاتصال بخدمة العملاء
0,Transaction Type Denied.|Please Call Mobily Support.	0، نوع المعاملة مرفوض|الرجاء الاتصال بخدمة العملاء
0,Transaction Delivery Denied.|Please Call Mobily Support.	0، تسليم المعاملة مرفوض|الرجاء الاتصال بخدمة العملاء
1,Transaction Delivery Failed.|Please Repeat.	1، فشل في تسليم المعاملة|الرجاء اعد المحاولة
0,Transaction Authorization|Denied. Please Call|Mobily Support.	0، ترخيص المعاملة|مرفوض. الرجاء الاتصال|بخدمة العملاء
1,Transaction Authorization|Failed. Please Repeat.	1، ترخيص المعاملة|مرفوض. الرجاء الاتصال|بخدمة العملاء
1,M-Pay System Is Currently|Unavailable. Please Repeat.	1، نظام M-Pay غير متوفر|حاليا. الرجاء اعد المحاولة

Slika 6: Originalen zapis (0600-06FF) v Auxiliary.xls datoteki

pretvorbe. Funkcij in gumbov, ki jih uporabnik v določenem trenutku ne potrebuje ne prikazujemo. V primeru pretvorbe *.xls* datoteke v *.hex* datoteko se izvrši normalna pretvorba, torej iz kodnega sistema 0600-06FF v kodni zapis arabskih prezentacijskih fontov FE70-FEFF. V primeru inverzne pretvorbe pa sistem pretvori *.hex 'printout'* datoteko in njeno arabsko vsebino iz kodnega sistema FE70-FEFF v kodni sistem 0600-06FF, in arabsko vsebino zapiše v novo *.xls* datoteko. Na ta način zagotovimo podporo pretvorbe v obe smeri. Zraven pretvorbe t.i. *'printout'* datoteke smo vključili še funkcionalnost pretvorbe t.i. *'auxiliary'* datoteke, kjer so zapisani razni dodatni napotki in errorji, ki jih terminal prikazuje ob različnih dogodkih. Struktura zpisa v *'auxiliary' .hex* in *.xls* datoteki je povsem identična strukturi zapisa v *'printout' .hex* in *.xls* datoteki. Iz tega razloga je enaka logika uporabljena tako za normalno kot inverzno pretvorbo *auxiliary* datoteke.

V razvito programsko rešitev smo dodatno implementirali še rešitev dopolnjevanja *dodatne* (ang. *additional*) *.hex* datoteke. *Additional.hex* datoteka privzeto vsebuje vse alfanumerične znake (evropsko tržišče). V primeru implementacije drugih jezikov, kot je npr. Arabski, pa implementirana logika za vsak znak vsake besede preveri, ali ga že ima zapisanega v t.i. *additional.hex* datoteki. Če le tega ne vsebuje, ga avtomatično doda. Postopek ponavlja vse do zadnje črke zadnje besede, ki je zapisana v *.xls* datoteki. Na ta način napolnimo *additional* datoteko z vsemi znaki, ki so zastopani v *.xls* datoteki, vendar en znak lahko v *additional* datoteki nastopa samo enkrat. Pri proceduri zapisa v flash pomnilnik mPOS terminala, terminalsko orodje preverja vsako črko besede z črkami, ki so enkratno zastopane v *additional* datoteki. Če slednjega v datoteki ne bi našel, ga tudi terminal na zaslonu ne bi prikazal (znak bi enostavno izpustil). Iz tega razloga je še toliko pomemneje, da avtomatiziran postopek napolni vsebino *additional* datoteke z novimi znaki, ki jih do tedaj še ne vsebuje. Da bi bila uporaba razvite rešitve še toliko lažja, smo vsakemu gumbu, funkciji, listi ipd. dodali namige (ang. tool tips), s katerimi ob enem uporabnika usmerja, in seznanja čemu je določen gumb, meni ipd. namenjen. Pri načrtovanju uporabniškega vmesnika smo prav tako upoštevali *Millerjev zakon* kratkotrajnega spomina, ter priporočene smernice.

7. Rezultati

Primer pretvorbe izrazov iz Auxiliary.xls datoteke v prezentacijsko obliko ter zapis v Auxiliary.hex datoteko:

Na sliki 6, je prikazan izsek zapisa *Auxiliary.xls* datoteke. Na skrajni desni se nahajajo izrazi zapisani v arabskem jeziku kodnega sistema 0600-06FF. Na sliki 7 je prikazan izsek izpisov (kodni sistem FE70-FEFF) iz ustvarjene *Auxiliary.hex* datoteke, ki predstavlja enega izmed izhodov translacijskega orodja.

```
1 0,Unauthorized Terminal.
2 Please Call Mobily Support.~0,الجهاز غير مرخص
3 ¤الرجاء الاتصال بخدمة العملاء
4 0,Transaction Denied.
5 Please Call Mobily Support.~0,المعاملة مرفوضة
6 ¤الرجاء الاتصال بخدمة العملاء
7 0,Transaction Type Denied.
8 Please Call Mobily Support.~0,نوع المعاملة مرفوض
9 ¤الرجاء الاتصال بخدمة العملاء
```

Slika 7: Pretvorjen arabski zapis v kodni sistem FE70-FEFF

Potrditev, da se pretvorjen zapis nahaja v kodnem sistemu FE70-FEFF prikazuje slika 8.

```
          0  1  2  3  4  5  6  7  8  9  a  b  ç  d  e  f
00000000h: FF FE 30 00 2C 00 55 00 6E 00 61 00 75 00 74 00 ; ÿþ0.,.U.n.a.u.t.
00000010h: 68 00 6F 00 72 00 69 00 7A 00 65 00 64 00 20 00 ; h.o.r.i.z.e.d. .
00000020h: 54 00 65 00 72 00 6D 00 69 00 6E 00 61 00 6C 00 ; T.e.r.m.i.n.a.l.
00000030h: 2E 00 0D 00 0A 00 50 00 6C 00 65 00 61 00 73 00 ; ......P.l.e.a.s.
00000040h: 65 00 20 00 43 00 61 00 6C 00 6C 00 20 00 4D 00 ; e. .C.a.l.l. .M.
00000050h: 6F 00 62 00 69 00 6C 00 79 00 20 00 53 00 75 00 ; o.b.i.l.y. .S.u.
00000060h: 70 00 70 00 6F 00 72 00 74 00 2E 00 7E 00 30 00 ; p.p.o.r.t...~.0.
00000070h: 2C 00 BA FE A8 FE AE FE E3 FE 20 00 AE FE F4 FE ; ,.°þ þ©þãþ .©þôþ
00000080h: CF FE 20 00 B0 FE 8E FE EC FE A0 FE E0 FE 8D FE ; Ïþ .°þŽþìþ þàþ¶þ
00000090h: 0D 00 0A 00 80 FE FC FE E4 FE CC FE E0 FE 8D FE ; ....€þüþäþÌþàþ¶þ
000000a0h: 20 00 94 FE E4 FE AA FE A8 FE 91 FE 20 00 DE FE ;  .”þäþªþ þ‘þ .Þþ
000000b0h: 8E FE BC FE 98 FE FB FE 8D FE 20 00 80 FE 8E FE ; Žþ¼þ˜þûþ¶þ .€þŽþ
000000c0h: A0 FE AE FE E0 FE 8D FE A4 00 0D 00 0A 00 30 00 ;  þ©þàþ¶þ¤.....0.
```

Slika 8: Hexadecimalni zapis vsebine v kodnem sistemu FE70-FEFF

Pretvorjeni izpisi v kodni sistem FE70-FEFF, ki jih nato zapišemo v flash pomnilnik mPOS terminala in prikažemo v menijih na zaslonu terminala so desno poravnani. Branje tovrstnih arabskih izpisov v menijih prav tako poteka od desne proti levi strani (zakonitosti pretvorbe iz enega v drug kodni sistem in obratno se ohranjajo).

Primer arabskih izpisov na zaslonu mPOS terminala je prikazan na sliki 9.

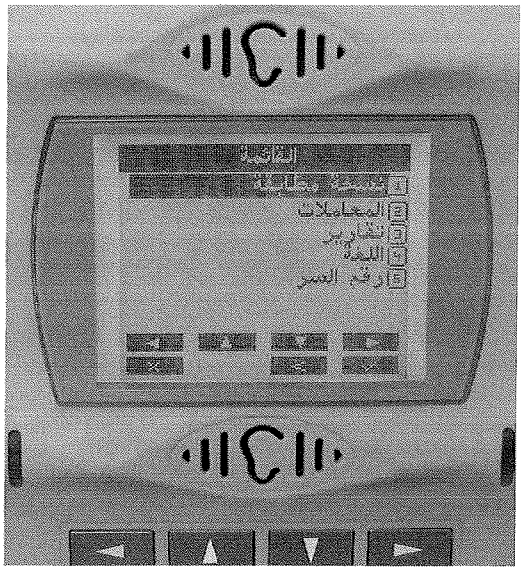

Slika 9: Izpis arabskih znakov kodnega sistema FE70-FEFF na zaslonu mPOS terminala

8. Sklep

Tekom članka smo predstavili princip in implementirane rešitve, ki pripomorejo k pravilni pretvorbi arabskih znakov iz kodnega sistema 0600-06FF v kodni sistem FE70-FEFF. Pristop z uporabo translacijskih matrik in aktivacijskih pravil se je v našem primeru izkazal za pravilnega. Ker so translacijske matrike zapisane v tako imenovani namestitveni datoteki, lahko uporabnik poljubno dodaja nove kombinacije. Enak pristop velja za pravila. To pomeni, da je sistem možno dograjevati in izpopolnjevati s strani drugih uporabnikov, saj je le ta javno dostopen vsakomur. Uspešna pretvorba je bila prav tako potrjena s strani naročnika iz Združenih Arabskih Emiratov. Rezultati, ki smo jih prejeli zadovoljujejo tako naše, kakor tudi naročnikove potrebe.

Literatura

/1/ http://unicode.org/charts/PDF/U0600.pdf

/2/ Zina Saadi, Arabic, Farsi and Urdu Text Normalization for Natural Language Processing, http://www.basistech.com/knowledge-center/Arabic/arabic-text-normalization.pdf

/3/ Kari Laitinen, A Natural Introduction to Computer Programming with C#

/4/ Sarmad Hussain, Nadir Durrani, Sana Gul, Survey of Language Computing in Asia 2005, http://www.panl10n.net/english/outputs/Survey/Arabic.pdf

/5/ http://www.unicode.org/charts/PDF/Unicode-3.2/U32-FE70.pdf

/6/ http://www.uconv.com/translit.htm

/7/ http://en.wikipedia.org/wiki/Glyph

Saša Klampfer, Peter Šamperl,
Zdenko Mezgec, Amor Chowdhury

Margento R&D d.o.o.
Gosposvetska cesta 84, Maribor, 2000, Slovenija
Epošta: sasa.klampfer@margento.com

Prispelo (Arrived): 21.09.2009 *Sprejeto (Accepted): 09.03.2010*

NAPAJALNI SISTEM BATERIJSKO PODPRTE RFID ZNAČKE

[1]Kosta Kovačič, [2]Anton Pleteršek

[1]IDS d.o.o. Ljubljana, Slovenia
[2]University of Ljubljana, Ljubljana, Slovenia

Kjučne besede: RFID, brezkontaktna identifikacija, sledenje, beleženje parametrov, baterijsko podprt sistem RFID, pametna aktivna značka.

Izvleček: V članku predstavljamo izvedbo napajalnega sistema, ki je uporabljen v baterijsko podprti RFID znački. Baterijsko podprte RFID značke uporabljajo enak princip prenosa podatkov do izpraševalnika kot pasivne RFID značke. Baterija je uporabljena za napajanje sestavnih blokov, kateri morajo delovati tudi izven elektromagnetnega polja. Predstavljena je nova rešitev izvedbe preklopnega vezja z aktivnim krmiljenjem tokovnih stikal. Rešitev omogoča napajanje celotnega integriranega vezja iz elektromagnetnega polja ali iz baterije, kjer se odločitev o viru napajanja izvede ob vsakem prekinitvenem dogodku. Sistem omogoča delovanje RFID značke v popolnoma pasivnem načinu, torej brez baterije ali v baterijsko podprtem načinu. V baterijsko podprtem načinu sistem omogoča delovanje značke tudi po izpraznitvi baterije.

Supply system in a battery supported RFID tag

Key words: RFID, data logger, passive RFID, battery-assisted RFID, Smart Active Label.

Abstract: In this article a supply system for a battery assisted RFID tag is presented. Battery assisted tags have a double supply - the electromagnetic field that is generated by the interrogator and a battery. The energy of the electromagnetic field is used to supply the parts of the system that need to work only in the presence of an interrogator while the battery energy is used to supply other parts of the system that need to work also in the absence of an interrogator. The system used in this work is an RFID battery assisted tag with an integrated temperature sensor and data logging capability. The integrated circuit has been designed in standard CMOS 0.35μm technology. The article presents a new supply source switch with active switch control based on the current level of the battery voltage. The complete integrated circuit can be supplied from this supply source switch where the decision on the supply source is made on each interrupt event that wakes up the circuit. The system has 3 interrupt sources, where the firs source is the RF supply, the second is the SPI interface and the third is the timer event for data logging. During sleep mode all blocks are turned off and the overall current consumption is less than 100nA. The new supply system is shown on the block diagram (figure 4) and on the schematic (figure 5). The figure 6 shows the simulation in case the battery voltage falls below the specified threshold and the rectified RF voltage is selected. The case where the battery voltage is above the threshold is shown in figure 7.

1 Uvod

RFID tehnologija je zelo razširjena v področju avtomatične identifikacije raznih izdelkov, v nadzoru dostopa, v plačilnih sistemih in v področju identifikacije živali. Že dalj časa se pojavlja težnja dodatne funkcionalnosti RFID sistemov, predvsem na področju merjenja fizikalnih parametrov. Vzrok za to težnjo je predvsem velika razširjenost teh sistemov pri skladiščenju in transportu. Med skladiščenjem in transportom izdelkov se lahko zgodi marsikaj, ki lahko vpliva na kvaliteto izdelka. Pomemben parameter, ki vpliva na lastnost raznih izdelkov, je temperatura, saj je hitrost kemičnih reakcij predvsem odvisna od temperature. Shranjevanje temperature med skladiščenjem in transportom je zelo pomembno pri izdelkih, ki ne spremenijo optičnih lastnosti z degradacijo in ni možno neposredno preveriti, ali jim je življenjska doba že iztekla. Pri takšnih izdelkih je ključnega pomena, da lahko življenjsko dobo avtomatično določimo glede na neprestano spreminjanje fizikalnih pogojev ob skladiščenju in transportu.

V članku je predstavljen napajalni sistem za RFID značko z integriranim temperaturnim senzorjem in enoto za avtomatično beleženje podatkov. RFID značka deluje v ISO15693 standardu, kjer je nosilna frekvenca 13,56MHz.

Nizka poraba integriranega vezja je ključna zahteva pri izdelavi majhnega in cenenega končnega izdelka. Prednost imajo predvsem avtomatsko nastavljivi napajalni sistemi /8/. Pri tem je pomemben način vklapljanja napajanja, ki je delno opisan v /9/. Končni izdelek je običajno v obliki kreditne kartice, kjer je uporabljena tankoplastna tiskana baterija. Glavna pomanjkljivost teh baterij je nizka kapaciteta, saj se le-ta giblje med 10mAh in 30mAh, pri površini 25cm^2. Druga pomanjkljivost je relativno visoka notranja upornost, ki je tudi odvisna od bremenskega toka. Upornost pri 1mA izhodnega toka je približno 200Ω. Vendar pa te slabosti odtehta zelo majhna debelina, upogljivost baterij in seveda nizka cena. Debelina baterije znaša manj od 1mm, baterije pa lahko prepogibamo brez poslabšanja lastnosti.

V drugem poglavju je predstavljeno napajanje običajnih pasivnih RFID značk in napajanje baterijsko podprtih RFID značk. V tretjem poglavju je predstavljen nov napajalni sistem, ki uporablja aktivno krmiljenje stikal za preklapljanje vira napajanja.

2 Napajanje RFID značk

2.1 Pasivne RFID značke

Pasivne RFID značke nimajo lastnega vira napajanja in se napajajo iz elektromagnetnega polja, katerega ustvarja izpraševalnik (interrogator). Energijo za delovanje pridobi

značka z usmerjanjem izmenične napetosti, ki se inducira na anteni. Antena je sestavljena iz tuljave, ki je zunanji element, in kondenzatorja, kateri je običajno integriran na samem vezju. Tuljava in kondenzator tvorita vzporedno resonančno vezje, ki ima resonančno frekvenco uglašeno na 13,56MHz, lahko pa tudi višje. Za značko je bolj primerna izbira vzporednega resonančnega vezja (Slika 1), ker le-ta nudi pri resonančni frekvenci visoko impedanco in posledično visoko inducirano napetost pri malem toku. Višja inducirana napetost je bolj primerna za usmernik izmenične napetosti, majhen tok pa pomeni, da bo integrirano vezje značke moralo imeti nizko porabo.

Poraba integriranega vezja predstavlja dušenje nihajnemu krogu, saj v njega teče tok, zato bi za izračun dušenja potrebovali ekvivalentno upornost, ki jo predstavlja poraba integriranega vezja, ki pa je žal zelo nelinearna.

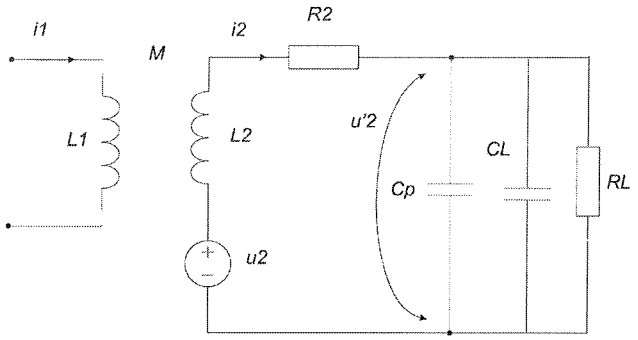

Slika 1: Ekvivalentno vezje magnetno sklopljene antene izpraševalnika in antene RFID značke

Za poenostavitev izberimo fiksno oddaljenost anten izpraševalnika in značke, kar nam omogoča, da tokovno breme integriranega vezja prevedemo v bremensko upornost (R_L), ki je dodana vzporedno k resonančnemu vezju (L_2 in C). Dobro uglašena resonančna frekvenca značke zelo vpliva na domet branja, zato je pomembno, da se le-ta natančno izračuna. Ko se značka približuje anteni izpraševalnika lahko inducirana napetost zelo naraste, zato imajo integrirana vezja RFID značk tudi omejevalnik napetosti, ki v bistvu znižuje kvaliteto nihajnega kroga in na ta način znižuje inducirano napetost. Kvaliteta se znižuje tako, da se dodatno vključujejo bremena, ki povišajo tok iz nihajnega kroga. V tem primeru bo tok, ki teče v integrirano vezje seveda dosti višji kot v neomejevanem delovanju, zato naša poenostavljena enačba ne bo veljala. Enačba bo veljala v področju od skrajnega dometa do točke, kjer se vključi omejevalnik napetosti.

Resonančna frekvenca antene RFID značke se izračuna po enačbi (1).

$$f_0 = \frac{1}{2\pi\sqrt{(L_2 \cdot C_2)}} \qquad (1)$$

Pri tem je $C_2 = C_p + C_L$.

Kadar se v tuljavi inducira napetost u_2 lahko napetost na sponkah integriranega vezja u'_2 določimo po enačbi (2).

$$u'_2 = \frac{u_2}{1 + (j\omega L_2 + R_2)\cdot\left(\frac{1}{R_L} + j\omega C_2\right)} \qquad (2)$$

Sedaj lahko zamenjamo inducirano napetost z $u_2 = j\omega M \cdot i1 = \omega k \sqrt{(L_1 \cdot L_2)}$ in dobimo odvisnost napetosti u'_2 od medsebojno induktivnostjo izpraševalnika in značke.

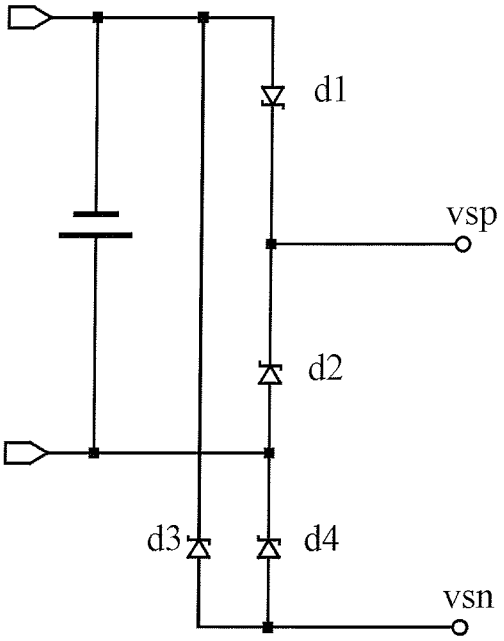

Slika 2: Polnovalni usmernik s Schotty diodami

$$u'_2 = \frac{j\omega M \cdot i_1}{1 + (j\omega L_2 + R_2)\cdot\left(\frac{1}{R_L} + j\omega C_2\right)} \qquad (3)$$

$$u'_2 = \frac{j\omega k \sqrt{(L_1 \cdot L_2)} \cdot i_1}{1 + (j\omega L_2 + R_2)\cdot\left(\frac{1}{R_L} + j\omega C_2\right)} \qquad (4)$$

Iz tega lahko izpeljemo realno obliko (5):

$$u'_2 = \frac{\omega k \sqrt{(L_1 \cdot L_2)} \cdot i_1}{\left(\frac{\omega L_2}{R_L} + \omega R_2 C_2\right)^2 + \left(1 - \omega^2 L_2 C_2 + \frac{R_2}{R_L}\right)^2}$$

V sistemih, ki delujejo na nosilni frekvenci 13,56MHz je kapacitivnost C_2 tako majhna, da je lahko v celoti sestavljena iz integriranega kondenzatorja, ki je priključen med antenske sponke integriranega vezja ter iz parazitnih kapacitivnosti.

Kvaliteta nihajnega kroga Q se določi po enačbi (6).

$$Q = \frac{1}{R_2 \cdot \sqrt{\left(\frac{C_2}{L_2}\right)} + \frac{1}{R_L} \cdot \sqrt{\left(\frac{L_2}{C_2}\right)}} = \frac{1}{\frac{R_2}{\omega L_2} + \frac{\omega L_2}{R_L}}$$

V 13,56MHz značkah je običajno uporabljen polnovalni usmernik, ki je tipično narejen iz tranzistorjev (slika 3). Lahko

je tudi narejen iz Schotty diod (slika 2) v primeru, če to omogoča uporabljena tehnologija.

2.2 Baterijsko podprte RFID značke

Poleg RF usmernika, ki je opisan v prejšnjem poglavju, imajo baterijsko podprte RFID značke še baterijsko napajanje.

V dosedanjih izvedbah pametnih aktivnih RFID značk smo zasledili določeno pomanjkljivost, in sicer je značka neuporabna po izpraznitvi baterije /5/. Takšno značko je potrebno zavreči, hkrati so pa izgubljeni tudi podatki, ki so trenutno shranjeni v trajnem spominu. V primeru, da se ugotovi izpraznjenost baterije dovolj zgodaj ni nobene škode, škoda lahko nastane, če se baterija nepričakovano izprazni v delovanju, ko je aktivno sledenje. To pomeni, da bo določena količina informacij, ki bi bila uporabna, izgubljena. Vzrok za omenjeno pomanjkljivost je dejstvo, da imajo ti sistemi deljeno napajanje. Nekateri deli vezja se napajajo iz enega vira (na primer iz baterije), drugi deli vezja pa iz drugega vira (na primer iz elektromagnetnih valov) /6/. To seveda pomeni, da deli vezja, ki se napajajo iz baterije, ne bodo več delovali po izpraznitvi baterije.

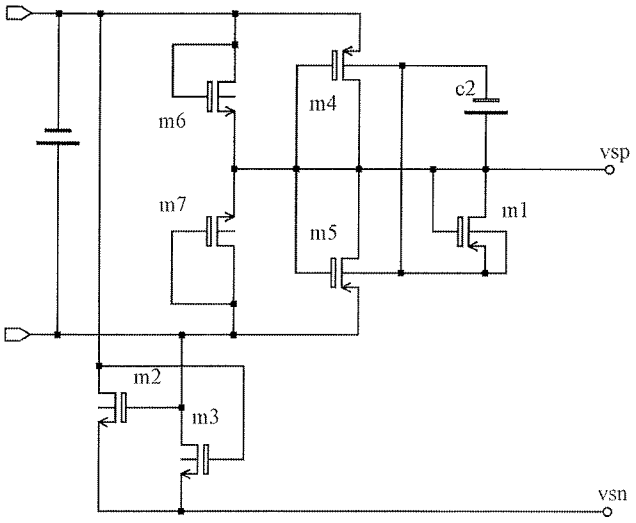

Slika 3: Polnovalni usmernik s tranzistorj

Problem delno rešuje /7/ z uporabo diod, bolj točno Schottky diod. Sistem za izbiro vira napajanja, ki ga opisuje omenjeni patent je pasiven sistem, kar pomeni, da bo za vir napajanja izbrana vedno najvišja napetost, ne glede na stanje baterije. V primeru pametne aktivne značke je bolj primerno, da se za napajanje uporabi baterija, kadar je napetost še dovolj visoka. Baterijsko napajanje je namreč bolj stabilno od RF napajanja, ki je odvisno od več različnih dejavnikov. Prav tako je slabost omenjenega sistema padec napetosti, ki je vedno prisoten na prevodno polarizirani diodi, in je glede na tip diode in uporabljeno tehnologijo od 0.2V do 0.7V. To pa pomeni, da bo napajalna napetost vezja za ta padec manjša, kot bi lahko bila ob uporabi aktivnega sistema izbire napajanja, kakršnega ponuja naša rešitev. Aktiven sistem napajanja omogoča delovanje integriranega vezja z 1.5V baterijo.

3 Izvedba preklopnega vezja

Integrirano vezje je načrtovano v 0,35 µm tehnologiji CMOS.

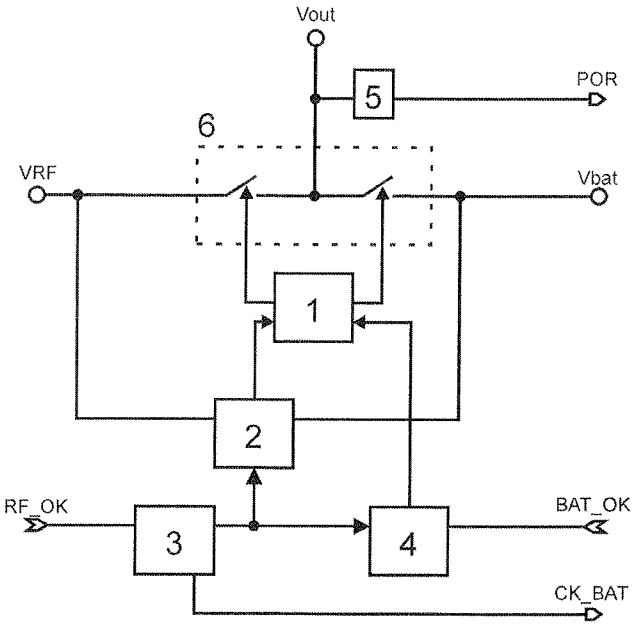

Slika 4: Blokovna shema preklopnega vezja

Blokovna shema enote za izbiro napajanja prikazuje slika 4. Stikala, ki na izhodno napajanje povežejo baterijsko napajanje (*Ubat*) ali usmerjeno RF napajanje (*URF*) sto označena s 6. V naši izvedbi sta to PMOS stikali. Podvezje 1 je kontrolno vezje za PMOS stikala, podvezje 2 je primerjalno vezje napajalnih napetosti *Ubat* in *URF*, ki izbere najvišjo napetost v vezju. Tej napetosti pravimo *Umax* in je povezana na 1, saj jo potrebujemo za ustrezno krmiljenje PMOS stikal. Podvezje 3 je zakasnilno vezje, ki zakasni signal RF_OK. Signal RF_OK je izhod podvezja za oceno usmerjenega RF napajanja, ki se nahaja v analognem radijskem delu in primerja usmerjeno RF napajanje z določenim pragom. Signal RF_OK je v visokem logičnem stanju, kadar je usmerjeno RF napajanje dovolj visoko, da zagotavlja zanesljivo delovanje preostalega vezja. Zakasnjen signal RF_OK je povezan na 2 in 4, nezakasnjen signal za vklop podvezja za oceno baterijske napetosti (CK_BAT), pa je povezan na vezje za primerjavo baterijske napetosti (ni na blokovni shemi). Podvezje za preverjanje baterijske napetosti se nahaja v analognem merilnem delu in ima na svojem izhodu 1 (signal BAT_OK), kadar je baterijska napetost dovolj visoka za zanesljivo delovanje preostalega vezja. Podvezje 4 po zakasnitvi da podvezju 1 signal, ali je baterijska napetost dovolj visoka za zanesljivo delovanje. Podvezje 5 je vezje, ki generira dinamični reset signal (POR) samo ob vklopu baterijskega napajanja, oz. tudi ob vklopu RF napajanja, če baterijskega napajanja ni. Namen tega signala je povrnitev vseh spominskih celic (flip flop) v začetno stanje.

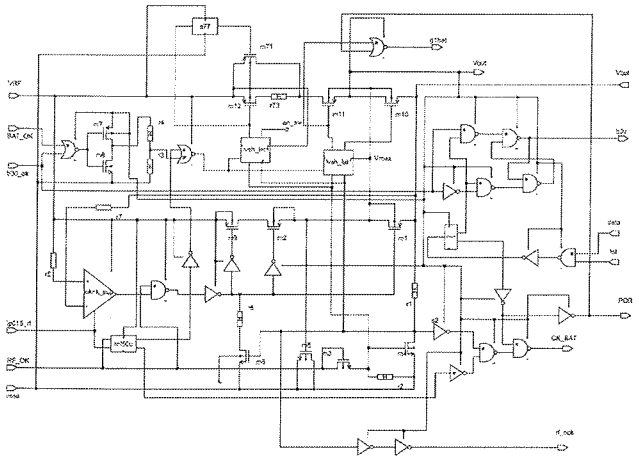

Slika 5: Shema preklopnega vezja za izbiro napajanja

3.1 Analiza vezja

Običajen potek izbire napajanja (slika 7) se začne ob priključitvi baterije, katera sproži POR signal in resetira preostalo vezje. V delovanju lahko pride antena značke v elektromagnetno polje, RF napajanje postane aktivno in analogni radijski del generira signal RF_OK. Podvezje 3 takoj ob RF_OK signalu sproži signal CK_BAT, ki zažene vezje za primerjavo baterijske napetosti. V primeru, ko je baterijska napetost dovolj visoka za zanesljivo delovanje (1,2V) se signal BAT_OK postavi na 1 in ob preteku zakasnitve vezje izbere baterijsko napajanje. Za zanesljivo delovanje PMOS stikal skrbi podvezje 2 na sliki 4, ki najvišjo napetost v vezju pelje v kontrolno vezje PMOS stikal (podvezje 1 na sliki 4) in s pravilnim krmiljenjem izniči možnost povratnih tokov.

Slika 6 prikazuje simulacijo enote za izbiro napajanja, ko baterijska napetost pade pod najnižji dovoljen nivo. Ob trenutku 1 priključimo na vezje baterijsko napajanje z napetostjo 1,5V. Ob tem trenutku se sproži tudi POR signal, kateri vključi vezje za primerjavo baterijske napetosti s signalom CK_BAT. Vezje za primerjavo baterijske napetosti kontrolira signal BAT_OK, ki ima do trenutka 2 visok logični nivo, saj je baterijska napetost dovolj visoka. Ob trenutku 3 baterijska napetost pade pod najnižji dovoljen nivo, vendar se ob tem trenutku nič ne zgodi v samem vezju, saj vezje za primerjavo baterijske napetosti ni aktivno. Ob trenutku 4 (slika 6) pride značka v elektromagnetno polje in RF napajanje se dvigne nad najnižji nivo. V trenutku 5 se postavi signal RF_OK, ki pravi, da je RF napajanje dovolj visoko. Signal RF_OK sproži vezje za primerjavo baterijske napetosti s signalom CK_BAT, vendar je ob koncu primerjave baterijske napetosti (trenutek 6) signal BAT_OK na nizkem nivoju, kar pomeni, da je baterijska napetost prenizka. Zato se ob trenutku 7 za glavno napajanje Vout izbere RF napajanje. Napajanje Vmax, ki je zmeraj priključeno na najvišje napajanje v vezju, se na RF napajanje priključi že ob trenutku 5, ko postane aktiven signal RF_OK in tako zagotovi pravilno delovanje stikal.

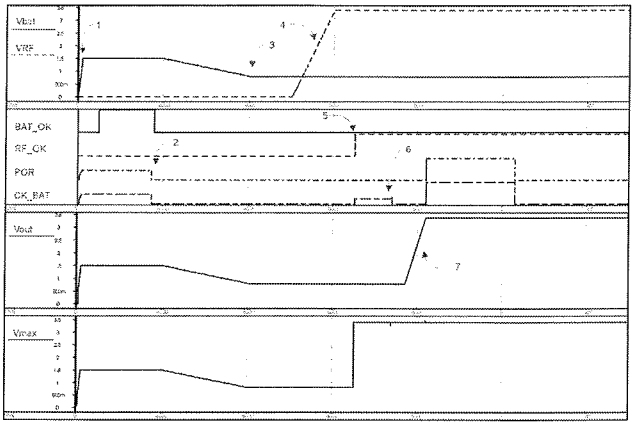

Slika 6: Potek izbire napajanja pri nezadostni baterijski napetosti

Slika 7 prikazuje simulacijo enote za izbiro napajanja za primer, ko je baterijska napetost dovolj visoka čez celoten potek grafa. Ob trenutku 1 priključimo na vezje baterijsko napajanje z napetostjo 1,5V. Ob tem trenutku se sproži tudi POR signal, kateri vključi vezje za primerjavo baterijske napetosti s signalom CK_BAT. Vezje za primerjavo baterijske napetosti kontrolira signal BAT_OK, ki je do trenutka 2 v visokem stanju, saj je baterijska napetost dovolj visoka. Ob trenutku 3 pride značka v elektromagnetno polje in RF napajanje se dvigne nad najnižji nivo. Ob trenutku 4 se postavi signal RF_OK, ki pove, da je RF napajanje dovolj visoko. Signal RF_OK sproži vezje za primerjavo baterijske napetosti s signalom CK_BAT. Po končani primerjavi baterijske napetosti (trenutek 5) je signal BAT_OK na visokem nivoju, zato se RF napajanje ne bo izbralo za glavno napajanje. Napajanje Vmax, ki je zmeraj priključeno na najvišje napajanje v vezju, se na RF napajanje priključi že ob trenutku 4, ko postane aktiven signal RF_OK in tako zagotovi pravilno delovanje stikal.

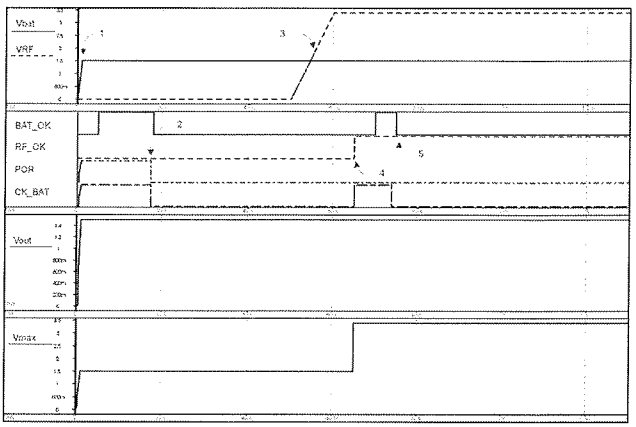

Slika 7: Potek izbire napajanja pri zadostni baterijski napetosti

Shema vezja za izbiro napajanja je na sliki 5, kjer so tudi signali, katere nismo opisali v delovanju samega vezja in v blokovnem diagramu. Signal b30_ok je na logični enici, kadar vhodna napetost presega 2,4V, torej kadar je prik-

ljučena baterija z nominalno napetostjo 3V. V tem primeru vezje za izbiro napajalne napetosti ne deluje nič drugače, kot kadar je priključena baterija z nominalno napetostjo 1,5V. Signal b30_ok se v vezju za izbiro napajanja le shrani, saj je potreben za izklop napetostnega dvojilnika. Shranjen signal se imenuje b3v in je na shemi prikazan kot izhod. Drugi izhodni signal je g1bat, ki je na logični enici, kadar na integrirano vezje ni priključena baterije in se vezje napaja iz RF polja. Ostali signali so testni signali in vhod za delovni tok.

4 Sklep

Integrirano vezje je načrtano v standardni tehnologiji CMOS 0.35µm. Omogoča brezkontaktno komunikacijo z RFID izpraševalnikom na standardu ISO15693. Integriran ima tudi temperaturni senzor in vezje za avtomatično beleženje temperature. Za shranjevanje podatkov je uporabljen pomnilnik tipa EEPROM.

Prednost predstavljenega integriranega vezja RFID nalepke pred prejšnjimi izvedbami /2/, /3/, /4/, /5/, /6/, /7/, je v vpeljavi aktivnega preklopnika izvora napajanja, ki je opisan v tem članku. Ob vsaki prekinitvi iz stanja pripravljenosti (wake-up) se sistem odloči o viru napajanja, glede na trenutno stanja baterije. V stanju pripravljenosti so vsi sklopi integriranega vezja izklopljeni. Poraba v stanju pripravljenosti je tako manjša od 100nA.

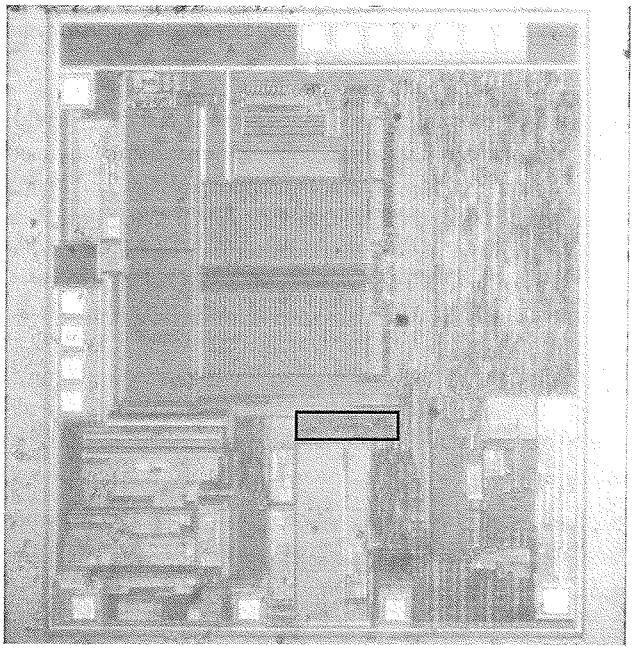

Slika 8: Slika integriranega vezjaRFID nalepke z označenim preklopnikom izvora napajanja

Predstavljeno vezje se prav tako lahko napaja le iz elektromagnetnega polja in je lahko uporabljeno v popolnoma pasivnih značkah, kot RFID temperaturni senzor.

Prednost takšnega sistema se pokaže tudi v izvedbi z baterijo, saj lahko izpraševalnik dostopa do podatkov, ki so shranjeni na trajnem pomnilniku, tudi po izpraznitvi baterije.

Na sliki 6 je prikazano testno vezje RFID nalepke, kjer je označen tudi preklopnik napajanja.

Zahvale

Avtorja se zahvaljujeta zaposlenim podjetja IDS za nasvete in podporo.

Izvedbo raziskav na projektu je delno financirala Evropska unija.

Literatura

/1/ Dominique Parret: „RFID and Contactless smard card applications", John Wiley & Sons Ltd., 2005.

/2/ B. Abali, H. Franke, M. E. Giampapa: „Method and aparathus for automated measurement of properties of perishable consumer products", Patentna objava PCT WO 00/45331, 2000.

/3/ S. K. Howel, I. Butler: „Identification tag with environmental sensong faccility", Patentna objava GB 2308947 A, 1997.

/4/ P. Sorrels, S. Poulin, L. Furey, S. Alexander: "Radio identification tag device with sensor input", Patentna objava US 6720866 B1, 2004.

/5/ N. Batra: "RFID sensor tag with manual modes and functions", Patentna objava PCT WO 145911, 2007.

/6/ L. W. Kueckendahl: "Data capture and logging with passive data transmission", Patentna objava WO 01/84581 A1, 2001.

/7/ Heinrich Harley Kent, "RFID tag having combined battery and passive power source", Patentna objava US2003017804 A1, 2003.

/8/ ATANASIJEVIĆ-KUNC, Maja, KUNC, Vinko. Automatically adjustable supply system, Avtomatsko nastavljivi napajalni sistem. Inf. MIDEM, mar. 2007, letn. 37, št. 1, str. 12-15.

/9/ KUNC, Vinko, VODOPIVEC, Andrej. Vmesnik za zagotavljanje napajalne napetosti s funkcijo mehkega vklopa : patent št. 21527, podeljen z odločbo št. 600-154/03-JM-3 z dne 03. 1. 2005 : datum objave 31. 12. 2004 : številka prijave P-200300154, datum prijave 20. 6. 2003. Ljubljana: Urad RS za intelektualno lastnino, 2004.

/10/ Klaus Finkenzeller: „RFID Handbook", John Wiley & Sons Ltd., 2003

Kosta Kovačič
IDS d.o.o. Sojerjeva 63, 1000 Ljubljana, Slovenia
E-mail: kosta.kovacic@ids.si
Tel: +386 1 281 11 83

Anton Pleteršek
University of Ljubljana, Tržaška 25,
1000 Ljubljana, Slovenia
E-mail: anton@kalvarija.fe.uni-lj.si,
anton.pletersek@ids.si

Prispelo (Arrived): 20.11.2009 *Sprejeto (Accepted): 09.03.2010*

DIGITAL TEMPERATURE COMPENSATION OF CAPACITIVE PRESSURE SENSORS

Matej Možek, Danilo Vrtačnik, Drago Resnik, Borut Pečar, Slavko Amon

Laboratory of Microsensor Structures and Electronics (LMSE), Faculty of Electrical Engineering, University of Ljubljana, Ljubljana, Slovenia

Key words: ASK, RFID, Receiver, 13.56 MHZ, ISO/IEC 14443, CMOS.

Abstract: Implementation of a novel digital temperature compensation method, developed for piezoresistive pressure sensors, to the field of capacitive sensors is presented. Possibilities for the compensation of sensor parameters such as sensor nonlinearity and temperature sensitivity are analyzed. In order to achieve effective compensation and linearization, different approaches to digital descriptions of sensor characteristic are investigated and reported, such as two-dimensional rational polynomial description and Chisholm approximants. Evaluation results of sensor response are compared against reference pressure source and most effective digital temperature compensation is proposed.

Digitalna temperaturna kompenzacija kapacitivnih senzorjev tlaka

Kjučne besede: kompenzacija, Padéjev aproksimant, Chisholmov aproksimant, Taylorjeva vrsta, nelinearnost, občutljivost, kapacitivni senzor

Izvleček: V prispevku so predstavljene izboljšane metode za digitalno temperaturno kompenzacijo kapacitivnih senzorjev tlaka. Veliko izboljšav sledi iz področja piezorezistivnih senzorjev tlaka. Analizirane so možnosti kompenzacije senzorskih parametrov kot sta nelinearnost in temperaturna občutljivost. Za doseganje učinkovite temperaturne kompenzacije in linearizacije so predstavljeni različni pristopi k opisu senzorske karakteristike, kot npr. ulomljena polinomska aproksimacija in Chisholmovi aproksimanti. Rezultati ovrednotenja s posameznim opisom senzorske karakteristike so primerjani glede na tlak referenčnega tlačnega izvora. Iz rezultatov primerjave smo izbrali in predlagali najbolj ustrezno metodo temperaturne kompenzacije.

1 Introduction

Sensors that exhibit a change in electrical capacitance as a response to a change in physical stimulus represent an attractive approach for use in modern sensor systems due to their extensive range of applications such as humidity, pressure, position sensors etc. Their broader range of applications include biomedical, touch & non-touch switch technology, proximity sensing, fingerprinting, automotive applications, robotics, materials property, and applications in motion sensors. This versatile sensor category offers higher precision and robustness, simpler construction and lower power consumption than resistive-based alternatives. However, they traditionally require more complex interfacing circuits, which represented a major disadvantage in the past. In a capacitive sensor, the physical parameter being measured by varying one or more of the quantities in the basic equation of capacitance

$$C = \varepsilon \frac{A}{d} \qquad (1)$$

where ε is the permittivity of the dielectric, A is the overlap area of the capacitor plates, and d is the distance between the plates. For example, humidity sensors typically work by varying the permittivity ε, pressure sensors by varying distance d and position sensors by varying area A or distance d. Measurement of the sensor capacitance is generally achieved by applying an excitation source to the capacitor electrodes which is used to turn variance in capacitance into a variance in voltage, current, frequency or pulse width variation. Translation from voltage or current to a digital word requires an additional analog to digital converter (ADC).

The expected variance in capacitance is generally in the order of several pF or less. In many cases the stimulus capacitance change is much smaller than the parasitic capacitances present in the measuring circuit, hence representing a difficult interfacing task. However, a modification of conventional sigma"delta analog to digital converter architecture has been identified as a suitable basis for monolithic Capacitance to Digital Converter (CDC) /1/. Circuit itself is parasitic insensitive, and can be configured to work with both floating (access to both sensor terminals) and grounded configuration sensors (one terminal grounded).

Precision capacitive sensor interface products are based on a well established sigma-delta (ΣΔ) conversion technology. Converters utilizing ΣΔ principle offer excellent linearity and resolution and are appropriate for most sensor interfacing applications. A typical ΣΔ converter ADC consists of a switched-capacitor modulator followed by a digital filter. The modulator operation is based on balancing, over time, an unknown charge with a known reference charge of variable polarity /1, 2/.

Charge from reference terminal and input terminal are summed in an integrator. The integrator is inside a feedback loop, whose action is to control the polarity of the reference charge so that the integrator output averages to

zero. This occurs when the magnitude of the average reference charge is equal over time to the input charge, hence the name - charge balancing converter. The reference charge is derived by charging a known capacitor to a known (reference) voltage. The polarity of reference voltage is varied. In a conventional voltage input ΣΔ converter, the unknown charge is derived from charging a fixed capacitor to an unknown input voltage, while in the capacitance to digital converter (CDC) realization, the voltage is fixed and the capacitor is variable. Such arrangement provides the high precision and accuracy that are typical for ΣΔ ADCs /3,4/. Modern implementations enable measurement of capacitances in atto Farad (aF) range /4, 5/, with effective noise resolution of 21 bits and corresponding resolution down to 4 aF. They offer measurements of common-mode capacitance up to 17 pF on 4 pF range with 4 fF measurement accuracy. These implementations offer complete sensor solutions, however their application is limited to indication of temperature and humidity dependence problem /6/ of capacitive sensors, while not offering an effective implementation for compensation of these unwanted quantities. In the following work an effective method of temperature compensation of capacitive pressure sensors will be presented.

2 Setup and measurements

The layout of designed capacitive sensor measurement system is depicted in Figure 1. Capacitive sensor with the CDC AD7746 is shown leftmost. The sensor is connected via interface module to the I^2C - USB converter, which is used to interface the sensor to the host PC.

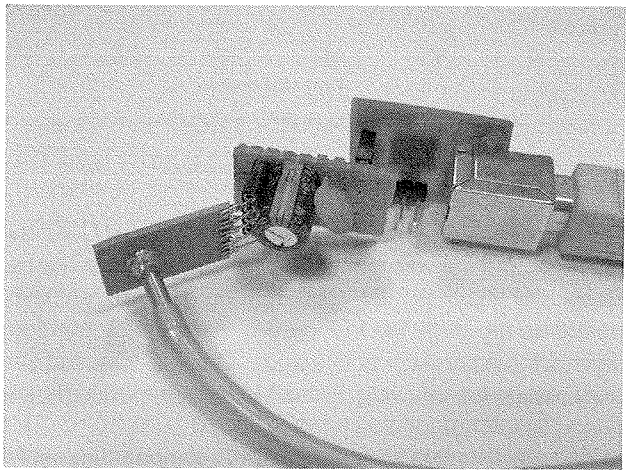

Fig. 1: General layout of the capacitive sensor evaluation module.

A dedicated electronic interface module was designed. This module enables data transmission and control of CDC AD7746. The module itself is based on a CY8C24794 Programmable System on Chip (PSoC) circuit. The layout of PSoC interconnection blocks is depicted in the Figure 2.

The hardware is used to directly map the CDC to the controlling PC. Designed PC software performs the functions of CDC status and data reading. In fact, the controlling software implements all functions of AD7746: from capacitance channel setup to the temperature sensor channel setup as well as channel excitation, common mode capacitance setting, offset and gain of capacitance measurement channel.

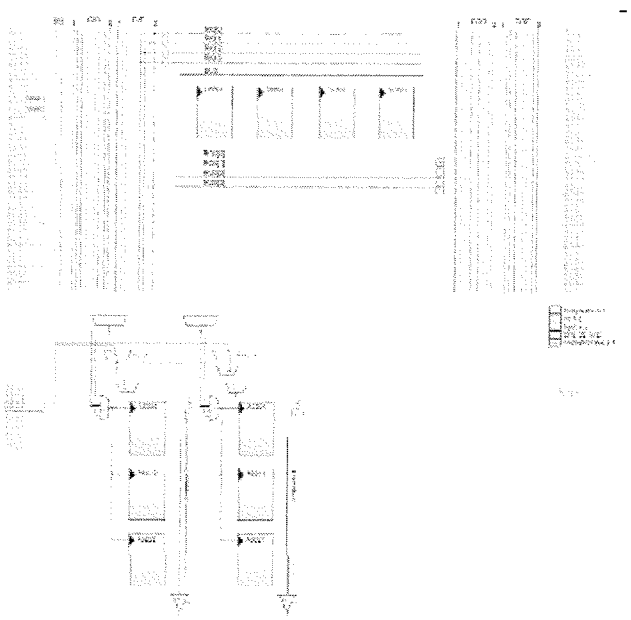

Fig. 2: PSoC device interconnections.

Measurement range optimization was performed in order to get maximal span of CDC measurement range. Measured device, the LTCC capacitive sensor /7/, exhibits negative slope of sensor characteristic. Therefore, the measurement range optimization must be performed at maximal pressure readout with minimal pressure applied and vice versa.

This indicates that the offset compensation must be performed before the gain compensation. Sensor offset response is compensated by setting AD7746 registers CAPDACA and CAPOFFSET. The register value CAPDACA value affects coarse setting of offset response and the CAPOFFSET affects fine setting of sensor response. The procedure of offset setting is comprised of coarse and fine offset setting. Because of negative sensor characteristic slope, the fine offset value is initially set at maximum and the coarse value is altered from its initial zero value in such manner, that the raw sensor readout maintains its maximal value. The setting of CAPDACA register is performed by successive approximation approach, starting at MSB of CAPDACA register. The subsequent bits are tested against raw sensor output. If the sensor output exceeds the maximal sensor readout ($FFFF_{16}$) when corresponding bit is set to 1, then the bit is set to zero and the algorithm advances towards lower bits. After the coarse register was set, the CAPOFFSET register is processed in a similar

manner. The result of this algorithm is a maximal sensor response value at applied offset pressure.

After successful optimization of offset value, the gain parameter is set in a similar manner. Minimal sensor response is set with alteration of CAPGAIN register, which actually changes the clock rate of front-end of CDC. The procedure starts with minimal setting of CAPGAIN register. The bits of CAPGAIN register are tested according to described successive approximation algorithm, just the bit-testing criteria is now minimal CDC readout. The result of this algorithm is minimal sensor response at maximal applied pressure. Initial measurements were performed at "Jožef Stefan Institute" /7/. The aim of these measurements was the determination of optimal settings of AD7746 and the tested LTCC sensor. Results of these measurements are depicted in Figure 3. Figure 3 shows the results of sensor characteristic in up and down scan of pressure range. Tested sensor exhibited practically no hysteresis, but the deviation form ideal straight line indicated the necessity for sensor characteristic linearization. The measurements were performed at a room temperature.

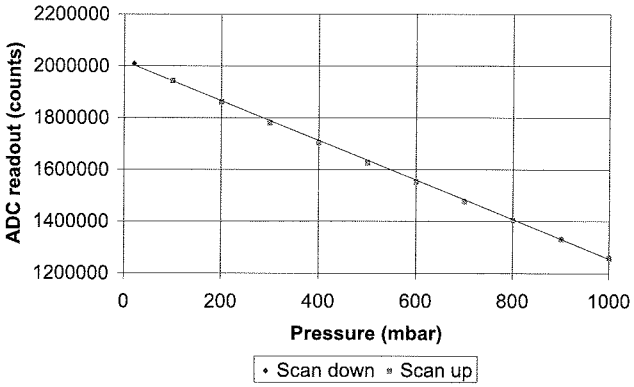

Fig. 3: Initial pressure sensor measurements.

Measurements were repeated in HYB d.o.o., Šentjernej. This time, the scan was performed at three different temperatures. Sensor with interface electronic circuit were placed in the temperature chamber and measurement of raw response value was performed at three different temperatures. As the aimed temperature range was set at 0 °C ... 70 °C, the temperature calibration points were selected at 0 °C, 35 °C and 70 °C. The measurements have demonstrated the susceptibility of initial electronic circuit design to electromagnetic interference. Initially it was believed that the long integration setting of AD7746 will solve the problem of 50 Hz hum. As the temperature measurements were performed at temperatures, below room temperature, the chamber compressor switching affected the sensor readout as depicted in Figure 4.

Figure 4 is showing raw CDC response versus number of samples. The sample rate was set at two samples per second. The left part of Figure 4 is showing disturbed CDC readout when temperature chamber compressor was switched. Pressure was increased from offset to full scale

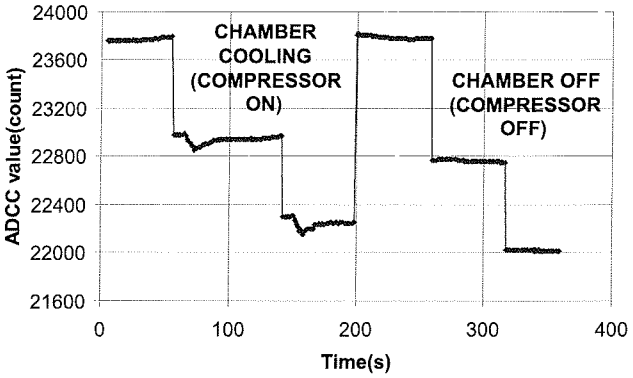

Fig. 4: Sensor readout at lower temperatures.

in three increments. The right part of Figure 4 is showing the CDC readout with compressor turned off and again with three pressure settings, ranging from offset to maximal pressure. As the temperature was elevated above room temperature, the CDC readout diminished, as the compressor is not needed for achievement of higher temperatures. Sensor was fitted with additional shielding (tin foil) and the shielding terminal was grounded in further measurements. Results of raw CDC response stability are shown in Figure 5 at three different temperatures at 0 °C, 35 °C and 70 °C.

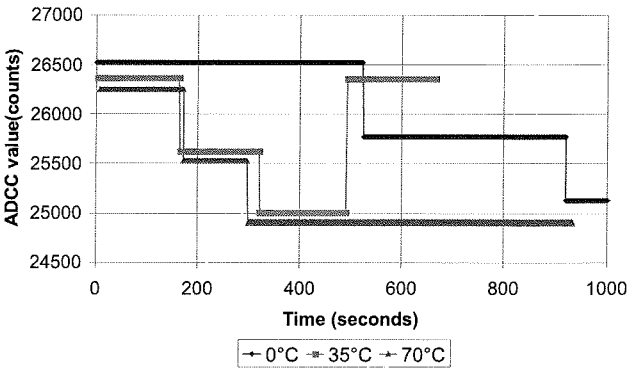

Fig. 5: CDC readout stability.

Sensor responses were evaluated and stabilized CDC raw response points were obtained at different temperatures. Results of stabilized raw CDC readouts at different temperatures are depicted in Figure 6. At each temperature setting, three pressure points were obtained. Acquired stability results are showing 12 % of sensor response degradation over temperature increase from 0 °C to 35 °C. This turned our attention to more elaborate temperature analysis of sensor properties.

Acquired sensor characteristics were redisplayed as a function of temperature. Resulting data is depicted in Figure 7. This enabled further sensor temperature properties assessment. Analysis from Figure 7 has shown, that tested sensor exhibits a typical pressure span of 1400 counts over 2000 mbar range, which yields approximately an average sensitivity of -0.7 counts/mbar. The temperature coefficient of offset was evaluated as a normalized sensor re-

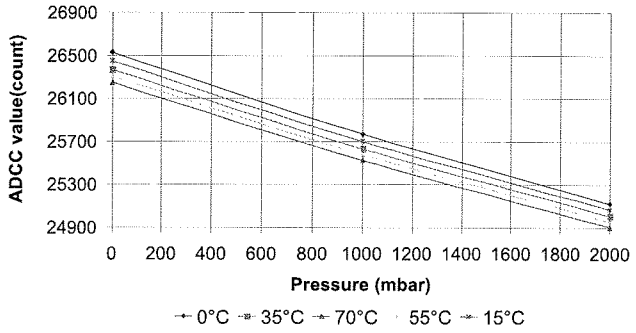

Fig. 6: Stabilized CDC readouts vs. pressure over entire temperature range.

sponse over observed temperature range. A large sensor offset temperature coefficient was found at 0.3% FS/°C, which results in total 21% change of sensor offset over temperature range. More encouraging was a low temperature coefficient of sensitivity value, which was estimated at 0.04% FS/°C.

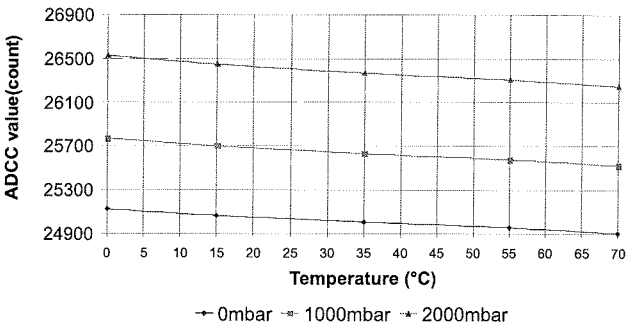

Fig. 7: Stabilized CDC readouts vs. temperature over entire pressure range.

A fairly consistent 3% change in sensitivity was found over temperature calibration range. This indicates the simplicity of sensitivity compensation. On the other hand, a large dependence of sensor offset requires a more complex offset compensation algorithm.

3 Temperature compensation

As the CDC produces a digital capacitance readout, we focused our work towards digital implementations of temperature compensations. The CDC features ΣΔ approach, the sample rate is limited to several tenths of samples (90 SPS maximum for AD7746), indicating that the increasing complexity of digital processing after acquisition of raw sensor data is not the limiting factor for the entire sensor signal processing.

Temperature compensation of capacitive sensor requires an accurate mathematical description of sensor characteristic in two directions. In case of investigated pressure sensor, the input axes comprise raw pressure and temperature readout and the result is the compensated pressure. Compensation complexity level is depending on sensor nonlinearity of temperature and pressure characteristic. Most adaptable and versatile digital description of sensor characteristic is achieved by Taylor expansion of sensor characteristic. Sensor characteristic expansion can be further segmetned into intervals by writing an expansion around interval ($p_{ocOFFSET}$, $T_{ocOFFSET}$).

$$\begin{aligned} \Delta p &= p_{oc} - p_{ocOFFSET} \\ \Delta T &= T_{oc} - T_{ocOFFSET} \end{aligned} \tag{2}$$

where the raw pressure readout p_{oc} and raw temperature readout T_{oc} are offset with corresponding values $p_{ocOFFSET}$ and $T_{ocOFFSET}$ respectively. Segmentation using (2) further reduces the calibration error.

Taylor series description (3) represents a general approach to sensor characteristic description using segmentation, recommended by IEEE1541.2 standard /8/.

$$p = \sum_{i=0}^{N_P}\sum_{j=0}^{N_T} A_{ij} \cdot \Delta p^i \cdot \Delta T^j \tag{3}$$

Where Δp represents an offset corrected raw readout from capacitive sensor, ΔT represents the offset corrected raw readout from temperature sensor residing on sensor signal conditioner and the N_P and N_T represent the order of Taylor series.

However, such representation requires $N_P \cdot N_T$ calibration points, which is unacceptable. Another major drawback is the use of floating - point calculation coefficients A_{ij} and involution operator. Although algorithms for fast evaluation of (3) were presented /9/, time consuming mathematical operations will reduce the output update rate. On the other hand, the Taylor expansion provides a reasonable start point for initial coefficient relevance. coefficients A_{ij} are obtained by solving a system of linear equations. However, this system is resolved by computing a Vandermonde matrix, which is generally ill conditioned.

In order accommodate abovementioned drawbacks, a two - dimensional Padé approximant, also named Chisholm approximant /10/, is evaluated. This evaluation inherently reduces the number of required calibration points by one.

$$\begin{aligned} A(p_{oc}, T_{oc}) &= \sum_{i=0}^{N_P}\sum_{j=0}^{N_T} a_{ij} \cdot \Delta p^i \cdot \Delta T^j \\ B(p_{oc}, T_{oc}) &= \sum_{i=0}^{N_P}\sum_{j=0}^{N_T} b_{ij} \cdot \Delta p^i \cdot \Delta T^j \\ p(p_{oc}, T_{oc}) &= \frac{A(p_{oc}, T_{oc})}{B(p_{oc}, T_{oc})} \quad \text{where} \quad b_{00} = 1 \end{aligned} \tag{4}$$

For effective temperature compensation of capacitive sensor signal conditioner a two-dimensional rational polynomial for pressure calculation is used /11/. This type of digital temperature compensation enables correction of nonlinearities up to second order.

$$p = \frac{A_0 + \Delta P + A_1 \cdot \Delta P^2 + A_2 \cdot \Delta T + A_3 \cdot \Delta T^2}{A_4 + A_5 \cdot \Delta T + A_6 \cdot \Delta T^2} \tag{5}$$

Where A_0 through A_6 are calibration coefficients of pressure sensor. Pressure sensor characteristic can be described with inverse proportion of A_4 to sensor sensitivity

and the ratio of A_0/A_4 in proportion to sensor offset. Ratio of coefficients A_2 and A_5 are in direct proportion to linear dependence of sensor temperature sensitivity, while the ratio of coefficients A_3 and A_6 represents the quadratic dependence of sensor temperature sensitivity. Value of p corresponds to the normalized pressure output. The value of p lies within interval /0..1). Value of Δp represents an offset corrected raw readout from capacitive sensor, while the value of ΔT represents the offset corrected raw readout from temperature sensor residing on sensor signal conditioner according to equation (2).

Note that in a given formulations of sensor characteristic description (3) and (4), the actual temperature and capacitance readouts have only indirect significance to final measured quantity p, since the calculation of sensor characteristic description does not depend on actual value of capacitance or temperature.

In case of presented sensor, the pressure dependence of sensor characteristic can be described with linear relationship, while the temperature dependence can be described with quadratic relationship. Measurement resolution was set at 16 bits, maximum obtained resolution of AD7746 for described measurement setup.

The abovementioned observations result in a simplified form of temperature compensation principle for capacitive sensor by setting coefficient A_0 in (2) - the quadratic dependence of capacitive pressure sensor to zero, thus reducing the number of calibration points.

The solution for the unknown coefficients $A_0...A_6$ can be found by solving a system of linear equations, obtained from calibration data, depicted in Figure 7. Seven calibration points are selected and ordered into calibration scenario. Calibration scenario represents a sequence of calibration points, comprised of boundary values, which define the pressure and temperature calibration interval. Remaining calibration points are selected at mid - scale of temperature and pressure range, which result in total nine calibration point mesh. The excess two calibration points are used for verification of total calibration error.

4 Results

Software for acquisition, analysis and calibration of capacitive sensors was designed. Table 1 summarizes the evaluation of data depicted in Figure 7. First seven calibration points were used for evaluation of calibration coefficients.

Additional test points, which were obtained during the acquisition stage of the calibration process, are summarized in Table 2. The first two test points were a part of acquisition of the calibration process and the remaining points were obtained during temperature scan.

Data was first analyzed using a Taylor expansion for coefficient relevance assessment. This description uses 9 calibration points in order to determine all calibration coefficients. Calibration coefficients were obtained by solving a linear system of equations based on Taylor expansion (3). Resulting calibration coefficients are summarized in Table 3. Taylor expansion coefficients confirm the small nonlinearity (A_{02}) of characterized sensor in pressure direction. Furthermore, results in Table 3 show that linear and quadratic terms are dominant for successful sensor compensation, while the small cross " products between pressure and temperature direction indicate, that sensor characteristic evaluation can be simplified.

Table 1: Input calibration data.

CP#	P_{CAL}(mbar)	T(°C)	p_{OC}	T_{OC}
1	0	0	26526	16406
2	1000	0	25767	16406
3	2000	0	25123	16406
4	0	35	26366	16524
5	2000	35	25006	16524
6	0	70	26245	16651
7	2000	70	24902	16651
8	1000	35	25630	16524
9	1000	70	25522	16651

Table 2: Input testpoint data.

TP#	P(mbar)	p_{OC}	T_{OC}	T(°C)
1	1000	25630	16524	35
2	1000	25522	16651	70
3	0	26446	16465	15
4	1000	25698	16465	15
5	2000	25064	16465	15
6	0	26305	16587	55
7	1000	25576	16587	55
8	2000	24954	16587	55

Table 3: Calculated calibration coefficients of Taylor expansion.

A_{00}	1772.47
A_{01}	-1.35
A_{02}	-1.40E-05
A_{10}	-3.49
A_{11}	-8.71E-05
A_{12}	7.18E-07
A_{20}	1.94E-03
A_{21}	1.72E-07
A_{22}	-6.66E-10

Evaluation of a Taylor expansion (2) using coefficients listed in Table 3 was performed. Equation (2) was evaluated at testpoints in Table 2. Results are shown in Table 4, which lists the calibration error Í.

$$\varepsilon = \left| \frac{P_{CAL} - P_{EVAL}}{FS} \right| \cdot 100\% \qquad (6)$$

Where P_{CAL} represents calibration pressure point, P_{EVAL}, evaluation pressure and FS the output pressure span.

Results summarized in Table 4 are in fair agreement with calibration pressure points. A 0.5% discrepancy was found at the endpoint of temperature calibration range at testpoint 8 (*T=70°C*).

Table 4: Evaluation of Taylor expansion.

T_{OC}	p_{OC}	P_{CAL}	P_{EVAL}	$\varepsilon(\%)$
16465	25064	2000	1995.69	-0.22
16465	25698	1000	993.60	-0.32
16465	26446	0	-6.92	-0.35
16587	24954	2000	1995.48	-0.23
16587	25576	1000	992.37	-0.38
16587	26305	0	-9.36	-0.47

Simplification is performed by introduction of Chisholm approximant for sensor characteristic description. Chisholm approximant of degree (1,2) would require 11 calibration coefficients.

This lead to evaluation of a linear Padé (1,1) approximant, which requires 7 coefficients for evaluation. Calibration dataset was taken from first seven calibration points in Table 1. Resulting coefficients are summarized in Table 5.

Table 5: Resulting Padé (1,1) calibration coefficients.

a_{00}	1666.67
a_{01}	-1.47
a_{10}	-0.60
a_{11}	-3.51E-03
b_{00}	1
b_{01}	1.68E-03
b_{10}	5.48E-04
b_{11}	-6.28E-07

Equation (4) was evaluated at testpoints in Table 2. Results are shown in Table 6, which lists the calibration error ε according to equation (4).

Results in Table 6 are in fair agreement with calibration pressure points. A rather large 1.5% discrepancy occurs at the endpoint of temperature calibration range at testpoint 2 (*T=70°C*).

Table 6: Evaluation error at testpoint data.

TP#	$P_{CAL}(mbar)$	$P_{EVAL}(mbar)$	$\lvert\varepsilon(\%)\rvert$
1	1000	1000	0.0
2	1000	1030.7	*1.53*
3	0	-8.7	0.43
4	1000	972.7	*1.36*
5	2000	1995.84	0.20
6	0	−5.32	0.26
7	1000	1011.6	0.58
8	2000	1996.55	0.17

In order to further improve compensation accuracy, a Padé (2,2) approximant was analyzed. A full evaluation of Padé (2,2) approximant would require a set of 17 calibration points, which is unacceptable for mass production of sensors. The original evaluation was therefore normalized with coefficient $4/A_4$ factor and cross products terms of temperature and pressure were neglected. In order to minimize computational errors, coefficients were weighed according to:

$$p=\frac{2^2\cdot\Delta P+2^{-24}\cdot A_0\cdot\Delta P^2+A_1+2^{-9}\cdot A_2\cdot\Delta T+2^{-18}\cdot A_3\cdot\Delta T^2}{A_4+2^{-9}\cdot A_5\cdot\Delta T+2^{-18}\cdot A_6\cdot\Delta T^2} \quad (7)$$

Evaluation of system of linear equations based on equation (7) yields the calibration coefficients summarized in Table 2.

Table 7: Resulting calibration coefficients.

A_0	A_1	A_2	A_3	A_4	A_5	A_6
-8192	-5057	4999	-1391	-12931	2147	-1202

Equation (4) was evaluated at testpoints in Table 3. Results are shown in Table 8. A maximum 0.4% deviation from measured data was found at 0 mbar both at 0 °C and 70 °C, while the compensation remains well in typical industrial sensor applications (0.5% admissible temperature error over entire temperature calibration range).

Table 8: Evaluation error at testpoint data.

TP#	$P_{CAL}(mbar)$	$P_{EVAL}(mbar)$	$\lvert\varepsilon(\%)\rvert$
1	1000	1006	0.3
2	1000	1003	*0.15*
3	0	-8	0.4
4	1000	998	*0.1*
5	2000	1997	0.15
6	0	−7	0.35
7	1000	999	0.05
8	2000	1996	0.2

5 Conclusions

Implementation of a digital temperature compensation method, developed for piezoresistive pressure sensors, to the field of capacitive sensors was presented. Possibilities for the compensation of sensor parameters such as sensor nonlinearity and temperature sensitivity were analyzed. In order to achieve effective compensation and linearization, different digital descriptions of sensor characteristic were investigated and reported, such as two-dimensional rational polynomial description derived from Padé approximations. Evaluation results of sensor response were compared against reference pressure source and most effective digital temperature compensation was proposed. Proposed digital compensation yields maximum 0.4% FS error on a compensation range 0 " 70 °C and enables integer arithmetic, thus making proposed approach appro-

priate for use in modern sensor signal conditioning integrated circuits.

Acknowledgments

This work was performed in cooperation with Hipot - RR, supported by Ministry of Higher Education, Science and technology of Republic of Slovenia within research programme EVSEDI and industrial partner HYB d.o.o. Trubarjeva 7, 8310 Šentjernej, Slovenia

References

/1/ S. R. Norsworthy, R. Schreier, G. C. Temes, "Delta-Sigma Data Converters" IEEE Press, 1997, Wiley-IEEE Press, ISBN: 978-0780310452.

/2/ J. C. Candy, G. C. Temes, "Oversampling Delta-Sigma data converters", IEEE Press, Publisher: Wiley-IEEE Press, 2008, ISBN: 978-0879422851.

/3/ O'Dowd, J. Callanan, A. Banarie, G. Company-Bosch, E "Capacitive sensor interfacing using sigma-delta techniques" Sensors, 2005 IEEE, pp.-951-954, ISBN: 0-7803-9056-3. Digital Object Identifier: 10.1109/ICSENS.2005.1597858

/4/ Markus Bingesser, Teddy Loeliger, Werner Hinn, Johann Hauer, Stefan Mödl, Robert Dorn, Matthias Völker "Low-noise sigma-delta capacitance-to-digital converter for Sub-pF capacitive sensors with integrated dielectric loss measurement" Proceedings of the conference on Design, automation and test in Europe, Munich, Germany, 2008, pp. 868-872.

/5/ Analog Devices AD7746 Evaluation Board - EVAL-AD7746EB, Revision 0, May 2005. Available on: http://www.analog.com/static/imported-files/eval_boards/252730993EVAL_AD7746EB_0.pdf

/6/ Susan Pratt "Environmental Compensation on the AD7142: The Effects of Temperature and Humidity on Capacitance Sensors" Analog Devices Application Note AN-829, 2005. Available on: http://www.analog.com/static/imported-files/application_notes/577315308337353595863 3AN829_0.pdf

/7/ Belavič Darko, Santo-Zarnik Marina, Hrovat Marko, Maček Srečo, Kosec, Marija. "Temperature behaviour of capacitive pressure sensor fabricated with LTCC technology" Inf. MIDEM, 2009, vol. 38, no. 3, pp. 191-196.

/8/ IEEE Std. 1451.2 D3.05-Aug1997 "IEEE standard for a smart transducer interface for sensors and actuators - Transducer to microprocessor communication protocols and transducer electronic data sheet (TEDS) formats" Institute of Electrical and Electronics Engineers, September 1997.

/9/ MOŽEK, Matej, VRTAČNIK, Danilo, RESNIK, Drago, ALJANČIČ, Uroš, AMON, Slavko. Fast algorithm for calculation of measured quantity in smart measurement systems, 39th International Conference on Microelectronics, Devices and Materials and the Workshop on Embedded Systems, October 01. " 03. 2003, Ptuj, Slovenia. Proceedings. Ljubljana: MIDEM - Society for Microelectronics, Electronic Components and Materials, 2003, pp. 111-116.

/10/ Baker, George A. Graves-Morris, P. R., Padé approximants. #Part #1, Basic theory, Reading (Mass.) /etc./ : Addison-Wesley, 1981, (Encyclopedia of mathematics and its applications ; #vol. #13).

/11/ ZMD31020 Advanced Differential Sensor Signal Conditioner Functional Description Rev. 0.75, (2002) ZMD AG.

doc. dr. Matej Možek
doc. dr. Danilo Vrtačnik
doc. dr. Drago Resnik
Borut Pečar, univ. dipl. inž. el.
prof. dr. Slavko Amon

University of Ljubljana,
Faculty of Electrical Engineering,
Laboratory of Microsensor Structures and Electronics
Trzaska 25, Ljubljana 1000, SLOVENIA
e-mail: matej.mozek@fe.uni-lj.si
Telefon: 01 4768 380, Telefax: 01 4264 630

Prispelo (Arrived): 26.09.2009 *Sprejeto (Accepted): 09.03.2010*

THE BENCHMARKING OF FORCE SENSORS FOR THE WEIGHING OF SMALL MASSES IN COST-SENSITIVE APPLICATIONS

Roman Pačnik[1], Darko Belavič[2], Marko Hrovat[3], Marija Kosec[3]

[1]BSH hišni aparati d.o.o., Nazarje, Slovenia
[2]HIPOT-RR, d.o.o., Otočec, Slovenia
[3]Jožef Stefan Istitute, Ljubljana, Slovenia

Key words: weighing instruments, force sensors, strain gauges, characterization, sensitivity

Abstract: An overview of the requirements for weighing instruments is presented and some of the sources of the measurement errors are discussed. Four types of force sensors, intended for use in small kitchen appliances, with an integrated scale were constructed and evaluated. The sensing elements for two types were thick-film resistors, and for the other two types they were diffused resistors on silicon dies. In the case of the first two types the substrates with the thick-film resistors were bonded on to metallic spring elements. The other two types of sensors are based on the so-called force-to-pressure transformation principle and are known as hydraulic (or hydrostatic) force sensors. The sensitivities of the sensors with silicon sensing elements were between 10 to 20 times higher than the sensitivities of sensors with thick-film resistors. The offset voltages of the unloaded force sensors were significantly higher for the hydraulic force sensors with silicon sensing elements. Also, the temperature coefficients of the resistivities of thick-film resistors (around or below 100×10^{-6} /K) were much lower than the values for the resistors on silicon dies.

Primerjalna analiza senzorjev za tehtanje majhnih mas za uporabo v nizko-cenovnih napravah

Kjučne besede: tehtnice, senzorji sile, merilniki mehanskih deformacij, karakterizacija, občutljivost

Izvleček: V začetku članka predstavljamo osnovne zahteve za tehtnice. Opisali smo nekatere vzroke napak pri tehtanju. Konstruirali, izdelali in testirali smo štiri tipe senzorjev sile, primernih za vgradnjo v male gospodinjske aparate z vgrajeno tehtnico. Dva tipa senzorjev uporabljata senzorske elemente na osnovi debeloplastnih uporov, medtem ko pri drugih dveh izkoriščamo pretvorbo sile v tlak (hidravlični senzorji sile) in pri tem uporabljamo kot senzorske elemente difundirane upore na silicijevih tabletkah. Temperaturni koeficienti upornosti debeloplastnih uporov (okrog ali pod 100×10^{-6} /K) so za več kot velikostni razred manjši kot temperaturni koeficienti upornosti difundiranih uporov na silicijevih tabletkah. Pri senzorjih sile z debeloplastnimi upori so keramični substrati prilepljeni na kovinsko vzmetno telo. Hidravlični senzorji sile so napolnjeni s tekočino (silikonsko olje), ki je medij pri pretvorbi sile v tlak. Občutljivost senzorjev s silicijevimi senzorskimi elementi so deset do dvajset krat večje, kot občutljivosti senzorjev z debeloplastnimi upori. Ničelne napetosti neobremenjenih senzorjev sile so precej višje za hidravlične senzorje sile.

1. Introduction

A weighing instrument is a device that determines the mass of a body by using the action of gravity on this same body. The instrument may also be used to determine other quantities, magnitudes, parameters or characteristics related to the determined mass. The accuracy classes for weighing instruments, their symbols and typical fields of use are given in Table 1 /1/.

Table 1: Symbols for accuracy classes and typical fields of use /1/.

Mark	Name	Typical use
(I)	special accuracy	laboratory
(II)	high accuracy	trading with jewelry
(III)	medium accuracy	general trading
(IIII)	ordinary accuracy	general use

However, unless precautions are taken to correct for local gravity, air buoyancy and a number of other factors, the declared accuracy of the scale cannot usually be realized. In fact, considerations that are often overlooked can result in a significant error, especially with scales that have a higher accuracy. Some of those concerns are described in /2/.

Latitude is the most significant variable in determining the acceleration due to gravity. This acceleration (g) varies from 9.780 m/s^2 at the equator to 9.832 m/s^2 at the poles and can cause an error of up to 0.53 % in the final result of the weighing. Altitude also has a great influence, since the gravitational attraction to the earth at a particular location varies as the square of the distance from the centre of mass of the earth. These variations can cause an error of up to 0.26 % over the surface of the earth. Variations in the acceleration due to gravity, because of position and height, result in a change in the weight of an object by about 0.8 % over the surface of the earth. Objects being measured displace a volume of air, which has a density of approximately 1.2 kg/m^3, and whose density can vary due to weather. The resulting "upward" force is a function of the object's size. For large, low-density objects a failure to correct for buoyancy may result in an error of 0.5 %, or even more. Other concerns (i.e., tidal effects, gravitational anomalies,

electrostatic and magnetic attractions to nearby objects, air currents) can be neglected, except in the case of very precise measurements.

Kitchen scales are intend for personal use and are, therefore, not metrologically inspected at the place of use. Usually, these can be classified in the ordinary accuracy class (III) according to Table 1. This is why all these scales are manufactured and adjusted to a standard defined acceleration due to gravity, which is 9.80665 m/s^2. However, since there are for personal use the producer can "freely" choose the parameters and declare the precision.

The tendency in small kitchen appliances, especially for kitchen robots and food processors, is to integrate the function of the scale into the appliance. Usually, four force sensors (load cells) are used and integrated into the bottom of appliance. In this case, low-cost sensors are preferred. In such a case the integrated force sensors are loaded with the mass of the appliance (dead load) as well as with the mass being weighed. This dead load can be equal or even greater than the load that will be measured. In such a case, force sensors for a higher measuring range must be used and the actual measuring range is only a part of the declared measuring range of the sensor.

The aim of this paper is to benchmark different types of force sensors that can be used in certain types of small household appliances for weighing applications. Four types of force sensors were studied and evaluated.

The first two types of evaluated force sensors are based on thick-film technology, where the sensing piezoresistive resistors are screen printed and fired on an alumina substrate. The change in resistance of the resistors under an applied stress is partly due to the deformation, i.e., changes in the dimensions of the resistor, and partly due to an alteration in the specific resistivity as a result of microstructural changes /3, 4/. The gauge factor (GF) of a resistor is defined as the ratio of the relative change in the resistance ($\Delta R/R$) and the strain (ε), defined as ($\Delta l/l$), and is described by equation (1).

$$GF = (\Delta R/R)/(\Delta l/l) = (\Delta R/R)/\varepsilon \qquad (1)$$

Geometrical factors alone result in gauge factors of 2-2.5. Higher gauge factor values are due to microstructural changes, which alter the specific conductivity. The GF values of thick-film resistors are mostly between 3 and 15, and are higher than those of metal strain gauges (GF ~2) and lower than those realized with semiconducting elements (GF 50-200) /3, 4/. In the first type of force sensor, four thick-film sensing resistors are screen printed and fired on an alumina substrate, which is bonded to an aluminium double bending beam spring element (more details in Section 2.1). With a special design of this element, areas with concentrated strain can be achieved. Sensing resistors, which are connected in a Wheatstone bridge, are placed at the areas where the highest strain occurs. A simple planar construction of the spring element is used for the second type of force sensor. The alumina substrates with two screen-printed and fired thick-film resistors are bonded to the spring element, which is punched out from a steel plate. Since only two sense resistors are used, two additional fixed resistors of the same value are needed to realize half of the Wheatstone bridge circuit.

The third and fourth types of evaluated sensors based on the so-called force-to-pressure transformation principle are known as hydraulic (or hydrostatic) force sensors. Such kinds of force sensors are also generally known as hydraulic load cells. Hydraulic force sensors are force-balance devices, measuring force as a change in the pressure of an internal filling fluid. A force acting on a loading head is transferred to a piston, which in turn compresses a filling fluid confined within an elastomeric diaphragm chamber. As the force increases, the pressure of the hydraulic fluid rises. A pressure sensor - in these two cases with a small-sized piezoresistive absolute-pressure sensor chip - measures the fluid pressure. With such a kind of transformation the voltage output signal of the pressure sensor is proportional to the force that acts on the loading member of the sensor. Hydraulic force sensors are generally used to measure relatively large forces (i.e., from 500 N upwards) in harsh and industrial environments. The output is linear and relatively unaffected by the amount of filling fluid. With careful design and manufacturing, the accuracy can be within 0.25 % full scale /5/, but in general their accuracy is 0.5 % to 1 % of full scale.

The housing of the third type of force sensor is made from plastic and closed with rubber on one side. The interior is completely filled with fluid - a silicon oil is used. At the upper side of the force sensor the absolute silicon pressure sensor chip is bonded onto the ceramic substrate and through the contact pins connected to the measuring system. This type of sensor is described in Section 4 in more detail.

The forth type of force sensor is made from a copper-based metallic housing. A hydroformed metallic bellows is used as the loading member and this is soldered together with the base housing of the sensor. An absolute silicon pressure sensor is bonded to a hermetically closed TO-5 transistor header, which is soldered onto the body of the sensor. The details of this hydraulic force sensor are described in Section 5.

The most important characteristics of force sensors are non-linearity, hysteresis error, sensitivity and repeatability. Non-linearity is the deviation from a straight line of the increasing force sensor signal output curve. For this benchmarking, the linear approximation between the first and last measured points was taken. The hysteresis error is defined as the difference between the force-sensor readings for the same applied load: one reading obtained by increasing the load from the minimum load and the other by decreasing the load from the maximum load. The sensitivity is the ratio of the change in the response (output) of a force sensor to a corresponding change in the stimulus (load applied). Repeatability is the ability of a force sensor to

provide successive results that are in agreement when the same load is applied several times and applied in the same manner on the force sensor under constant test conditions.

In this paper, measurements of these characteristics of the evaluated sensors are compared and discussed.

2. Force sensor with double bending beam with tHick-film strain gauge

2.1 Design and construction

The double bending beam (also called a binocular form beam) is often used as a spring element in force sensors. The key parts of the spring element are the two "weak" points, with the aim to concentrate the strain induced by the applied force on the sensing resistors /6/. The double bending spring element is presented in Fig. 1 and the two "weak" points are shown in Fig. 2.

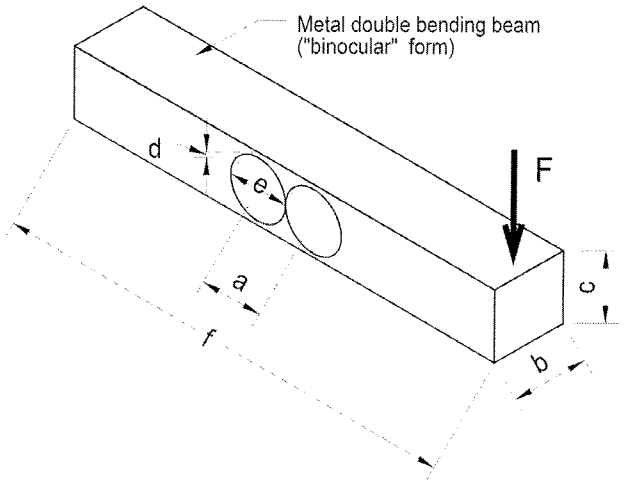

Fig. 1: The double bending spring element.

The strain in the most sensitive part of the beam is described by equation (2)

$$\varepsilon = \frac{1.5\,Fa}{Ebd^{2}} \qquad (2)$$

where the strain (m/m) is a function of the applied force, *F* (N), the Young's modulus, *E* (Pa), and the dimensions *a* (m), *b* (m) and *d* (m), as denoted in Fig. 1. The working principle of the double bending beam is schematically shown in Fig. 2. The strain is concentrated in two points: the positive (tensile) strain is concentrated in the first weak point, and the negative (compressive) strain is concentrated in the second weak point, marked in Fig. 2 by *R+dR* (the increase of resistance) and *R-dR* (the decrease of resistance), respectively.

In our case the force sensor converts a mechanical quantity (force) into strain, and then translates it into an electrical signal (voltage) using the resistance change of the thick-film sensing resistors printed and fired on the alumina substrate. The thick-film strain gauge, i.e., the ceramic substrate with the thick-film sensing resistors, is shown in Fig. 3. The working principle of the thick-film strain gauge is piezoresistivity - the property of resistor materials to change their resistivity under strain. Four thick-film sensing resistors are located on the double bending beam, so that two are under tensile strain, and two are under compressive strain. Sensing resistors are placed on the positions of the maximum tensile and compressive stains on the double bending beam. These four sensing resistors are electrically connected in a Wheatstone-bridge configuration and are excited with a stabilized bridge voltage (Fig. 4). The output of such a strain gauge is the voltage vs. strain induced by the applied force.

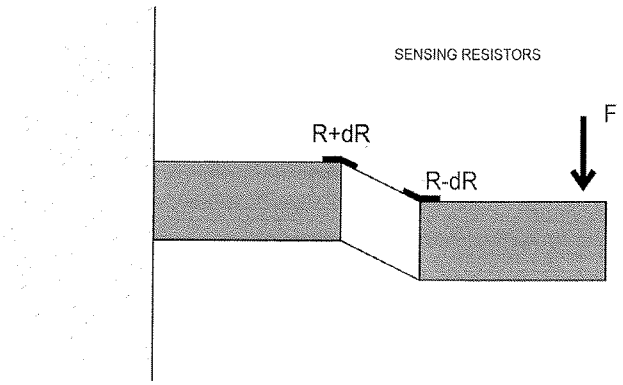

Fig. 2: Working principle of the double bending beam.

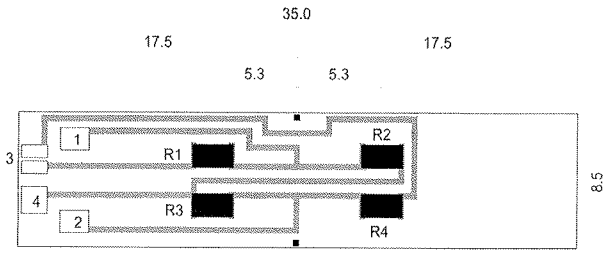

Fig. 3: Alumina substrate with thick-film resistors connected in a Wheatstone bridge.

The aluminium double bending beam, shown in Fig. 1 (and described by equation (2)), was designed with the following dimensions: a = 10.6 mm, b = 13 mm, c = 12 mm, d = 1.2 mm, e = 10 mm, and f = 80 mm. The material for the double bending beam is aluminium, which has a Young's modulus of 73 GPa, and a thermal expansion coefficient of 23×10^{-6}/K. The thick-film strain gauge shown in Fig. 3 consists of four thick-film resistors printed and fired on the alumina substrate. Sensing resistors have a resistance of 1300 ohm and have a value for the gauge factor of around 8. The thick-film strain gauge is bonded with glue onto the aluminium double bending beam. An example of the realized force sensors with the thick-film strain gauge is shown in Fig. 5.

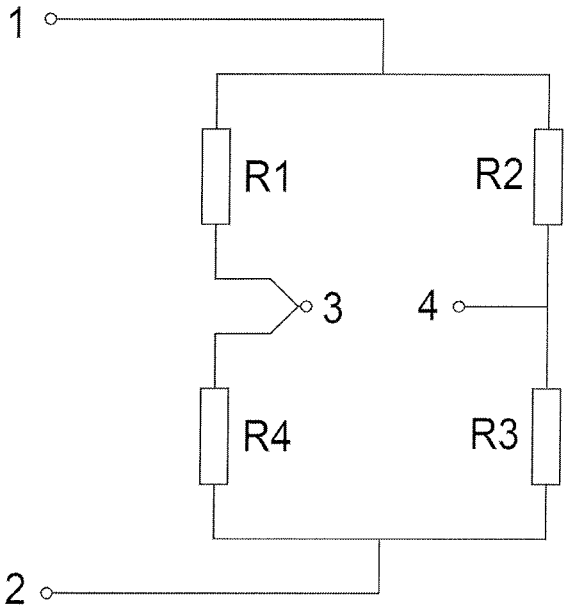

Fig. 4: Four sensing resistors connected in a Wheatstone bridge.

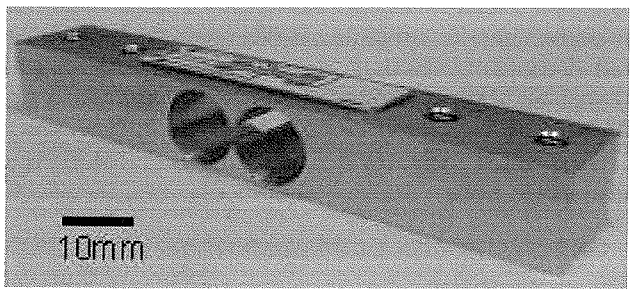

Fig. 5: The thick-film strain gauge on the alumina substrate is bonded on a double bending aluminium spring element.

2.2 Results

The fabricated samples (see Fig. 5) were mechanically fixed on one side and loaded with different forces (loads) on the other side. The thick-film strain gauges were excited with a stabilized bridge voltage of 5 V and the output voltage was measured. All the test samples were tested at different applied forces (weighing loads). The range of the applied forces was from 0 N to 34 N (0–3.4 kg). The output voltage versus loading force for a typical test sample is presented in Fig. 6.

The calculated force sensitivity from the measured data is about 45 μV/V/N. Some other characteristics of this type of force sensor with a thick-film strain gauge are presented in Section 6, Table 2. The non-linearity is 0.2 %, the hysteresis error is less than 0.2 %, and the offset voltage of the unloaded sensor is up to ±4 mV.

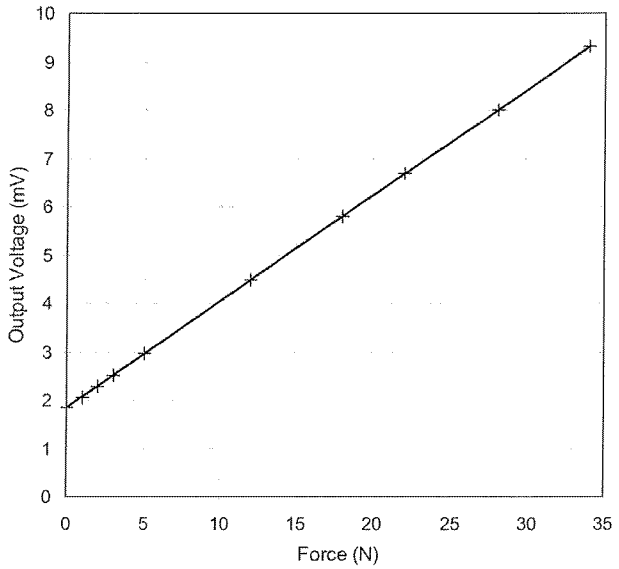

Fig. 6: Output characteristics of the force sensor with a thick-film strain gauge.

3. Thick-film double bending planar force sensor

3.1 Design and construction

A thick-film double bending planar force sensor was evaluated. The spring element, with outer dimensions of 32 mm x 29.9 mm, and with an 8-mm-wide and 18.6-mm-long flexure bar, is punched out from a 1.2-mm-thick sheet of 1.4016 ferritic steel. The Young's modulus, the Poisson's ratio and the thermal expansion coefficient of this steel are 200 GPa, 0.3 and 12×10^{-6}/K, respectively. The alumina substrate with screen-printed and fired sensing resistors is glued onto the flexure bar. The spring element with the glued alumina substrate on the double bended flexure bar is presented in Fig. 7.

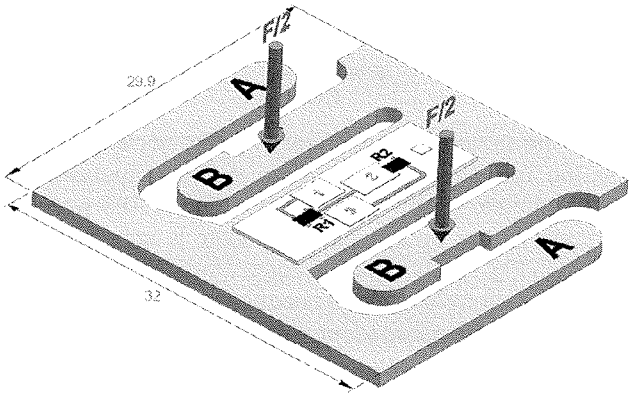

Fig. 7: Main dimensions of the double bending spring element where the outer arms are marked with A and the inner arms are marked with B.

The spring element consists of three key parts. Two outer arms, marked with A, are meant to be on a fixed support.

Both inner arms, marked by B, are loaded, through a special connecting mechanical structure, with the applied force.

The force is applied equally on both inner arms. The thick-film strain gauge is realized with two thick-film resistors printed and fired on alumina. The force sensor converts the mechanical quantity (force) into a strain and translates it into an electrical signal (voltage) using the resistance change in two sensing resistors.

Both resistors are trimmed to a resistance value of 10,000 ohm and are electrically connected to half the Wheatstone-bridge (two additional resistors are needed on the measurement side). The sensing resistor R1 lies on the positive (tensile) strain, while the sensing resistor R2 lies on the negative (compressive) strain. The alumina substrate with two thick-film sensing resistors and the main dimensions are schematically shown in Fig. 8.

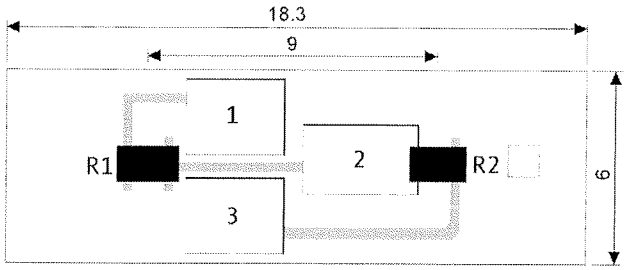

Fig. 8: Alumina substrate with two thick-film resistors. The contact pads are marked with 1, 2 and 3.

When a force is applied on the spring element of the force sensor a typical double bending of the flexure bar occurs. The deformation of the spring element under applied force was simulated using the finite-element method /7/. In Fig. 9 the deformation and the normal component of strain, which is along the axis of the flexure bar, are shown - for better clarity the deformation is over scaled. Lighter areas represent the areas under tensile strain and the darker areas represent the areas under compressive strain.

The strain reaches its peak value at both ends of the flexure bar. The peak values of the positive and negative strains are almost identical. At the areas of the maximum peaks there is also a lot of transverse strain. It is well known that the sensing resistors are also sensitive to transverse strain /8/.

To minimize the measuring error the influence of the transverse strain must be minimized. To achieve this, the sensing resistors are placed away from the areas of maximum strain and some sensitivity is sacrificed for a better accuracy. In the case of an uneven load to both inner arms a twisting of the flexure bar occurs. To minimize this effect, both sensing resistors are placed on a symmetric axis along the flexure bar.

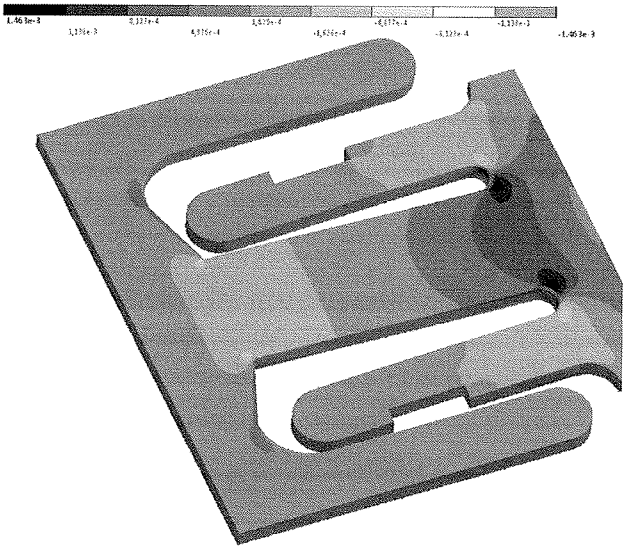

Fig. 9: Planar force sensors under an applied force. The normal component of strain (along the axis of the flexure bar) and the over-scaled mechanical deformation.

3.2 Results

The samples were supported under both outer arms and loaded with different forces (loads) through the mechanical structure on both inner arms, which are located on the other side of the flexure bar. The range of the weighting loads was from 20 N to 32 N, with 20 N of preload (dead load). The thick-film strain gauges were excited with a stabilized bridge voltage of 3.3 V and the output voltage was measured. An additional two resistors of 10 kΩ were used to complete the Wheatstone bridge and to achieve more accurate measurements. The output voltage versus the loading force for a typical test sample is presented in Fig. 10.

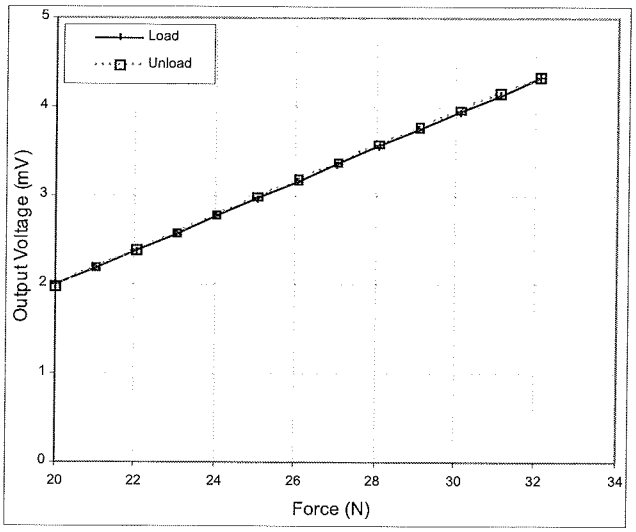

Fig. 10: Output characteristics - voltage vs. force - of the planar force sensor with a thick-film strain gauge.

The calculated force sensitivity from the measured data is about 58 μV/V/N. Some other characteristics of this type of force sensors with a thick-film strain gauge are presented in Section 6, Table 2. The non-linearity is 0.3 %, the hysteresis error is less than 0.4 %, and the offset voltage of the no-load sensor is up to ±4 mV.

4. Hydraulic force sensor with plastic housing and rubber meMbrane

4.1 Design and construction

The housing of this hydraulic force sensor is made from glass-reinforced Nylon (PA66-GF30). EPDM (ethylene-propylene-diene Monomer) rubber was vulcanized directly onto the plastic housing on a specially designed and custom-made moulding tool.

In Fig. 11 the main dimension of the realized force sensor in cross-section is shown.

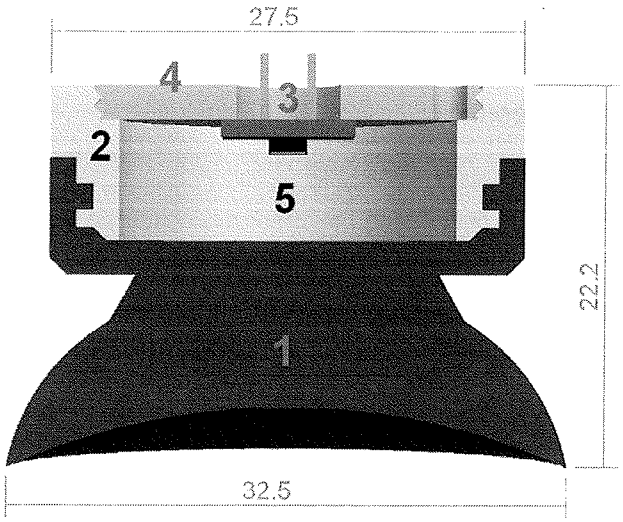

Fig. 11: Hydraulic force sensor with main dimensions. The rubber part (denoted by 1) is vulcanized directly to the plastic body (denoted by 2).

As already mentioned, the plastic housing (denoted by 2) was made from reinforced nylon. The surfaces that are in contact with the rubber were treated with a special primer 24 hours before the vulcanization to ensure a reliable junction between the plastic housing and the rubber part (denoted by 1). The rubber part functions as a membrane for the hydraulic force sensor and also as suction feet on the other side. After the vulcanization of the rubber to the plastic housing, the cover lid (denoted by 4) with a sensing element (denoted by 3) is placed onto the plastic body. The sensing element is an absolute silicon pressure chip bonded onto the alumina substrate.

Through four contact pins a sensing element is connected to a measurement system. The interior (denoted by 5) is filled with fluid - a Wacker AK100 silicon fluid is used. After the filling process both the filling holes were sealed. In Fig. 12 a fabricated sample of the hydraulic force sensor with a plastic housing and a rubber membrane is presented.

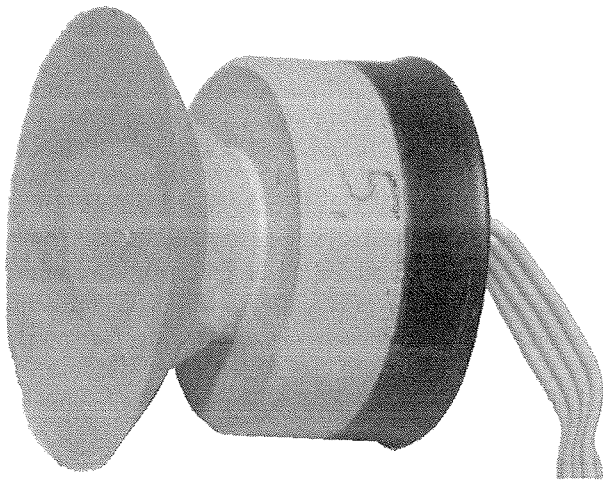

Fig. 12: Hydraulic force sensor with plastic housing and integrated vacuum suction feet.

4.2 Results

The fabricated samples (shown in Fig. 12) were loaded with different forces (loads). The silicon pressure chip was excited with a stabilized bridge voltage of 3.3 V and the output voltage was measured. The range of the measured forces was from 20 N to 32 N, with 20 N of preload (dead load). The output voltage versus loading force for a typical test sample is presented in Fig. 13.

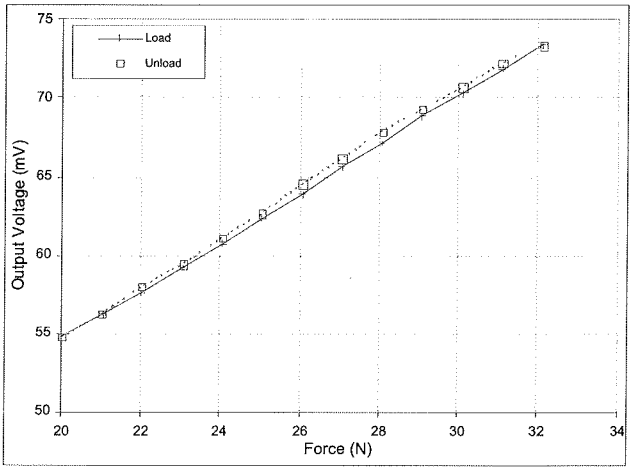

Fig. 13: A force-to-pressure transformation, sensor made from plastic and rubber.

The calculated force sensitivity from the measured data is about 470 μV/V/N. Some other characteristics of this type of force sensor with a silicon pressure sensor are presented in Section 6, Table 2. The non-linearity is 1.5 %, the hysteresis error is around 3.5 % and the offset voltage of the no-load sensor is up to 25 mV.

5. Hydraulic force sensor with METALLIC body

5.1 Design and construction

This type of force sensor is made from metallic parts. A cross-section of such a construction is shown in Fig. 14. With such a construction, better measurement parameters of the hydraulic force sensor were expected (based on the hydraulic force sensor described in Section 4). A copper cap (denoted by 1) with a 1-mm-thick wall and an 8.2-mm hole at the bottom is used as the housing for this type of hydraulic force sensor. A hydroformed metal bellows (denoted by 2), which is made from phosphor bronze, is soldered at the other side of the copper cap. The metal bellows with three convolutions of 19.1 mm for the outside diameter and a 0.1-mm-thick wall is designed for a nominal pressure of 200 kPa. Since one convolution is soldered to the housing only two of them are actually active.

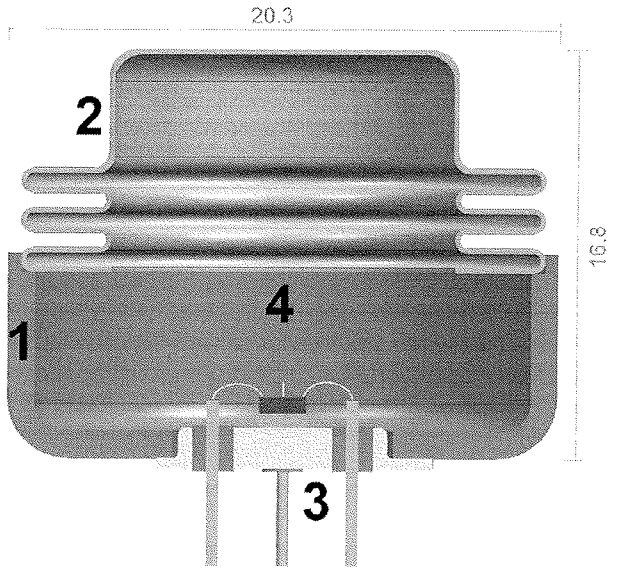

Fig. 14: Hydraulic force sensor with metallic body and metal bellows in cross-section.

An absolute silicon pressure chip is placed on the TO-5 transistor header (denoted by 3) and electrically connected with bonded wires to four connecting pins. The connecting pins are insulated with glass and hermetically sealed. Through these four contact pins a sensing element is connected to a measurement system. The interior (denoted by 4) is filled with fluid - a Wacker AK100 silicon fluid, like in the case of the hydraulic force sensor with the plastic housing (see Section 4.1). The realized hydraulic force sensor with a metallic body is presented in Fig. 15.

5.2 Results

The fabricated samples (shown in Fig. 15) were loaded with different forces (loads). The silicon pressure chip was excited with a stabilized bridge voltage of 3.3 V and the output voltage was measured. The range of the measured

Fig. 15: Hydraulic force sensor realized with metallic body and metal bellows.

forces was from 20 N to 32 N, with 20 N of preload (dead load). The output voltage versus loading force for a typical test sample is presented in Fig. 16.

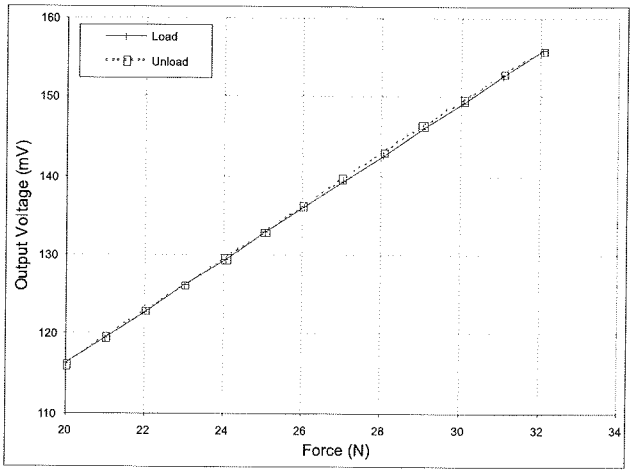

Fig. 16: A force-to-pressure transformation made from the hydroformed bellows.

The calculated force sensitivity from the measured data is about 1000 μV/V/N. Some other characteristics of this type of force sensors with a silicon pressure sensor are presented in Section 6, Table 2. The non-linearity is 0.3 %, the hysteresis error is less than 0.8 %, and the offset voltage of the no-load sensor is up to 60 mV.

6. Benchmarking and conclusions

The force sensors for weighing small masses in cost-sensitive applications can be realized with different types of sensing elements. Four types of sensing element were investigated:

Table 2: Some characteristics of force sensors realized with different types of sensing elements

Characteristics	Type 1	Type 2	Type 3	Type 4
Resistance (Ohm)	1300	10 000	3500	3500
TCR (10^{-6}/K)	± 100	± 100	~ 2800	~2800
Non-linearity error (%)	0.2	0.3	1.5	0.3
Hysteresis error (%)	0.2	0.4	3.5	0.8
Sensitivity (μV/V/N)	45	58	470	1000
Offset (mV)	± 4	± 4	± 25	±60

Type 1: Force sensor realized with a double bending beam with a thick-film strain gauge

Type 2: Force sensor realized with a double bending planar spring element with a thick-film strain gauge

Type 3: Hydraulic force sensor with a plastic housing and rubber feet as a load-member part.

Type 4: Hydraulic force sensor with a metallic housing and a metal bellows.

Some characteristics of the realized force sensors with different types of sensing elements are presented in Table 2. The resistances and temperature coefficient of resistivity (TCR) are given. The measured and calculated values for the non-linearity errors, the hysteresis errors, the sensitivities and the offset voltages (unloaded samples) are presented.

The TCRs of thick-film resistors (types 1 and 2) are around 100×10^{-6}/K and are much lower than the TCRs on silicon pressure sensor chips, which were used as the sensing elements for the types 3 and 4 hydraulic force sensors. The non-linearity errors were similar for the types 1, 2 and 4 force sensors, while for the type 3 force sensor the values were five times higher. The hysteresis errors were around 3.5 % for the type 3 - hydraulic sensors with plastic housing, while for the other types the values were below 1 %. The sensitivities of the sensors with silicon sensing elements were between 10 to 20 times higher than the sensitivities of the sensors with thick-film resistors. On the other hand, the offset voltages of the unloaded force sensors were significantly higher for the hydraulic force sensors with the silicon sensing elements.

Acknowledgements

Authors would like to acknowledge Ministry of Higher Education, Science and Technology for financial support within the grant Young Researcher from Industry (3211-05-000526). The authors gratefully acknowledge Mr. Srečko Maček (Jožef Stefan Istitute) for his help during the experiments. The authors are indebted to Mr. Toni Pogačar (BSH Hišni aparati d.o.o.) for the helpful discussions of obtained results.

References

/1/ OIML International recommendation OIML R 76-1 edition 2006 (E), Non-automatic weighing instruments, International organization of legal metrology, 2006

/2/ R. Boynton, Precise measurement of mass, 60_{th} Annual Conference of the Society of Allied Weight Engineers, 2001, Arlington, Texas

/3/ K. Hoffman, An introduction to measurements using strain gauge, Hottinger Baldwin Messtechnik GmbH, Darmstadt, 1989

/4/ M. Hrovat, D. Belavič, A. Benčan, J. Holc, W. Smetana, H. Homolka, R. Reicher, The characterization of thick-film resistors on dielectric-on-steel substrates for strain gauge applications, Sensors and materials, Vol. 15, 2003, 247-257

/5/ OMEGA press, Transactions in measurements and control, Volume 3 - Force-related measurements, Omega, http://www.omega.com/literature/transactions/Transactions_Vol_III.pdf

/6/ D. Belavič, M. Hrovat, M. Pavlin, M. S. Zarnik, Thick-film technology for Sensor Applications, Informacije MIDEM, Vol. 33, 2003, 45-48

/7/ S. Moaveni, Finite element analysis, Theory and application with ANSYS, Prentice Hall, Third edition, 2008

/8/ M.S. Zarnik, D. Belavič, F. Novak, Finite-element model-based fault diagnosis, a case study of ceramic pressure sensor structure, Miroelectronics Reliability, nr. 47, 2007, 1950-1957

Roman Pačnik univ. dipl.ing. el.
BSH hišni aparati d.o.o.
Savinjska cesta 30
SI-3331 Nazarje
Slovenia
Phone: +386 (0)3 83 98 239
E-mail: roman.pacnik@bshg.com

Prispelo (Arrived): 02.03.2010 *Sprejeto (Accepted): 09.03.2010*

SIB: SENSOR INSTRUMENTATION BUS FOR POWER AND ENERGY CONTROL UNITS

Uroš Platiše, Mihael Mohorčič

Institut "Jožef Stefan", Ljubljana, Slovenija

Key words: SIB, MAC, MSG, Protocol, Layer, Sensor, Power, Energy, Management, Monitoring, Control

Abstract: Power and energy management in buildings, be in households, offices or in industry, is becoming increasingly important for cost as well as for carbon footprint reduction. However, in addition to power and energy management algorithms, high availability and redundancy remain key system requirements. In this paper we present a novel low cost instrumentation bus for modular system architectures, considering modular units as distributed sensors and actuators. In particular, as a show case we apply the proposed instrumentation bus for Power and Energy Control (PEC) units, providing modularity, general connectivity, high availability, scalability and future system upgradeability. Drawing analogy with sensor and actuator networks the proposed instrumentation bus also guarantees very low protocol overhead and thus maximizes the throughput of the bus.

SIB: Senzorsko instrumentacijsko vodilo za modularno krmiljenje električne moči in energije

Ključne besede: SIB, MAC, MSG, protokol, plast, senzor, moč, energija, upravljanje, nadzor, krmiljenje

Izvleček: Upravljanje in nadzor energije v gospodinjstvih, poslovnih objektih in industriji postaja vse pomembnejše, tako z namenom zmanjševanja stroškov kot tudi emisij CO_2. Poleg algoritmov upravljanja z energijo ostajata visoka dostopnost sistema in redundančnost zelo pomembni lastnosti sistema. V tem članku predstavljamo nov koncept instrumentacijskega vodila za modularne arhitekture implementirane v "Power and Energy Control (PEC)" modulih za upravljanje z močjo in energijo. PEC moduli tako pridobijo modularnost, skalabilnost, visoko dostopnost, povezljivost z drugimi sistemi in nadgradljivost ter kompatibilnost z novejšimi (prihodnjimi) modeli.

1. Introduction

World trends of power consumption are continuously increasing, causing high or even excessive power demands in distribution grids as well as in energy generation. Several initiatives have been started under the term "Demand Response" or "Automatic Demand Response", with the goal to reduce the total or peak power consumption. Some of the available solutions for power and energy management are based for instance on ZigBee wireless devices /1/ or Echelon distributed wired devices /2/, while Siemens /3/ and General Electric provide systems based on Programmable Logic Controllers (PLC's). Entirely distributed systems, such as ZigBee and Echelon, may have problems with availability due to unstable communication channel between control units, which is for instance at 2.4 GHz for ZigBee not guaranteed. Furthermore, distributed solutions exhibit time delay issues when the number of controlled devices is increasing. PLC based systems, on the other hand, are costly and are typically used in the industry, where in addition to power and energy management they are also used to control industrial processes.

Particularly important requirements for power and energy management systems are their scalability and upgradeability. This is calling for a modular approach, which has already been introduced by profibus /4/, modbus /5/, echelon /2/, linbus /6/ and others, providing suitable protocols for communication between modules. Typical weaknesses of those protocols are as follows:

- Protocols are in most cases not self-describing, so a custom application is required in order to be able to understand, monitor and control module's parameters.
- Protocols may introduce significant overhead (such as in the case of widely used Extensible Markup Language, XML), or when compressed, they may only be manageable by powerful devices.
- Master-slave oriented architecture makes modules non-autonomous and dependent.
- Static binding of variables limits future upgradability and compatibility across modules.

In this paper we propose an instrumentation bus with tiny distributed protocol stack. This protocol is a subset of a Sensor Standard General Language (SSGL) /7/, a protocol stack originally developed for low-power sensor networks. We refer to the proposed hardware implementation of the instrumentation bus and the respective protocol stack as Sensor Instrumentation Bus (SIB) and consider modular units attached to the bus as distributed sensors and actuators. We implemented SIB for interconnection of Power and Energy Control (PEC) modules, designed to limit and reduce maximum power demand requirements within households and industry, and to provide energy saving functions. PECs follow modular approach and contain distributed protocol stack with the aim to offer high-availability, redundancy, future upgradeability and installation simplicity.

The rest of the paper is organised as follows. In Section 2 we briefly describe hardware features and modules of SIB

instrumentation bus. In Section 3 we provide an overview of the SIB protocol. Section 4 presents PEC modules as compact autonomous units implementing the proposed SIB instrumentation bus and protocol stack, and Section 5 concludes the paper.

2. Sensor Instrumentation Bus

The main purpose of SIB is to provide low cost instrumentation platform that suits applications in households, industrial fields, automated test environment (ATE) and low-power sensor networks. In the following we provide an overview of its basic features and structure of its modules.

2.1 SIB Basic Features

SIB is based on standard and well established technologies:

- DIN housing suitable for standard electric cases.
- Low-cost communication Inter-Integrated Circuit I2C bus.
- Universal Asynchronous Receiver/Transmitter (UART).
- High-speed point-to-point or multi-point Low-Voltage Differential Signalling (LVDS).

SIB provides decentralised control for a cluster of completely independent modules, where:

- Each module is autonomous and thus self-sufficient.
- Communication between modules is completely decentralised, with no central coordinator nor central processing module.
- Cluster consists of *n* modules stacked in an array sharing a global communication channel and having direct communication channels with adjacent modules to ensure fast communication and short response times.
- Clusters scale via additional isolated communication channel.
- Each module comprehends self-describing protocol for autonomous configuration and understandable human interface.

2.2 SIB Modules

Considering the degree of functionality we define the following classes of modules that can connect via SIB:

- Dependent Modules or Primitive Modules incorporate the minimum set of functions and layers to co-exist in a system and require intelligent modules or bridges for in-system integration. Such modules are typically accessed via I2C or UART bus.
- Independent Modules or Intelligent Modules incorporate all necessary layers to be completely independent. These modules handle communication with other modules on their own. PEC modules belong to this class.
- Bridges provide interfaces to other devices and to external systems for large scale integration. They take control over primitive modules for inter-connection with intelligent modules. Typically a power supply module may integrate such communication bridge.
- Supporting modules may exceptionally come without communication interface at all, such as low-cost power supplies and battery backups.

For its operation a SIB based system requires at least one module belonging to the intelligent class, a power supply, and optionally a bridge providing a connection to PC.

SIB specifies hardware minimalistic communication and power interface for modules, as shown in Figure 1. GLB, LBR and LBL represent communication channels, marked as GLB0, GLB1, or GVL0p/GVL0n when paired in differential mode and using high-speed LVDS. The I2C and GLB0/UART represent the primary communication interface and multi-master access to each device configuration. Fast communication with adjacent modules is achieved via local interfaces LBL and LBR. All signal connections on LBL, LBR and GLB are allowed to pass digital and analogue signals.

POWER up to 24 V and 0 V power signals, up to 3 A
I2C I2C based communication interface
GLB/GVB Global Bus, where pairs can form a LVDS link for very high speed communication
LBR/LVR Local Bus to adjacent module on the right, where pairs can form a LVDS link
LBL/LVL Local Bus to adjacent module on the left, where pairs can form a LVDS link

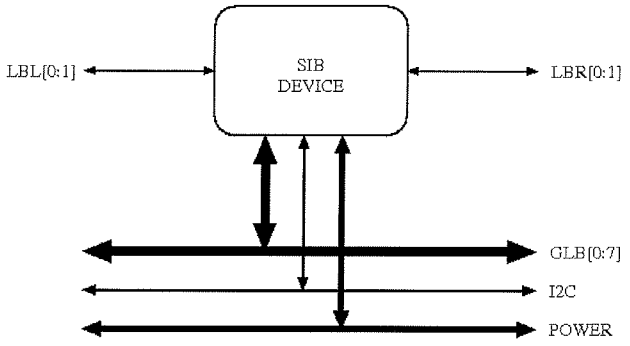

Fig. 1: SIB interface.

3. SIB Protocol Stack

By analogy with Open System Interconnection (OSI) layered architecture /8/ the protocol stack for the proposed instrumentation bus consists of PHY layer (SIB-PHY), medium access layer (SIB-MAC) and message layer (SIB-MSG), the latter encompassing all required functionalities above MAC layer. The proposed layered structure is depicted in Figure 2.

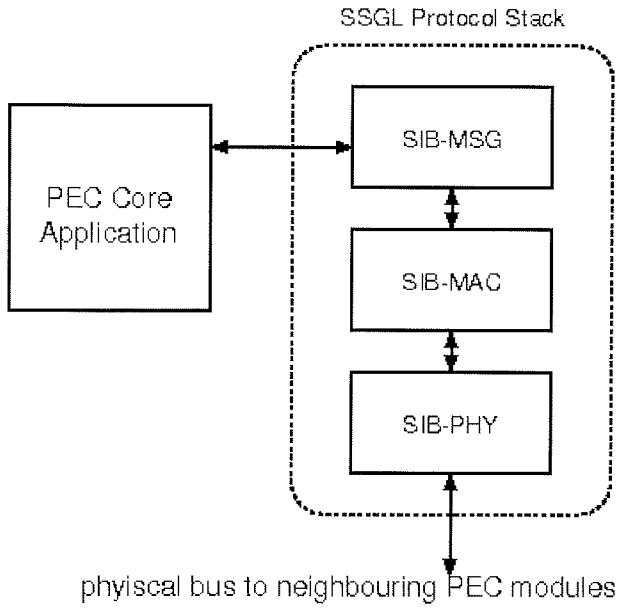

Fig. 2: SIB protocol stack implemented in PEC modules.

3.1 SIB-PHY Layer

SIB-PHY interface implemented in PEC modules only contains five signals that provide connection to left and right modules via two left and right four-pin connectors. These signals include:

- Power signal +24 V to left and right modules.
- Return or GND (0 V) to left and right modules.
- Global communication bus GLB0 to left and right modules.
- Local communication bus LBR0 to right module only.
- Local communication bus LBL0 to left module only.

Communication on the global bus needs to be fail-safe. This means that permanent malfunction of a module should not terminate communication on GLB0. Communication is half-duplex and has multi-master topology where up to 32 devices may be attached to a single GLB0 bus, this limitation being a consequence of power constraints and physical length of the bus.

Physical signalling is based on standard UART interface. With respect to the UART specifications, frame arbitration signalling is added to SIB-PHY, defining basic packet frame or time-slot.

Standard UART low-level framing protocol transfers data on byte basis (similar to linbus /6/) and is configured in 8 bit data mode with odd parity and one stop bit. SIB-PHY adds start of frame and end of frame signals making it suitable for multi-master environments and automatic data rate detection. SIB-PHY UART physical framing is shown in Figure **Error! Reference source not found.** and consist of:

1. Start of Frame (HIGH state) denoting Bus Request. If LOW is detect on the bus prior to step 2, bus is lost, or if HIGH is detected prior asserting logic HIGH, bus is busy. Start of Frame has length of 10 bits (8 HIGH bits + HIGH odd parity bit + one stop bit) and implies the bit rate.
2. Start of Byte (LOW state) begins standard UART transmission of a byte with logic LOW start bit.
3. Individual bits (LOW/HIGH state): the 8 data bits, odd parity.
4. End of Byte (HIGH state): 1 stop bit. *When more bytes are to be sent, repeat from step 2.*
5. End of Frame (LOW state). *When more messages are to be sent, repeat from step 1.*

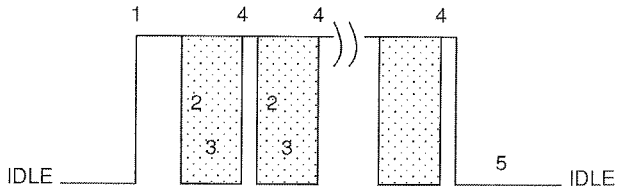

Fig. 3: SIB-PHY UART signalling.

Such physical framing can be implemented by any UART interface found in contemporary microcontrollers (MCUs). The most important properties of such signalling scheme are as follows:

- Transfer is half-duplex, multi-master with frame arbitration and automatic bit-rate detection.
- Bus collision is detected by monitoring (receiving) bytes back from GLB0 during the transmission and also by checking the parity bits.
- Frame length error is detected by standard UART Frame Error Detection mechanism (for instance by BREAK signal, which is generated in this case).
- Typical UARTs in MCUs support a broad selection of bit rates in the range from kbit/s up to Mbit/s.

3.2 SIB-MAC Layer

The SIB-MAC layer defines simple but powerful and low-overhead communication protocol stack. It has been designed to meet requirements of the next generation distributed communications and data processing devices. Being based on SSGL, which was originally developed for sensor networks, its main features include:

- PHY independency at variable data rates.
- Innovative peer-to-peer and broadcast bi-directional pipe.
- Bandwidth allocation with the first order allocation predictor.
- Synchronisation mechanism.
- Acknowledged protocol for transfer reliability.
- Support for low power and power down modes.
- Support for self-management and self-healing of devices.

- Support for redundant systems.
- Ultra-low packet overhead.
- Independency from the device intelligence level.

Full implementation of the SSGL-MAC layer supports standard star and peer-to-peer (full mesh) topologies. It additionally supports a combination of standard peer-to-peer and broadcast modes, simplifying the architecture of redundant and high-availability systems. The last type of connection is named as SSGL-MAC general pipe. For the operation, network does not require any coordinator, making the system very robust.

SSGL-MAC introduces the term pipe on the peer level, which defines transaction between two devices. The SSGL-MAC pipe enables a device to communicate with one peer, forming peer-to-peer connection, and at the same time allowing (or not) others to interrogate into their conversation. More intelligent devices can influence pipe properties, they can recommend better channel and require reduction of the bandwidth. In such a way, pipes can be managed and controlled by other entities without being dependent on them.

SIB only requires the most basic implementation of the SSGL-MAC supporting:

- Totally stripped message header containing only ID and CRC.
- One broadcast pipe and one receive pipe.
- Reception of other responses (messages).
- Internally time-driven broadcast pipe in order to limit maximum bandwidth occupation.
- Data fragmentation to support transfer of long messages.

The SIB-MAC frame consisting of three fields is shown in Figure 4. It can be up to 256 Bytes long. The *Device ID* field (4 Bytes) uniquely defines the device within the array, the *Data* field (0 t 250 Bytes) holds data formatted according to the SIB-MSG layer specification, and the *CRC field* (2 Byte) provides the final checksum.

Preamble	Device ID	Data	CRC	*Ending*
start of frame	4	0-250	2	end of frame

Fig. 4: SIB-MAC frame structure.

SIB devices support only two pipes operating at the same time:

- Broadcast Pipe broadcasts internal information of the device as declared by internal time-slot timer and is capable of receiving responses that are sent by other devices immediately after its transmission. This is the default pipe opened by every device.
- Receive Pipe selectively receives other broadcast messages and responds to the same device. This pipe is opened by the responding device in case there is a message that needs to be transferred only to a specific device with a given ID.

Low level transaction and framing is defined by SIB-PHY layer, however, MAC protocol takes care that sufficient time is left after the broadcast message is sent for safe transmission of responses.

3.3 SIB-MSG Layer

SSGL-MSG layer is designed as a light-weight self-describing protocol so as to suit to simple and advanced devices with minimum data and program memory requirements. Data is carried in the format of a message, which does not require converting the numbers into strings and can carry also structured expressions and powerful equations, including vectors and matrices. Furthermore, such format does not require extensive parsing (such as in the case of XML) by each device as it shifts all the complex arithmetic and logic to the typically more processing powerful devices which are designated to interpret given information. Variable-value pair binding requires only basic parsing, which is manageable also by most simple devices.

The general structure of the SSGL-MSG layer message is shown in Figure 5. It consists of constant (description) and dynamic (arguments) parts. Description is transmitted only upon request, if the message with a given ID is unknown to the receiver. Most of the time only arguments that are changing are (re-)transmitted. Fields marked as *mandatory* are present in every message, while fields marked as *optional* are sent on request or upon a change.

DESCRIPTION	TERMINATOR	ID	ARGUMENTS
optional	*mandatory*	*mandatory*	*optional*
t-bytes	1-byte: 0x00	2-bytes	*a*-bytes

Fig. 5: SSGL message structure.

The constant part of the message is formatted in a similar way as the standard C *printf()* function. It defines how message is to be shown or represented along with its arguments to a human using the following formatting syntax:

- Expressions to support high-level math operations in format *{expr}*.
- Variable-value pair binding with (tolerance) range and multi-dimensional unit support *{:variable}={expr+-tolerance}/unit/*.
- Local and global variables, and cross-referencing: *{:*global}, {:local}*.
- Data structures and unions: *{:struct.substruct.token}, struct{...}*.
- Text formatting, headers, tabular environment, enumerations, lists and buttons.

Each message is an autonomous cell. Multiple messages form larger structures and hence complex contents. Therefore it is required from the MAC to transfer each message as an autonomous cell even if fragmented to smaller pieces.

Each device with SSGL-MSG layer must implement at least two messages:

- INIT MSG - Initialization Message, which has assigned message ID 0. It defines the initial content of a device with unique textual description in human understandable form. This message is typically transferred only once.
- STATUS MSG - Status Message, which has assigned message ID 1. This message describes the current status of a device. In PEC modules, for instance, these include the present power and energy consumption, and the output states.

With respect to SSGL-MSG layer the SIB-MSG layer implementation as required in PEC units is considerably stripped down as it only needs to support the following features for its operation:

- Transmission of constant part of the message.
- Transmission of variable part of the message.
- Handling of local requests for message transmission.
- Handling of remote requests for message transmission.
- Handling of remote requests for message variable update.

The term *local request* refers to operations within MCU, while the term *remote request* refers to all operations sent by other(s) and received via MAC layer.

4. Power and Energy Control Modules

Power and Energy Control modules are compact autonomous units that monitor and control two power electrical branches at a time. They are designed to be placed in a standard (DIN) electric installation housing next to fuses, thus forming a cluster of distributed sensors and actuators. Connection between modules is achieved using contacts placed on the left and the right side of the module 4-pin connector. For the operation they require one (or more for redundancy) power supply unit(s). Typically power supply unit also features a bridge circuit to connect clusters into a larger monitoring and control network. The same interface also provides the access to the user. PEC module as described above is depicted in Figure 6.

A PEC module consists of:

- Isolated current sensor and switch power interface.
- SIB communication interfaces.
- 8-bit Atmel AVR MCU with the SIB protocol stack.
- PEC core application.

In order to prove the concept of SIB instrumentation bus and protocol stack in PEC units we implemented the following devices:

- SIB Bridge Interface that links a PC with PEC units.
- SIB Device Monitor software package in the form of a browser with Contents Viewer capable of high-level presentation of PEC messages and data structures with data input support to write back controllable variables.

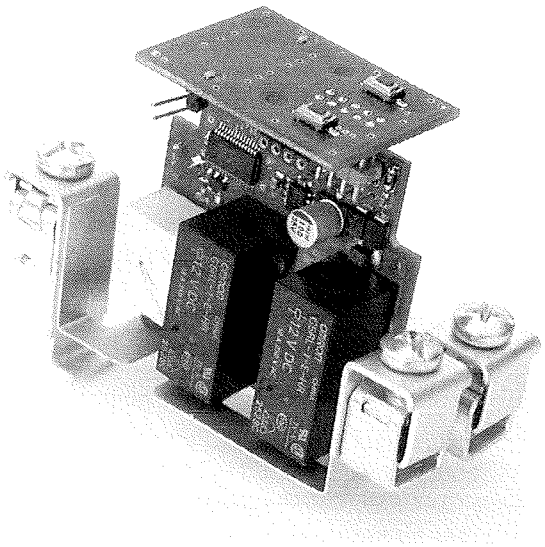

Fig. 6: PEC module implementation.

Description (or constant part of the message) is typically transmitted upon remote requests only until it is known to the receiving device. Description length is typically much longer than the maximum message size, so data is fragmented by SIB-MAC layer into smaller fragments and sent individually. SIB-MAC layer uses fragment counter and start and end of fragment bits to correctly assemble received fragments in the message.

During its operation a PEC unit continuously updates variables in the data structure, which is directly mapped to the variable part of the messages. The application can also issue a local request for (re-)transmission of the message with ID, which has updated variable part of the message. Only variable part of the message is sent with complete message length typically equal to 7 bytes.

By gathering all of the message descriptions along with variables the presentation software builds an HTML page for the PEC device.

In the same way as variables are transmitted from the device, they can be sent back to the device as an input. Using the same ID and message structure, a message is sent using a reply mechanism of the MAC layer (using receive pipe) and received as other response by receiving device. MAC layer passes valid messages to the Message layer and validates input argument(s).

The presentation software uses the same equations that are used in formatting messages into HTML format in reverse direction by computing inverse. Presently supported numerical method is 1-dimensional Newton's method

capable of computing an arbitrary function of a single argument: $x = f^{-1}(y)$.

The graphical user interface of the SIB Device Monitor is shown in Figure 7. It lists all available devices with the first two messages: Initialization (INIT MSG) and Status (STATUS MSG) messages. A mouse click on a device invokes Contents Viewer as depicted in Figure 8, showing:

- Formatted message contents in HTML format on the right side of the figure.
- A list of variables with present values on the left side of the figure. A mouse click on a variable invokes input method for a given type (string, number, list / enumeration, etc.).
- Additional views on the left side of the figure are Message Contents, showing headings sorted in a tree, and Raw Messages that can be used as a debugging tool.

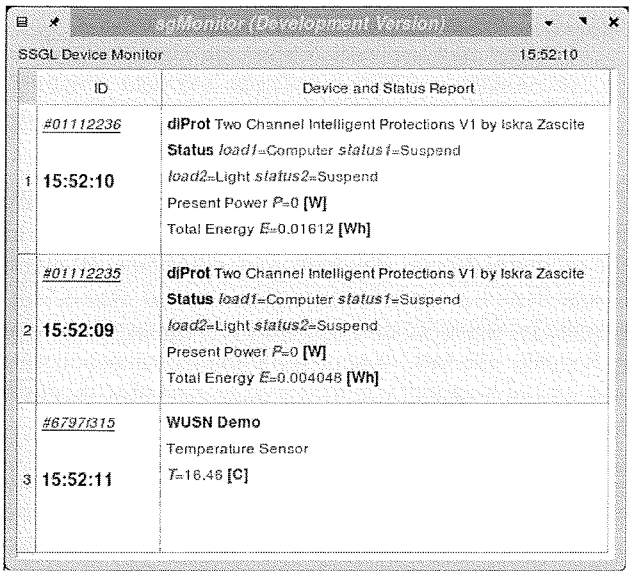

Fig. 7: SSGL Device Monitor.

5. Conclusions and future work

In this paper we described the implementation of the inter-module communication as defined by SIB instrumentation bus and a simplified protocol stack, which was originally defined by SSGL specifications for sensor networks. As a show case we applied the SIB instrumentation bus in power and energy management system consisting of PEC modules. Using the proposed SIB architecture two or more PEC modules can be arranged in an array forming a cluster of instrumentation and control devices with the following major benefits:

- Each PEC module (or SIB module) operates as an autonomous cell providing independency from other modules and consequently higher availability of the entire system compared to centralised architectures.
- SIB protocol stack supports fault-tolerant, multi-master half-duplex communication with collision detection, implemented using standard UART interface and innovative MAC layer broadcast/receiving pipe concepts.
- Being designed as a light-weight protocol it releases CPU from high processing requirements, which is particularly important for low-cost 8-bit devices while operating at high communication speed (Mbit/s).
- Self-describing message formats are featuring rich text formatting and expression post-processing capabilities with (user) feedback input, thus guaranteeing future upgradability and compatibility.
- Presentation software generates standard HTML output, viewable in a browser on any PC, handheld or mobile phone.
- SIB represents a compact solution at low manufacturing costs.

While in this paper demonstrated on PEC modules, the proposed SIB specification can be used for general purpose instrumentation, such as I/O units, power supplies, current and voltage meters, etc. In this respect we are planning to release the SIB specifications for general use and also provide software support library for data acquisition and control.

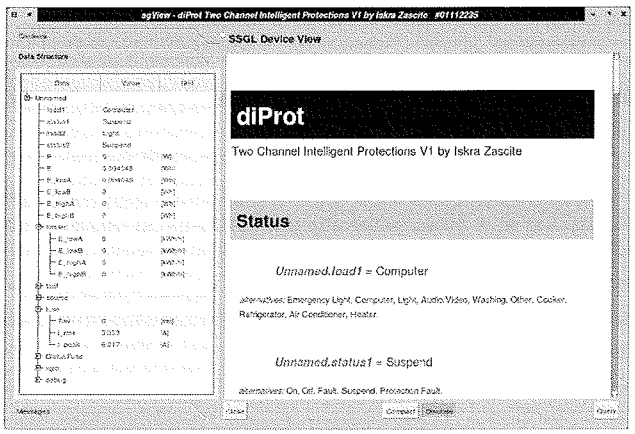

Fig. 8: SSGL Device View.

On the other hand, PEC modules can be integrated in a telemetry and telecontrol system for efficient and reliable remote management of an electric power distribution system, possibly making use of professional wireless communications technology such as TETRA (TErrestrial Trunked RAdio) /9, 10/.

Acknowledgement

The instrumentation bus technology and PEC modules were developed by Iskra Zaščite Ltd. and Insitut "Jožef Stefan".

References

/1/ ZigBee Alliance, http://www.zigbee.org

/2/ Echelon Corporation, http://www.echelon.com

/3/ Siemens Corporation, http:///www.siemens.com

/4/ The Industrial Communications Community, http://www.profibus.com

/5/ Modbus IDA, http://www.modbus.org

/6/ LIN SubBus, http://www.lin-subbus.org/

/7/ Sensor Standard General Language, http://sensornet.ijs.si/ssgl_whitepaper.html

/8/ H. Zimmerman, "OSI Reference Model. The ISO Model of Architecture for Open Systems Connection", IEEE Transactions on Communications, Vol. Com-28, No. 4, April 1980.

/9/ M. Smolnikar, A. Hrovat, M. Mohorčič, I. Ozimek, T. Celcer, G. Kandus, "Telemetry and telecontrol over TETRA network", Inf. MIDEM, 2008, vol. 38, no. 1, pp. 61-68.

/10/ I. Ozimek, T. Javornik, G. Kandus, M. Švajger, "Using TETRA for remote control, supervision and electricity metering in an electric power distribution system", WSEAS trans. commun., 2008, vol. 7, no. 4, pp. 289-299.

Uroš Platiše and Mihael Mohorčič
Institut "Jožef Stefan", Ljubljana, Slovenija

Prispelo (Arrived): 22.07.2009 *Sprejeto (Accepted): 09.03.2010*

MAGNETIC MICROSYSTEMS FOR POSITION MEASUREMENT

Blaž Šmid

University of Ljubljana, Faculty of electrical Engineering, Ljubljana, Slovenia

Key words: magnetic microsystem, Hall sensor, angle measurement, linearization algorithm, distance measurement

Abstract: Position measuring devices are used in numerous fields in everyday life. Automobile industry uses them for detecting the throttle position, steering wheel position, clutch position, ignition key position, etc. Home appliances like washing machines use them for measuring the rotation and axis displacement of the drum. Basically every movement in a device that determines its operation needs to be measured more or less accurately.

Magnetic microsystems that measure position are a good alternative to older mechanical solutions. A magnetic microsystem usually consists only of an ASIC (application specific integrated circuit) and a permanent magnet. The setup is simple and requires no mechanical contacts or switches. The whole setup is usually relatively small and cheap.

In the paper several solutions for measuring the position with magnetic microsystems are presented. The mathematical model is built for each. Some solutions are already integrated in ASICs that are used in the industry.

Magnetni mikrosistemi za merjenje absolutne pozicije

Kjučne besede: magnetni mikrosistem, Hall-ov senzor, merjenje kota, algoritem linearizacije, merjenje razdalje

Izvleček: Naprave za merjenje pozicije se uporabljajo v vsakdanjem življenju na različnih področjih. Avtomobilska industrija jih uporablja pri določanju položaja stopalke za plin, sklopke, pri določanju kota krmila in zagonskega ključa, itd. V gospodinjskih aparatih, na primer v pralnem stroju, so merilne naprave uporabljene za merjenje obratov in gibanja bobna. V bistvu vsak premik, ki določa delovanje naprave, mora biti izmerjen bolj ali manj točno.

Magnetni mikrosistemi za merjenje pozicije so lahko dobra alternativa starejšim mehanskim rešitvam. Magnetni mikrosistem ponavadi sestavljata integrirano vezje in trajni magnet. Sestav je enostaven in ne zahteva mehanskih kontaktov ali stikal. Je razmeroma majhen in poceni.

V prispevku je prikazanih nekaj rešitev za merjenje pozicije z magnetnimi mikrosistemi. Za vsako rešitev je razvit matematični model in nekatere so že vgrajene v integrirana vezja in uporabljene v industriji.

1. Introduction

The basic function of magnetic microsystems is to measure magnetic field. The magnetic field is generated by a permanent magnet that is located in the proximity of an integrated circuit (ASIC). That means that the microsystem consists only of an integrated circuit and permanent magnet. In some setups more magnets are used.

The permanent magnets are of different shapes and sizes. Also the magnetization direction and strength varies from one type of position measuring magnetic microsystem to another. The magnet changes its position relative to the integrated circuit which means that the magnetic field strength changes at the position of the integrated circuit.

The position can be measured absolutely or relatively. If the magnetic field is generated by multiple permanent magnets and is periodic over a certain span of distance, the position is measured relatively. That means that the given information from the ASIC about the distance is relative. If the magnetic field is not a periodic function and the position is measured absolutely, one value of the magnetic field strength in the position of the ASIC corresponds to only one value at the output. In practice the difference between these two cases is that when the position is measured relatively, the reference position has to be known or it may not be relevant at all.

The integrated circuits embedded in the magnetic microsystems measure the magnetic field with integrated Hall element (elements). Many different approaches for integrated Hall element signal processing are published in /3/ and /4/, providing a solid basis for different algorithm implementation. Hall element senses only the perpendicular component of the magnetic field strength vector which means that only one dimension of permanent magnet movement can be measured. In some cases it is beneficial to use more Hall elements that are positioned perpendicular to each other. That way two or three components of the magnetic field strength vector are measured. This gives more information about the magnetic field. One component of the magnetic field strength can determine the position over one part of the measuring range and the other component can determine the position over the other part of the measuring range, and that can increase the measuring resolution or increase the position measuring range. Also more components of the magnetic field strength vector mean that position can be measured in two or three dimensions.

In the paper three different magnetic microsystems are described:

- magnetic microsystem for absolute angle measurement
- magnetic microsystem for absolute distance measurement

- magnetic microsystem for accurate position measurement

Each of them is comprised of a permanent magnet and the ASIC. All measure one dimension of permanent magnet movement relative to the integrated circuit. The first microsystem gives information about the rotation of the permanent magnet, second about the distance between the permanent magnet and the ASIC and the third measures the position of the permanent magnet that moves parallel to the ASIC. For all three systems signal processing ASICs are designed with methodologies for mixed signal design /1/, /8/ and optimization technologies /7/.

2. Absolute angle measurement magnetic microsystem

The microsystem is comprised of the permanent magnet and the ASIC (Figure 1). The permanent magnet is diametrically magnetized. The ASIC measures the perpendicular component of the magnetic field strength vector and gives the information about the absolute rotational angle of the permanent magnet above the ASIC.

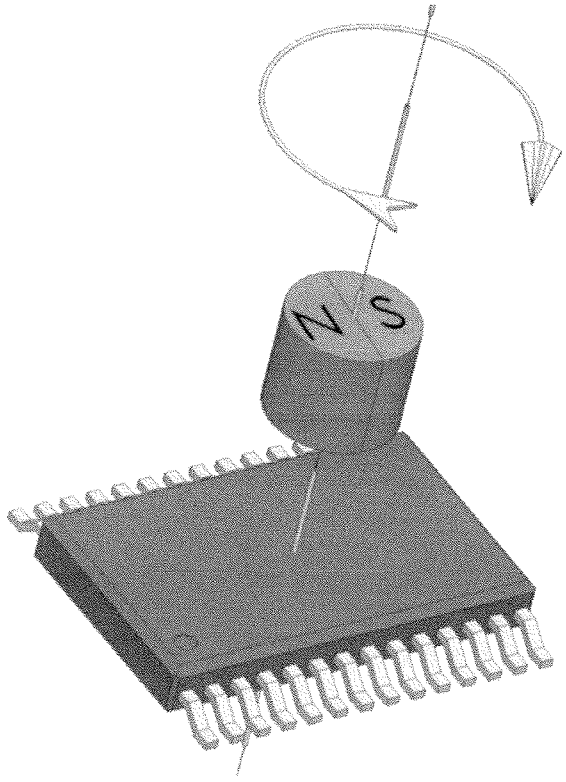

Fig. 1: Magnetic microsystem for absolute angle measurement

2.1 Angle measurement principle

There are sixty four Hall elements integrated in the ASIC. They are positioned in a circle. The axis of the circle coincides with the rotational axis of the permanent magnet. For clearer principle presentation only eight Hall elements are shown in Figure 2. This can be easily generalized into the case with sixty four Hall elements.

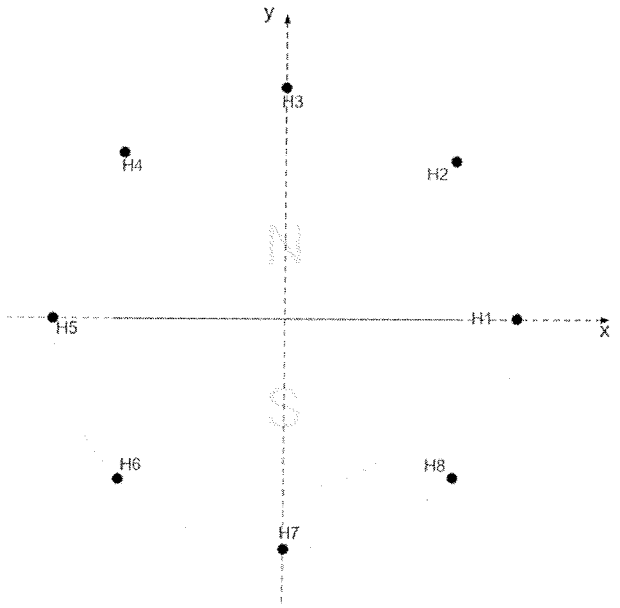

Fig. 2: Eight Hall elements placed in a circle

By rotating the permanent magnet above the ASIC, the perpendicular component of the magnetic field strength to every Hall element describes a sine shaped signal. That means that eight (sixty four) sine signals are the result of one permanent magnet turn. The ASIC has two output signals. A sine signal and a cosine signal. They are a derivative of all eight (sixty four) sine signals that come directly from the Hall elements and are calculated as shown in (1) and (2).

$$sine = S1 + S2 + S3 + S4 - S5 - S6 - S7 - S8 \quad (1)$$

$$cosine = S3 + S4 + S5 + S6 - S7 - S8 - S1 - S2 \quad (2)$$

The angle is calculated as shown in (3).

$$\alpha = arctan\frac{sin\,\alpha}{cos\,\alpha} \quad (3)$$

The used principle is very beneficial and robust. Any external homogenous magnetic field that is added to the magnetic field generated by the permanent magnet is eliminated. This comes from (1) and (2). Also the sensitivity of Hall element is a process parameter. If the sensitivity changes from one ASIC to the other the sensitivity changes for all Hall elements on one ASIC and sine and cosine signals are amplified. According to (3) the angle remains unchanged.

2.2 Microsystem characterization

The principle is implemented in the integrated circuit. Special care was paid to front end signal processing design / 2/, low noise input amplifier /5/ and to Hall element modeling /6/. The microsystem is composed of a permanent magnet sized 3-6mm x 3-6mm and diametrically magnetized and the ASIC in one of the standard packages. The

distance between the magnet and the ASIC is variable from 0.5mm to 5mm.

2.2.1 Angle error

The setup allows an accurate absolute angle setting. The angle is set from -21° to 21° with a step of 1°. The angle is calculated from output sine and cosine voltage. The error is then calculated as the difference between manually set angle and calculated angle from output sine and cosine voltage. Figure 3 shows the angle error in angular degrees which is approximately ±0.04 degrees.

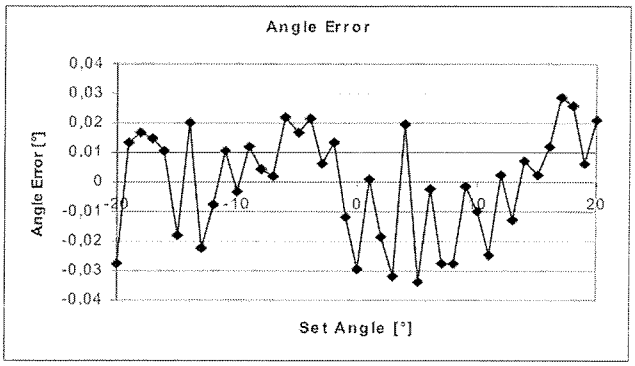

Fig. 3: Angle error

2.2.2 Noise

The resolution of the measurement is limited by the noise. One thousand samples are measured at a randomly set angle. Figure 4 shows the noise in angular degrees. The peak to peak angle noise is 0.015 degrees, the RMS value is 0.065 degrees, and standard deviation is 0.0021 degrees.

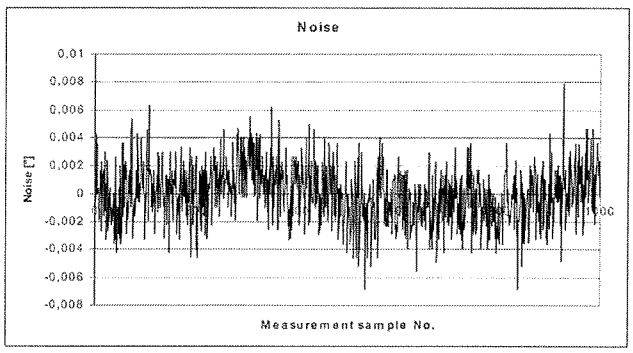

Fig. 4: Noise measurements

2.2.3 Angle depending on the temperature

The angle calculated from sine and cosine voltage is measured at temperatures from -40°C to 100°C with a step of 10°C. A random angle is set. Figure 5 shows the angle depending on the temperature which is approximately 0.001 angular degrees per Kelvin.

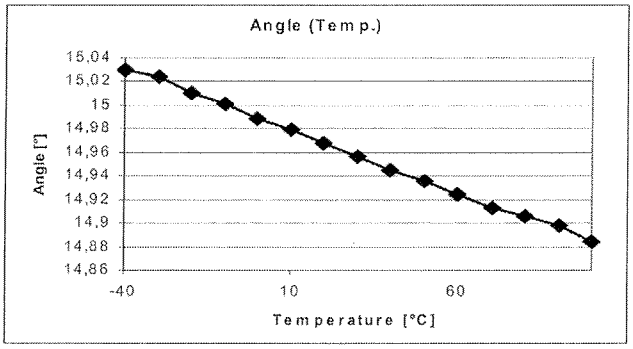

Fig. 5: Angle depending on the temperature

3. Magnetic microsystem for absolute distance measurement

The main idea of accurately measuring the distance is to measure the magnetic field strength in the position of the ASIC which is caused by a permanent magnet placed close to the ASIC (Figure 6). The distance between the ASIC and the permanent magnet varies and it is limited to the maximum distance which depends on signal to noise ratio, offset and sensitivity of the ASIC. While the magnetic field strength is inversely proportional to the distance and is nonlinear with distance, the output of the ASIC should be linear. To solve the problem of nonlinearity a linearization algorithm is developed using the piecewise linear approach.

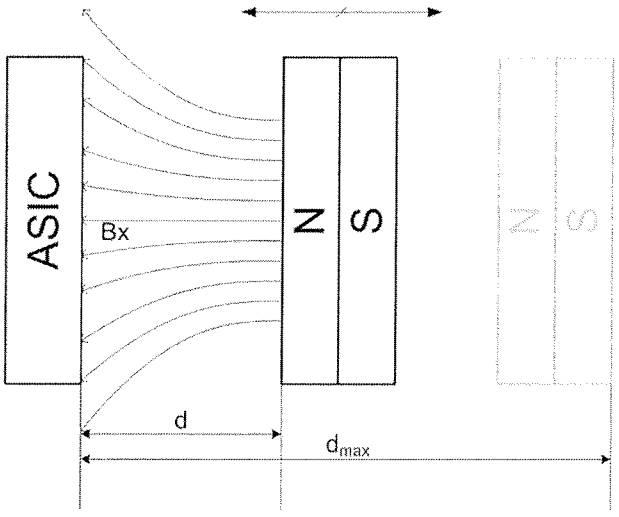

Fig. 6: Magnetic microsystem for absolute distance measurement

3.1 Linearization algorithm

The perpendicular (to the ASIC) component of the magnetic field strength vector is measured with Hall sensor at distances between permanent magnet and the probe varying from 22 to 12 millimeters. The correlation between magnetic field and the output voltage of the ideal Hall element is linear.

For the analysis the maximum distance is selected as a reference point since the magnetic field at maximum distance is the weakest. Figure 7 shows the measured (scaled) values and the ideal linear output voltage.

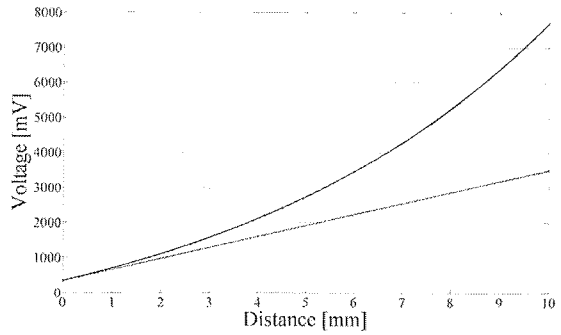

Fig. 7: Input (scaled) and output voltage

The distance range is divided into 20 segments called linearization points. At each linearization point the gain decreases so the signal at that point becomes equal to the desired output voltage. The result is a saw-tooth shaped signal with large error. The saw-tooth shaped signal and the ideal output voltage is shown in Figure 8.

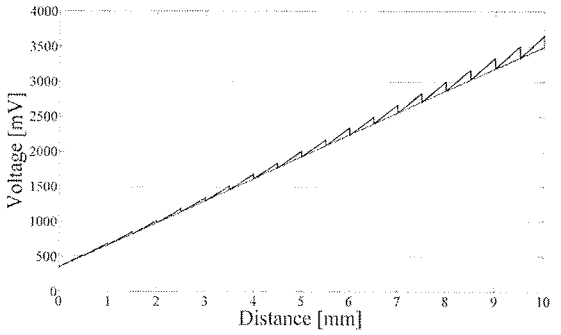

Fig. 8: Saw-tooth shaped and ideal output voltage

The resulting signal still has a large error. Additional smoothing procedure is implemented in the linearization algorithm. The gain between linearization points is calculated as a linear interpolation of two neighboring linearization points.

Theoretically the magnetic field strength is inversely proportional to the distance (1/x). The relation between magnetic field strength and output voltage of the Hall element is linear and the gain at linearization points can be adjusted infinitely accurate. In this case the overall error after linearization is zero. In the real environment the Hall element is not linear, the data are measured and the gain cannot be accurately set because only finite gain steps are available. These factors contribute to the resulting linearized output voltage with an error. The linearized output signal error in percentage is shown in Figure 9.

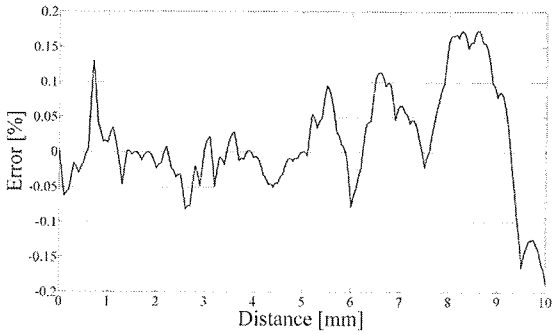

Fig. 9: Output error

3.2 Microsystem linearization characterization

The linearization algorithm and Hall element with corresponding electronics is implemented in the integrated circuit. The distance from ASIC to permanent magnet varied from 22 to 12 millimeters. The input nonlinear voltage curve is linearized from 0.35 V to 3.5V. Also 20 linearization points are used, the same as in the mathematical linearization. Figure 10 shows the linearized output voltage and Figure 11 shows the overall error in percentage.

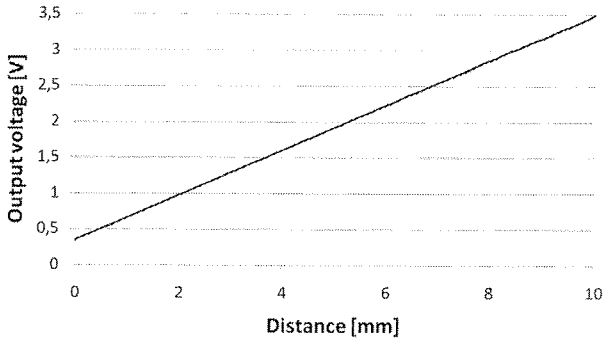

Fig. 10: Measured linearized output voltage

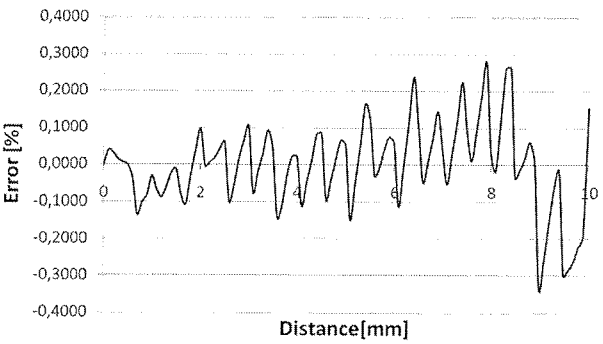

Fig. 11: Overall linearization error of the measured linearized output voltage

4. Magnetic microsystem for accurate position measurement

The magnetic microsystem is composed of a permanent magnet and two integrated circuits. The main integrated circuit contains all the circuitry including the algorithm realization and Hall sensor. The additional integrated circuit is simpler since it contains only a Hall sensor and some elements needed by Hall sensor, such as amplifiers, etc.

In Figure 12 the setup is shown. The Hall sensor of the main integrated circuit is positioned in the centre of the Cartesian coordinate system. The additional integrated circuit is positioned away from the main integrated circuit so the Hall sensor is at the point with coordinates x=0mm, y=-1mm and z=3mm.

The Hall sensor in the main circuit is set horizontally, therefore it is sensitive to vertical component (By) of the vector of magnetic field density. In contrast the Hall sensor in the additional integrated circuit is set vertically and is sensitive to the horizontal component (Bx) of the vector of magnetic field density.

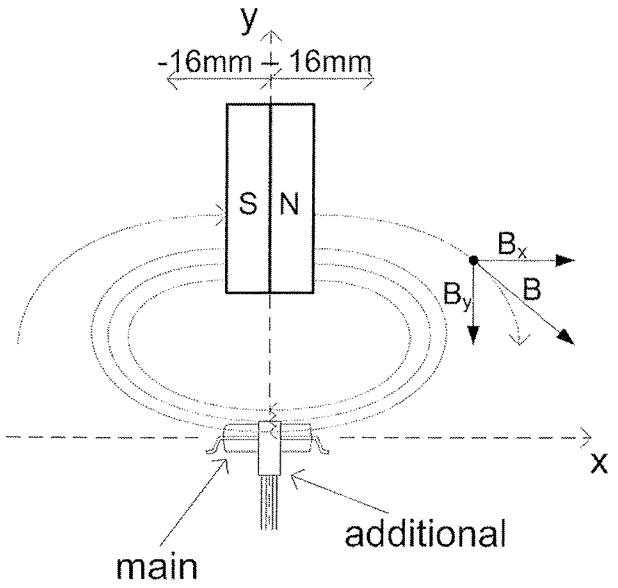

Fig. 12: Magnetic microsystem setup

In order to perform further analysis and linearization, both vertical and horizontal components are measured from x=0 millimetres to the position of x=16 millimetres. Since the measured components are symmetrical over the y axis the other half of measurements are not necessary. The measurements are presented in Figure 13. The full line presents the vertical component of magnetic field density vector and the dashed line presents the horizontal component of the magnetic field density.

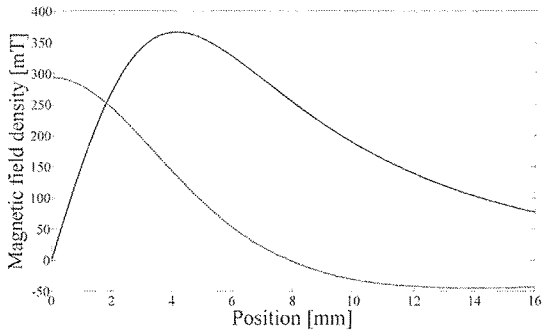

Fig. 13: Vertical and horizontal component measurement

4.1 Idea of electronic realization of linearization

Before the algorithm is designed, some basics need to be known concerning the electronic realization.

In Figure 14 the idea of electronic realization of the algorithm is presented. With properly calculated resistors, the coefficients are set and the comparators are switching linearly according to the position. The linearization is therefore discrete and there are as many steps as the number of comparators.

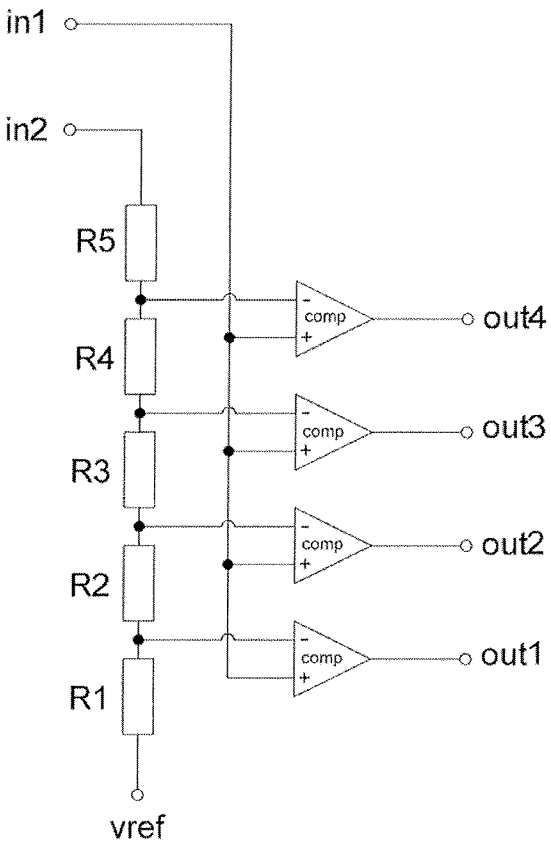

Fig. 14: The idea of electronic realization

The requirement of such realization is that the input signal on the resistor chain needs to have higher voltage values

than the signal on the comparators otherwise the switching would not occur.

Another requirement is that the ratio between the signal on the resistor chain and the signal on the comparators must be a rising or a falling function or in other words the derivative of the ratio must not change its sign. Therefore the signal from the vertical Hall sensor is inverted from the point where it reaches its minimum.

The signals are divided into three distance regions. One distance region is from the position 0 millimetres to the position where the two signals meet. Second region is from the end of the first region to the point where the lower signal reaches its minimum. The third region is from the end of the second region to the 16 millimetres. Figure 15 shows the two signals prepared for the linearization algorithm.

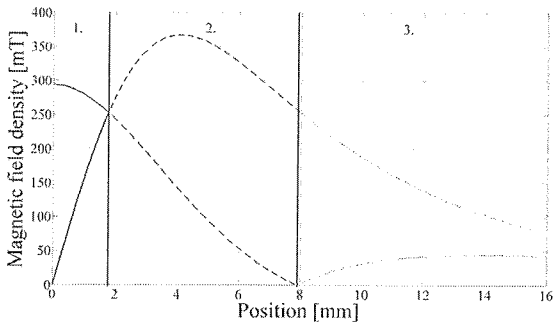

Fig. 15: Signals divided into three regions

4.2 Linearization results of mathematical model

The two signals are divided into three distance regions that are further divided into more segments. 45 segments are selected for all three distance regions together. At every segment the output changes it value for one step. The ratios of two signals are calculated at segments and also the resistor values are calculated which are later used in electronic realization. If the ratios are calculated correctly, the output is changing its value linearly versus the position of the magnet.

Figure 16 shows the results. A step function is the output of the algorithm and the linear function is a linear interpolation of the output function so the linearity of the output is more evident. The y axis shows the output level number and as the figure shows there are 45 steps for a range of 16 millimetres.

4.3 Electronic realization of the algorithm and simulation results

According to the idea of the electronic realization and resistors values calculated mathematically, an electronic realization of the algorithm is designed.

Three separate resistor chains with comparators are

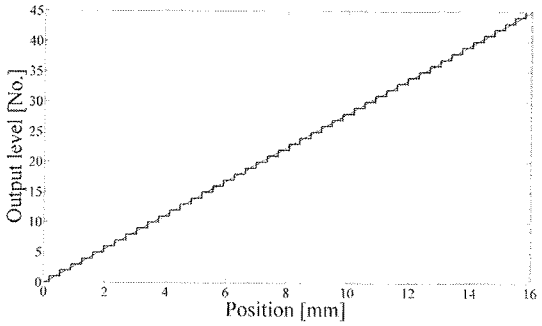

Fig. 16: The output of the mathematical algorithm

formed. First block has 5 comparators, thus it covers 5 steps of the first of three segments of a whole position range. Second block has 17 comparator and the third block has 23 comparators, all together 45 comparators.

On each out of 45 segments one comparator changes its state from 0 to 5 volts (the supply voltage) and enables the transistor switch. The transistor then adds current to the output resistor and the voltage on the resistor rises.

Figure 17 shows the first block with resistor chain, comparators, etc. There is some additional logic added so the first block functions only in the first segment. That is from the 0 millimetre to the position where the signals meet. The outputs are then connected to the cell with transistor switches which add the current to the output resistor.

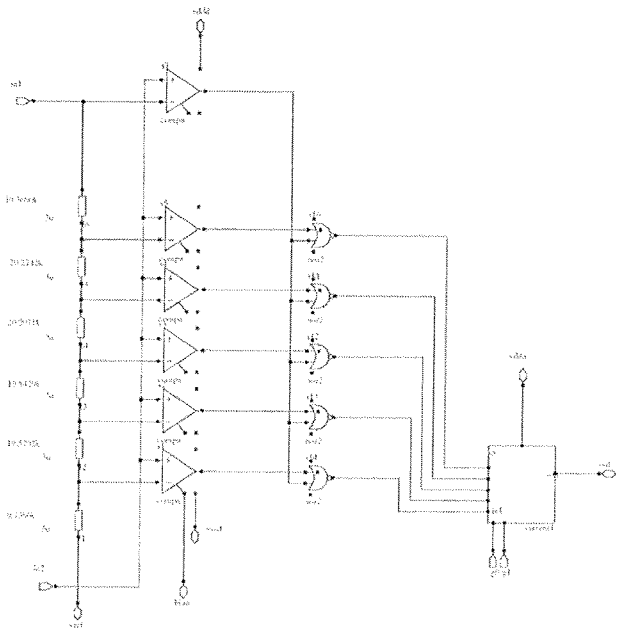

Fig. 17: First linearization block

The other two blocks used for second and third segment are similar to the first block. All three blocks together cover only half of the position span, that is 0 millimetre to 16 millimetre.

The goal is to cover 32 millimetre span, from -16 millimetres to 16 millimetres according to Fig. 12. Since the hor-

izontal component of the magnetic field strength is symmetrical and vertical component is inversely symmetrical, only the vertical component has to be inverted for the other half of the position span. Also the output is inverted in the other half of the position.

Simulation results are shown in Figure 18. The upper part of the Figure shows two inputs and the bottom part shows the output of the algorithm.

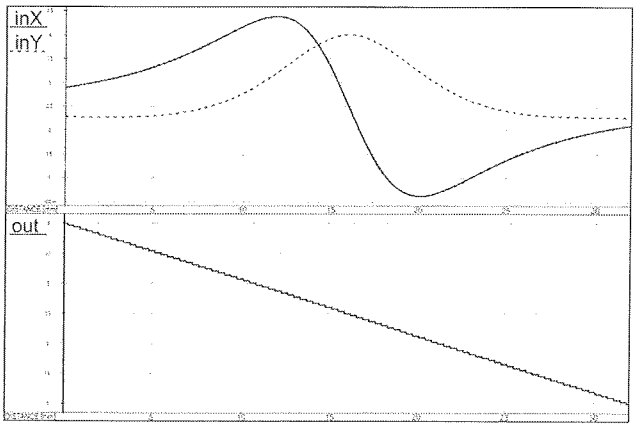

Fig. 18: Simulation results

5. Conclusion

Three different magnetic microsystems are presented in the paper. One is for absolute angle measurement, second for absolute distance measurement and the third for absolute position measurement. All of them are verified with mathematical analysis; the ASICs for all three are designed and verified with accurate simulations tools. Two of them are realized, fully characterized and released to production. Some of the characterization results are presented in the paper.

6. References

/1/ TRONTELJ, Janez. Trends in mixed signal ASIC design. Inf. MIDEM, vol. 24, št. 4(72), str. 221-226, 1994

/2/ TRONTELJ, Janez. Integrated Hall sensor array electronics. Inf. MIDEM, let. 28, št. 2(86), str. 95-101, 1998

/3/ TRONTELJ, Janez. Smart integrated magnetic sensor cell. Inf. MIDEM, let. 29, št. 3, str. 126-128, 1999

/4/ TRONTELJ, Janez. Integrated magnetic sensors design examples. Inf. MIDEM, let. 29, št. 4, str. 190-194, 1999

/5/ TRONTELJ, Janez, SEŠEK, Aleksander. Ultra low noise PAGC amplifier for microsystem sensor signal processing. Inf. MIDEM, letn. 35, št. 1, str. 8-12, 2005

/6/ SEŠEK, Aleksander, TRONTELJ, Janez. A new model for six terminal Hall element. Inf. MIDEM, letn. 37, št. 2, str. 61-66, 2007

/7/ TRONTELJ, Janez. Optimization of integrated magnetic sensor by mixed signal processing. Proceedings of the 16th IEEE Instrumentation and Measurement Technology Conference, Venice, Italy, vol. 1, str. 299-302, 1999

/8/ TRONTELJ, Janez, TRONTELJ, Lojze, SHENTON, Graham. Analog digital ASIC design. London [etc.]: McGraw-Hill Book Company, XVI, 249 str., 1989

Blaž Šmid, univ. dipl. ing. el.
Univerza v Ljubljani, Fakulteta za elektrotehniko
Tržaška 25, SI-1000 Ljubljana
E-mail: blaz.smid@fe.uni-lj.si
Telefon: (01) 4768 - 340

Prispelo (Arrived): 09.12.2009 *Sprejeto (Accepted): 09.03.2010*

ON THE FUNCTIONALIZATION OF POLYPROPYLENE WITH CF_4 PLASMA CREATED IN CAPACITIVELY COUPLED RF DISCHARGE

A. Vesel, M. Mozetic

Plasma Laboratory, Jozef Stefan Institute, Ljubljana, Slovenia

Key words: Plasma, tetraflourmethane, plasma functionalization, sputtering, aluminum

Abstract: Hydrophobisation of polypropylene was performed using low pressure weakly ionized plasma of tetrafluormethane at pressure of 1.0 Pa. Plasma was created in an aluminum discharge chamber by capacitively coupled RF generator at 13.56 MHz and the forward power of 100 W. The powered electrode was made from aluminum and its area was much smaller than the grounded chamber. The plasma density was about $1\times10^{16}m^{-3}$ and the electron temperature about 3 eV. Samples of polypropylene discs were exposed to plasma for 10 minutes. Before and after the treatment they were analyzed by high-resolution XPS. Apart from the appearance of F-rich functional groups, a few at.% of aluminum was detected on the sample surface after the plasma treatment. The XPS results were explained by weakly etching of the powered electrode during plasma treatment and deposition of sputtered material onto the polymer samples.

Funkcionalizacija polipropilena s CF_4 plazmo ustvarjeni v kapacitivno sklopljeni RF razelektritvi

Kjučne besede: Plazma, tetrafluorometan, plazemska funkcionalizacija, razprševanje, aluminij.

Izvleček: Hidrofobizacijo polipropilena smo izvedli v nizkotlačni šibko ionizirani plazmi iz tetrafluorometana (CF_4) pri tlaku 1,0 Pa. Plazma je bila proizvedena v razelektritveni komori iz aluminija s kapacitivno sklopljenim RF generatorjem pri frekvenci 13,56 MHz in moči 100 W. Elektroda je bila narejena iz aluminija. Njena površina je bila veliko manjša kot površina ozemljene komore. Gostota plazme je bila približno 1×10^{16} m^{-3} in temperatura elektronov okoli 3 eV. Vzorci polipropilena so bili izpostavljeni CF_4 plazmi za 10 minut. Pred in po izpostavi so bili analizirani z visoko ločljivim XPS. Poleg fluorovih funkcionalnih skupin smo na površini plazemsko obdelanih vzorcih opazili tudi nekaj at.% aluminija. XPS rezultate smo razložili s šibkim jedkanjem napajane elektrode med plazemsko obdelavo in depozicijo tanke plastni razpršenega materiala (Al) na vzorcih polimera.

1. Introduction

Plasma treatment is a popular method for modification of surface properties of different polymers. Surface energy of polymers can be increased using oxygen or nitrogen plasma, or plasma created in a mixture of argon and residual atmosphere (water vapor usually predominates) /1-6/. The surface energy can be decreased, on the other hand, using fluorine-rich plasma. For safety reasons, pure fluorine is often avoided and many researchers apply plasma created in tetraflourmethane instead. In any case, the surface energy is decreased by formation of a thin film of CF_x functional groups on the polymer surface /7-11/. The functional groups are extremely non-polar so the polymer treated by fluorine plasma becomes highly hydrophobic.

Different discharges are used for creation plasma suitable for hydrophobization of organic materials. They include the RF /12-14/ and MW /15-16/ discharges. The RF discharges can be used in two different modes: i) capacitively coupled and ii) inductively coupled. In capacitively coupled (CC) discharge, plasma is created between two parallel metal electrodes, while in inductively coupled (IC) discharge it is usually created within a coil wounded around a tube made from an insulator. The tube is usually cylindrical and made from a glass. Pyrex, quartz and borosilicate glasses are all popular. The coil assures formation of an oscillating magnetic field inside the tube, which induces an electric field. The electric field is always parallel to the tube, it oscillates with the same frequency as the RF generator, and is rather uniform along the tube, except at the edges of the coil. The induced electric field is 0 at the axes and increases toward the coil as U = const. r^2. The coil is tightly wounded around the discharge tube in order to make use of almost all magnetic field. The acceleration of ions in the oscillating induced electric field is neglected at the frequency above, say, 1 MHz due to a large ion mass /17/. The electrons, on the other hand, are well accelerated in the electric field. They transfer a part of their kinetic energy to gaseous molecules at inelastic collisions. Since there is no electrode in IC plasma, no DC biasing occurs. The plasma is slightly positive against the glass wall in order to equalize the fluxes of fast electrons and slow positive ions onto the surface. The plasma potential in IC discharge is estimated as

$$V_p - V_f = -\frac{kT_e}{2e_0} ln \frac{m_+}{2m_e} \quad (1)$$

Where V_s is the space potential, V_f is the floating potential, k is the Boltzmann constant, T_e is electron temperature, e_0 is the elementary charge, m_+ is the ion mass and m_e is the electron mass. Typical order of magnitude of plasma potential in IC discharges is 10 V.

2. Capacitively coupled plasma

The discharge chamber of our plasma reactor is shown in Fig. 1. The housing is grounded and made from stainless steel while the powered electrode is made from aluminum. Plasma is created in the entire volume of the discharge chamber. The powered electrode is connected to a RF generator via a matching network. The RF generator operates at the standard frequency of 13.56 MHz, and the output power of 100 W. The RF peak - to - peak voltage is about 450 V. Plasma is created in the oscillating electric field between the powered electrode and the ground. At the CF_4 pressure of 1 Pa, the entire volume of the discharge chamber is filled with luminous plasma. Plasma density and electron temperature were estimated with a simple single Langmuir probe mounted into the centre of the plasma reactor. At our discharge parameters the plasma density is about 1×10^{16} m^{-3} and the electron temperature is about 3 eV. The Debye length is

$$\lambda_D = \sqrt{\frac{\varepsilon_0 kT_e}{Ne_0^2}} \qquad (2)$$

Here, l_0 is the influence constant, N is the plasma density, while the other symbols were already defined. Taking into account the measured values of plasma density and electron temperature, the Debye length in our plasma is about 1.3×10^{-4} m. The Debye length depends on N and T_e as a square root, so even if the experimental error was a factor of 2, the Deby length would change for only 40%.

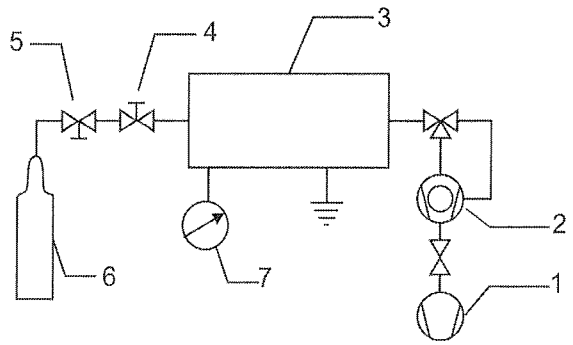

Fig. 1 Discharge chamber

Electrodes in capacitively coupled plasmas acquire a negative potential. The sheath thickness is often said to be "of the order of Debye length". The thickness is difficult to define since the boundary between the sheath and the unperturbed plasma is not sharp, but it is reasonable to say that it is few times the Debye length. At our conditions the sheath thickness is thus estimated to about 1 mm. The potential is oscillating with the generator frequency. Due to the requirement to equalize the fluxes of fast electrons and slow positive ions from unperturbed plasma onto the boundary of the sheath, the average (let us call it DC) electrode potential is negative against plasma.

The potential in the sheaths appears both at powered and grounded electrode, and depends on the area of the electrodes. Smaller electrodes acquire larger potential sheaths. In the classical work, Chapman /18/ assumes that the sheath voltages vary as $V_1/V_2 = (A_2/A_1)^4$. This assumption is based on the work performed by Koenig *et al* /19-20/. A 10 - times smaller electrode would thus acquire a 10000 - times larger potential sheath. This effect is used in the conventional RF sputtering systems: the target is always much smaller than the rest of the discharge system. Best results in terms of thin film deposition by RF sputtering are obtained if the mean free path is smaller than the distance between the powered electrode and the substrate holder. In such cases, the sputtered atoms reach the substrate without a collision in the gas phase.

Our experimental system is not at all intended for sputter deposition of thin films, but the basic concepts still apply. Practically all the generator voltage appears as the sheath voltage next to the powered electrode. The sheath voltage oscillates with the generator frequency and so do positive ions appearing in the sheath. The maximum energy of oscillating ions is

$$W_{max} = \frac{1}{2}mv_{max}^2 = \frac{1}{2}m\left(\frac{eE}{m\omega}\right)^2 = \frac{e^2E^2}{2m\omega^2} \qquad (3)$$

and the amplitude is

$$x_{max} = \frac{eE}{m\omega^2} \qquad (4)$$

As argued above, almost entire RF voltage drop appears across the sheath next to the powered electrode. The DC self bias is thus little less than half of the peak - to - peak voltage of the RF generator, i.e. about 200V. Assuming the thickness of our sheath is 1mm, and a constant electric field across the sheath (which is definitely not true, but serves as a nice simplification), the oscillating electric field is about 400 V/mm. The ion oscillation amplitude is calculated from equation (4) and is about 6×10^{-5} m for F^+ ions, while the maximum energy is calculated from equation (3) and is about 12 eV for the same ions. Lighter ions would gain more energy and would have larger oscillation amplitude, while heavier ions (such as F_2^+ and CF_x^+) would gain less energy and would have smaller oscillation amplitude.

Simple calculations performed by equations (3) and (4) give important results. The ions are too heavy to obtain substantial energy at oscillations so the sheath actually acts as a simple DC potential fall across the sheath, i.e. between the unperturbed plasma and the electrode. If the sheath is collisionless (i. e. the sheath thickness is much smaller than the mean free path), the ions are unlikely to loose their kinetic energy within the sheath and bombard the electrode with the kinetic energy of $W_{k+} = eV$, where e is the ion charge (often e_0) and V is the DC potential self bias. In our case, as estimated above, the kinetic energy of ions bombarding the powered electrode is about 200 eV.

The ions thus transfer their energy to the powered electrode. Since their kinetic energy is much larger than the

binding energy of surface and subsurface atoms, they cause the so called radiation damage. Most ion energy is spent for a collision cascade and thus displacement of surface and subsurface atoms. The atoms tend to rearrange so the net effect is heating of the powered electrode. A small part of the ion energy is used for kicking out free electrons from the powered electrode. The electrons are accelerated across the sheath and reach unperturbed plasma with a high energy. In the case of collisionless sheath, the average electron kinetic energy is about 200 eV. Once in unperturbed plasma, the fast electrons are quickly thermallized at elastic collisions with rather slow plasma electrons and contribute to the heating of electrons in plasma.

A small part of the ion kinetic energy is also used for kicking out atoms from the surface of the powered electrode. The effect is called sputtering and is often expressed in the terms of the sputtering coefficient which has been defined as the number of sputtered atoms leaving the electrode per incident ion. Sputtering coefficients have been determined experimentally for a variety of incident ions, kinetic energy, impact angle, surface finish and target materials. For a quick estimation of the sputtering coefficient many authors apply SRIM software package /21-23/. Although the computer simulation may not give extremely accurate results, it is easy to use and represents a quick method for determination of recombination coefficients. The sputtering coefficients for F^+ and C^+ ions on oxidized aluminum electrode are shown in Fig. 2.

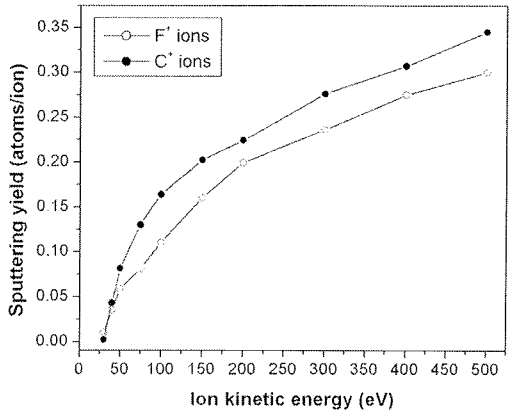

Fig. 2 Sputtering yields for aluminum oxide sputtered by F^+ and C^+ ions

3. Experimental

3.1. Experimental setup

Experiments have been performed in plasma created in the discharge chamber shown in Fig. 1. The chamber is made from aluminum and has inner dimensions 28.5×13.8× 23.5 cm^3. There is a flat rectangular powered electrode in the upper part of the chamber as shown in Fig. 1. The dimensions of this electrode are 21×11×2.5 cm^3. The area of the chamber wall is thus 2800 cm^2 while the area of the powered electrode is 600 cm^2.

The electrode is powered by a RF generator via a matching network. The RF generator operates at the industrial frequency of 13.56 MHz and the output power of 100 W. The discharge chamber is an integral part of the experimental system schematically shown in Fig. 3. The system is pumped with a turbomolecular pump with the pumping speed of 250 l/s backed by a two stage oil rotary pump with the nominal pumping speed of 25 m^3h^{-1}. The turbomolecular pump is mounted about 10 cm apart from the discharge chamber and is connected to the discharge chamber with a stainless steel bellow with the inner diameter of 4.5 cm The effective pumping speed at the entrance to the discharge chamber at the pressure of 1 Pa is therefore not far from the nominal pumping speed of the turbomolecular pump. Pressure is measured with a baratron attached to the discharge chamber. The ultimate pressure in the system is about 0.01 Pa. Gases are leaked through flowmeters. At current experiments, only one flowmeter that was calibrated for tetrafluormethane was used.

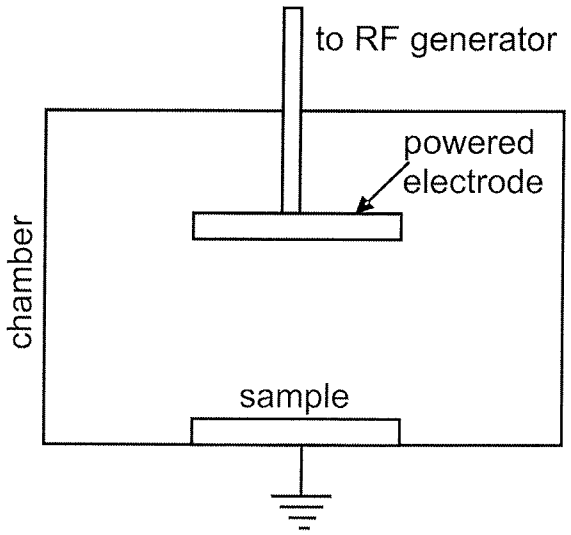

Fig. 3 Experimental set-up: 1 - two-stage rotary pump, 2- turbomolecular pump, 3 - discharge chamber, 4 - flowmeter, 5 - reduction valve, 6 - CF_4 bottle, 7 - pressure gauge

The experiments on the plasma treatment of the polypropylene samples were performed as follows: The discharge chamber was first open to mount a sample onto the bottom of the chamber. The chamber was thus exposed to (humid) air. The chamber was then closed and pumped by the rotary pump to obtain the pressure of few Pa. The turbomolecular pump was turned on and the pressure dropped significantly until after, say half an hour, reached the value of about 0.01 Pa. Tetrafluormethane was then introduced into the discharge chamber to obtain the pressure of 1.0 Pa. The RF generator was turned on for the desired period (in our case the treatment time was 10 minutes).

3.2. XPS analyses

The surface of the samples was analyzed with an XPS instrument TFA XPS Physical Electronics. The base pressure in the XPS analysis chamber was about 6×10^{-8} Pa. The samples were excited with X-rays over a 400-μm spot area with a monochromatic Al $K_{\alpha1,2}$ radiation at 1486.6 eV. The photoelectrons were detected with a hemispherical analyzer positioned at an angle of 45° with respect to the normal to the sample surface. The energy resolution was about 0.5 eV. Survey-scan spectra were made at a pass energy of 187.85 eV, while the individual high-resolution spectra were taken at a pass energy of 23.5 eV and a 0.1 eV energy step. Since the samples are insulators, we used an additional electron gun to allow for surface neutralization during the measurements. All spectra were referenced to the main C 1s peak of the carbon atoms which was assigned a value of 284.8 eV. The spectra were analyzed by using MultiPak v7.3.1 software from Physical Electronics, which was supplied with the spectrometer.

4. Results

XPS survey spectrum for an untreated polypropylene (PP) disc is shown in Fig. 4. As expected form the chemical composition of the virgin PP, carbon predominates. The small concentration of oxygen on the untreated sample is probably due to water adsorption. The high resolution C1s peak for an untreated sample is shown in Fig. 5. The peak is rather uniform - no subpeaks due to carbon bonding with atoms other than C or H are observed. The composition of the surface layer of untreated samples is shown in Table 1. The XPS analyses were performed on 3 samples in order to have some statistics. As expected, no F or anything else was detected on untreated samples, except perhaps some Si whose origin is unknown.

Table 1 Surface composition of the untreated polypropylene sample (three measurements)

Sample	C	O	Si
PP untreated (1^{st})	97.4	2.3	0.3
PP untreated (2^{nd})	98.9	0.9	0.2
PP untreated (3^{rd})	98.4	1.3	0.3

XPS survey spectrum for polypropylene (PP) disc treated by CF_4 plasma is shown in Fig. 6. Apart from the small concentration of O and N, one can observe F in a substantial amount too. The high resolution C1s peak for plasma treated sample is shown in Fig. 7. The peak now contains several subpeaks due to carbon bonding with F (as well as O and N) atoms, what is an expected feature. More surprising is an appearance of the Al peak which is clearly distinguished from the background. The composition of the surface layer of plasma treated samples is shown in Table 2. Again, the XPS analyses were performed on 3 samples in order to have some statistics.

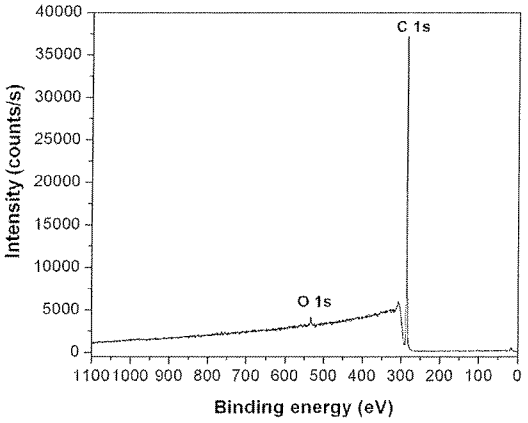

Fig. 4 XPS survey spectrum of the untreated polypropylene sample

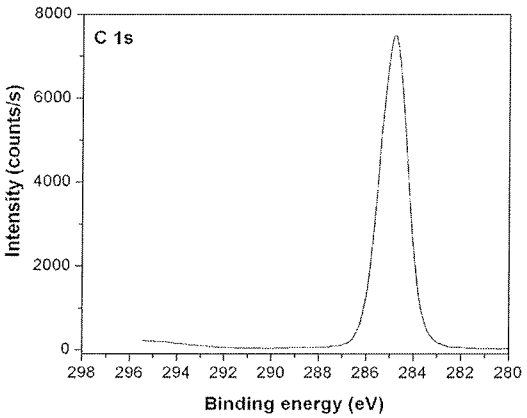

Fig. 5 High-resolution XPS spectrum of C 1s peak of the untreated polypropylene sample

Table 2 Surface composition of the polypropylene sample treated in CF_4 (three measurements)

Sample	C	O	N	Si	F	Al
PP treated in CF_4 (1^{st})	45.1	7.0	2.6	/	36.8	8.6
PP treated in CF_4 (2^{nd})	43.4	6.4	2.0	3.0	38.5	6.7
PP treated in CF_4 (3^{rd})	43.1	5.5	2.4	2.2	39.1	7.6

5. Discussion

The appearance of the F-rich functional groups on the surface of samples treated by CF_4 plasma is expected. Namely, as shown by numerous authors /24-26/, the result of the plasma treatment is a formation of F-rich functional groups on the surface of the PP polymer. Any discussion on the composition, let alone the structure of the surface film, is beyond the scope of this paper.

More interesting is the appearance of aluminum on the surface of plasma treated samples. This is important from both scientific and applied view. Namely, while F-rich functional groups cause a decrease of surface energy and thus the

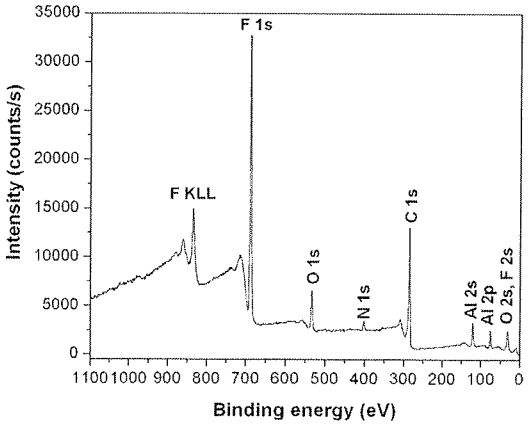

Fig. 6 XPS survey spectrum of the polypropylene sample treated in CF_4 plasma

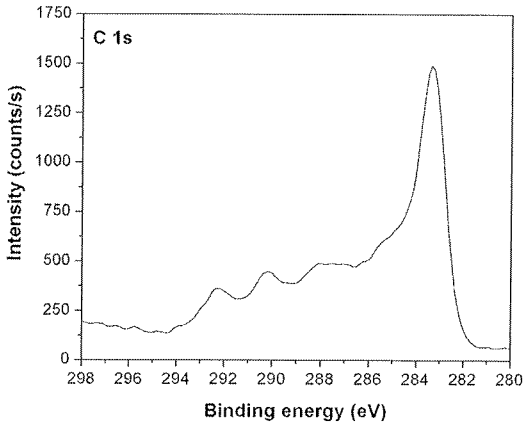

Fig. 7 High-resolution XPS spectrum of C 1s peak of the polypropylene sample treated in CF_4 plasma

decrease of the wettability, aluminum definitely has the opposite effect: metals always have high surface energy and should contribute to an increase of the surface energy.

The appearance of a thin film of aluminum on the sample surface is explained by sputtering of the powered electrode. As already mentioned, almost entire DC self bias occurs at the powered electrode. Let us first consider the type of ions bombarding the powered electrode. The electron temperature is only a few eV. Average electrons are therefore likely to excite CF_4 molecules to a variety of vibrational and rotational states but cannot dissociate or ionize the molecules. Only the fastest electrons are capable of dissociation and ionization. The lowest dissociation energy of about 12.5 eV is found for the reaction $CF_4 \rightarrow CF_3 + F$. Since the electron temperature in our plasma is rather low, this reaction probably prevails. Apart from it, dissociation like $CF_3 \rightarrow CF_2 + F$ seems quite possible, but is definitely less probable. The final concentrations of CF_x molecules should decrease in the following way: CF_4, CF_3, CF_2, CF, C. The concentration of F atoms should be a bit higher than the concentration of CF_3 molecules if F atoms are not lost by some mechanisms. The gas phase loss can be neglected at the pressure of 1 Pa, while there are some possible mechanisms of the F loss on the surfaces facing plasma. They include heterogeneous surface recombination of F atoms on the walls of the discharge chamber and the powered electrode (reaction $F + F \rightarrow F_2$) and substitution of the H atoms on the surface of polypropylene with F atoms (reaction $C_xH_y + F \rightarrow C_xH_{(y-1)}F$). The recombination coefficient for the first reaction is unknown. Namely, to the best of our efforts we could not find literature reporting the recombination coefficient for F atoms on the surface of (surface oxidized) stainless steel or aluminum. However, we can estimate the loss by the other mechanism. Let us estimate a 1% dissociation fraction of CF_4. The partial pressure of F atoms in our plasma is then 0.01 Pa and the corresponding density of F atoms is $n = p_K/kT = 2.4\times10^{18}\,\mathrm{m}^{-3}$. The resultant flux of F atoms on the PP sample is then $j = \frac{1}{4} n\langle v\rangle$. Assuming the average random velocity of F atoms of 500 m/s the flux is then $j = 3\times10^{20}\ \mathrm{m}^{-2}\mathrm{s}^{-1}$. Taking into account the number of atoms on the surface of solid materials, which is roughly $1\times10^{19}\ \mathrm{m}^{-2}$ one can clearly see that the loss of F atoms due to substitution of H from polypropylene is negligible.

Let us now estimate the type of ions bombarding our powered electrode. The relevant literature does not report CF_4^+ ions so the first candidates are CF_3^+ ions appearing at the reaction $CF_4 + e \rightarrow CF_3^+ + F + e$ or at simple ionization of the CF_3 radical. Since the density of CF_4 molecules is much larger than the density of CF_3 molecules and F atoms (let alone CF_2 and CF molecules), we can expect that the CF_3^+ ions will prevail. These ions are accelerated in the DC sheath and bombard the powered electrode with the kinetic energy of about 200 eV. As soon as an ionized molecule reaches the electrode surface it is dissociated to atoms. On the average, each atom takes about a fourth of the CF_3^+ ion kinetic energy, i.e. about 50 eV. This is thus the available kinetic energy of each particular atom. As we already mentioned, most of the energy is spent for the electrode heating and a smaller fraction is spent for sputtering. The sputtering coefficients for F and C atoms (or ions) versus the kinetic energy are shown in Fig. 2. At the kinetic energy of 50 eV, the sputtering coefficient for oxidized aluminum is about 0.08. For F^+ ions with the kinetic energy of 200 eV the coefficient is much larger at around 0.2, but as argued above, the density of F^+ ions in plasma is much smaller then the density of CF_3^+ ions so the contribution of F^+ ions from plasma to the electrode sputtering is easily neglected.

Let us now estimate the etching rate of the powered electrode. If the ion density in unperturbed plasma is $1\times10^{16}\mathrm{m}^{-3}$ the resultant flux of CF_3^+ ions onto the electrode surface is about $1\times10^{18}\ \mathrm{m}^2\,\mathrm{s}^{-1}$. Tanking into account the sputtering coefficient of 0.08 and the fact that there are 4 atoms in the CF_3 molecule, the powered electrode is etched at the rate of

$$\frac{dx}{dt} = j\frac{S}{N_s} \qquad (5)$$

where j is the ion flux, S is the sputtering coefficient and N_s is the atom density in the solid material. Taking into ac-

count the numerical values, i.e. $j = 1\times10^{18}$ m^{-2} s^{-1}, $S = 0.08$ and $N = 1\times10^{19}$ m^{-2}, the etching rate is about 10^{-2} monolayers of oxidized aluminum per second. The samples are exposed to plasma for 10 minutes, i.e. 600 s. In this period, the powered electrode is etched for about 2.5 monolayers. The sputtered atoms leave the powered electrode with a small kinetic energy and are deposited on the chamber walls as well as on the surface of the polypropylene samples. Since the area of the samples mounted opposite the powered electrode is much smaller than the area of the powered electrode, we can assume a homogeneous flow of sputtered atoms on the surface of the substrate. The powered electrode is made from aluminum but exposed to air prior to any plasma experiment, so a thin film of oxide is formed on its surface. According to the literature /27-28/ the thickness of this native oxide film is several nm, so much more than the thickness of the etched film during our experiments. Since the Al atomic concentration in alumina is 40% the expected thickness of the Al film on the polypropylene surface is 2.5×0.4 = 1 monolayer. This should be true if the mean free path of the sputtered atoms is larger or close to the distance between the electrode and the sample.

At the pressure of 1 Pa, the mean free path of molecules and atoms is close to 1 cm. The distance between the powered electrode and the samples is about 10 cm. The sputtered atoms are therefore unlikely to go directly towards the sample, but they rather diffuse in the space between the powered electrode and the sample. Since a sample has a much smaller area than the powered electrode, the diffusion should not influence the thickness of the deposited Al film on polypropylene.

Another effect, however, should be addressed before concluding the thickness of the Al film on our samples. The system is pumped by the turbomolecular pump and CF_4 is continuously leaked into the chamber. There is obviously a drift of gas from the entrance port toward the pump. If the geometry of our discharge vessel was cylindrical with the length much longer than the diameter and if the initial gas drift velocity was low, one would be able to calculate the drift velocity of the gas between the electrode and the samples. In our case, however, the discharge vessel has other geometry, and the drift velocity of gas entering the discharge chamber is far from being low. Namely, the gas is leaked into the system through the flowmeter, i.e. an extremely narrow tube. At the exit of the flowmeter, the gas drift velocity is close to the sound velocity, i.e. around 300 m/s. The gas jet expands into the discharge chamber and the drift velocity between the powered electrode and the samples is much smaller than at the entrance, but definitely large enough to push sputtered atoms toward the pump, i.e. away from the samples. For this reason, the thickness of the Al film on the polypropylene is definitely smaller than 2.4 nm, which was calculated ignoring the gas drift. The thickness could be calculated taking into account both the diffusion and the gas drift, but the calculation is definitely beyond the scope of this paper. We can only conclude that the expected thickness of the Al film on the polypropylene samples is of the order of 0.1 monolayers, or perhaps close to a monolayer.

The upper considerations are sound with the measured XPS survey spectra (Fig. 7). The Al concentration on the sample surface, as calculated from the XPS survey spectrum, is about 7 at.%. If the XPS would measure the composition of the uppermost atomic layer, this would mean that the thickness would be only 0.07 monolayers, i.e. several times smaller than the estimated value, which should be several 0.1 monolayers. This discrepancy is explained by the simple fact that XPS does not measure the concentration of elements in the uppermost layer only, but gives some average over a thicker film, say up to the equivalent of about 10 nomolayers. It is clear that the uppermost layer contributes more to the XPS spectrum than the subsurface layers, but it is difficult to calculate the exact thickness of the Al film on the PP samples. Not only the escape depths of photoelectrons, but the surface morphology would have to be taken into account as well.

Let us finally explain the fact that the O concentration on the surface of plasma treated samples is several times larger than on the untreated samples. The most probable explanation for this effect is oxidation of aluminum. Freshly sputter deposited Al is likely to bond oxygen. There are some sources of oxygen atoms (or molecules) in the discharge chamber. The first one is sputtering of the oxidized aluminum, but due to a poor sputtering rate it is easily neglected. The major source of oxygen is a virtual leak originating from desorption of water molecules from the walls of the discharge chamber. The ultimate pressure in our system is about 0.01 Pa. Since the system is never baked prior to plasma experiments, the majority of the residual atmosphere is water vapor. The number of molecules leaving the surface in unit time is estimated using the data on the ultimate pressure and the effective pumping speed:

$$\frac{dN}{dt} = p_0 \frac{S_{eff}}{kT} \qquad (6)$$

where p_0 is the ultimate pressure, S_{eff} is the effective pumping speed, k is Boltzmann constant, T is the gas temperature. Taking into account the numerical values, one can estimate the number of molecules leaving the surface in unit time to $dN/dt = 1\times10^{20}$ s^{-1}. This value is orders of magnitude larger than the number of oxygen atoms entering the discharge volume due to sputtering of the powered electrode (Al_2O_3). The water molecules are oxidative enough, but they also dissociate to H and OH in plasma so they are effective oxidizers.

6. Conclusion

Polypropylene samples were treated by CF_4 plasma created in a capacitively coupled RF discharge. As expected, a thin film of CF_x functional groups appeared on the sample surface during plasma treatment. The concentration of fluorine on plasma treated samples was estimated by XPS

analyses, and it was close to 40 atomic %. Apart from fluorine, a thin film of aluminum was formed on the sample surface as well. The appearance of the Al was explained by sputtering of the powered electrode. The thickness of the Al film on the PP samples was estimated to several 0.1 monolayers from the XPS results. This value was explained taking into account gas phase and surface phenomena. Although the calculations include several simplifications as well as uncertain data, the theoretical calculation is sound with the experimental results.

References

/1./ Wang MJ, Chng YI, Poncin- Epaillard F (2005) Surf Interface Anal 37:348

/2./ Ahmadi NS, Chehimi MM, Khonsari FA, Belacemi NF, Amouroux J, Delamar M (1995) Colloid Surface A 105:277

/3./ Cvelbar U, Mozetic M, Junkar I, Vesel A, Kovac J, Drenik A, Vrlinic T, Hauptman N, Klanjsek-Gunde M, Markoli B, Krstulovic N, Milosevic S, Gaboriau F, Belmonte T (2007) Appl Surf Sci 253:8669

/4./ Vrlinic T, Vesel A, Cvelbar U, Krajnc M, Mozetic M (2007) Surf Interface Anal 39:476

/5./ Mafra M, Belmonte T, Maliska A, da Silva Sobrinho AS, Cvelbar U, Poncin-Epaillard F (2008) Key Eng Mater 373/374:421

/6./ Canal C, Molina R, Bertrán E, Erra P (2004) J Adhes Sci Technol 13:1077

/7./ Truesdale EA, Smolinsky G (1979) J Appl Phys 50:6594

/8./ Hopkins J, Badyal JPS (1995) J Phys Chem 99:4261

/9./ Hopkins J, Badyal JPS (1996) Langmuir 12:3666

/10./ Strobel M, Thomas PA, Lyons CS (1987) J Polym Sci A 25:3343

/11./ Marais S, Metayer M, Poncin- Epaillard F (2001) J Fluorine Chem 107:199

/12./ Tressaud A, Durand E, Labrugčre C (2004) J Fluorine Chem 125:1639

/13./ Wen CH, Chuang MJ, Hsiue GH (2006) Thin Solid Films 503:103

/14./ Occhiello E, Garbassi F (1988) Polymer 29:2277

/15./ Marais S, Hirata Y, Cabot C, Morin- Grognet S, Garda MR, Atmani H, Poncin- Epaillard F (2006) Surf Coat Technol 201:868

/16./ Fresnais J, Benyahia L, Chapel JP, Poncin- Epaillard F (2004) Eur Phys J Appl Phys 26:209

/17./ Eiselt P (2007) Inform MIDEM 37:175

/18./ Chapman B (1980) Glow discharge Processes. J Willey and Sons, New York

/19./ Koenig R, Maissel LI (1970) IBM J Res Develop 14:168

/20./ Koenig R (1972) US patent 3661761

/21./ Amekura H , Plaksin OA, Umeda N, Kono K, Kishimoto N, Buchal C (2006) Vacuum 80:802

/22./ Glaude AS, Thomas L, Tomasella E, Badie JM, Berjoan R (2006) Surf Coat Technol 201:174

23. Mozetic M, Zalar A, Jagielski J, Evangelakis GA, Drobnic M, Chab V (1999) Inform MIDEM 29:117

/24./ Denes F, Hua ZQ, Young RA, Shohet JL (1997) Plasmas and Polymers 2:1

/25./ Hopkins J, Boyd RD, Badyal JPS (1996) J Phys Chem (100):6755

/26./ Strobel M, Corn S, Lyons CS, Korba GA (1987) J Polym Sci A Polym Chem 25:1295

/27./ Strobel M, Corn S, Lyons CS, Korba GA (1985) J Polym Sci A Polym Chem 23:1125

/28./ Mozetic M, Zalar A, Cvelbar U, Babic D (2004) Surf Interface Anal 36:986

A. Vesel, M. Mozetic*

Plasma Laboratory, Jozef Stefan Institute, Jamova cesta 39, 1000 Ljubljana, Slovenia

**corresponding author:*
Phone: +38614773502,
Fax: +38614773440,
E-mail: alenka.vesel@guest.arnes.si

Prispelo (Arrived): 15.07.2009 *Sprejeto (Accepted): 09.03.2010*

AN LTCC-BASED CAPACITIVE PRESSURE SENSOR WITH A DIGITAL OUTPUT

Marina Santo Zarnik[1], Matej Možek[2], Srečko Maček[3], Darko Belavič[1]

[1]HIPOT-RR d.o.o., Otočec, Slovenia
[2]Faculty of Electrical Engineering, University of Ljubljana, Ljubljana, Slovenia
[3]Jožef Stefan Institute, Ljubljana, Slovenia

Key words: Pressure sensor, 3-D LTCC structure, capacitive sensing, capacitive-to-digital conversion, low power consumption.

Abstract: A capacitive pressure sensor, fabricated using low-temperature cofired ceramic (LTCC) materials and technology was considered for an application in a wireless sensor system. LTCC technology is inherently efficient for 3D structuring and exhibits good dimensional definition and stability, appropriate material flexibility (higher than the commonly used alumina), good chemical resistance, and low moisture absorption, which makes it appropriate for a wide range of sensor applications, even in some extreme conditions and harsh environments. However, very often in such applications, remote control and operation in a low power-consumption mode are required. In order to meet such demands, electronics for signal processing and power managing, based on a capacitance-to-digital conversion, were realised by using an Analog Devices AD7746. A sensor characterization system with the corresponding software for an evaluation of the sensor's nonlinearity and temperature sensitivity is presented. The typical characteristics of the capacitive sensing elements were as follows: a sensitivity of 1.7 fF/mbar, a temperature dependence of 9 fF/°C and a temperature dependence of the sensitivity of less than 2 aF/mbar/°C. The digital temperature compensation was performed with a two-dimensional rational polynomial approximation, resulting in a less than 0.4% FS temperature error in the compensation range 10 °C to 75 °C.

Kapacitivni senzor tlaka z digitalnim izhodom izdelan v LTCC tehnologiji

Kjučne besede: senzor tlaka, 3-D LTCC struktura, kapacitivni senzor, kapacitivno digitalna pretvorba, nizka poraba.

Izvleček: V prispevku so prikazani rezultati študije kapacitivnega keramičnega senzorja tlaka za uporabo v brezžičnem senzorskem sistemu. Senzor je izdelan z uporabo keramike z nizko temperaturo žganja (LTCC - low temperature cofired ceramic) in z ustreznimi novimi tehnološkimi postopki. LTCC materiali in tehnologija so primerni za oblikovanje tri-dimenzionalnih keramičnih struktur. Poleg tega imajo LTCC materiali približno trikrat nižji Youngov modul elastičnosti v primerjavi z najpogosteje uporabljano korundno keramiko, kar omogoča doseganje večje tlačne občutljivosti senzorja. Zahvaljujoč še nekaterim drugim lastnostim, kot so kemična stabilnost in nizka absorpcija vlage, je LTCC keramika zelo primerna za uporabo v različnih medijih in celo v nekaterih ekstremnih pogojih. Pogosto je pri tovrstni uporabi potrebno zagotoviti tudi prenos in obdelavo merilnih rezultatov v oddaljeni enoti ob energijsko varčnem delovanju. V ta namen smo tudi izbrali kapacitivni senzorski princip, ki je že v osnovi energijsko varčen. Pretvorba in procesiranje senzorskega signala je izvedena z uporabo kapacitivno-digitalnega pretvornika AD7746. Predstavljen je merilni sitem z ustrezno programsko podporo za evaluacijo temperaturne kompenzacije senzorske karakteristike. Tipične karakteristike izmerjenih prototipov so naslednje: tlačna občutljivost je 1.7 fF/mbar, temperaturna odvisnost ničelne kapacitivnosti je 9 fF/°C in temperaturna odvisnost občutljivosti je manjša od 2 aF/mbar/°C. Z digitalno kompenzacijo temperaturne odvisnosti odziva smo dosegli napako manjšo od 0,4% FS na kalibracijskem temperaturnem področju 10 °C do 75 °C.

1. Introduction

Thick-film ceramic pressure sensors have been used for many years in a variety of special applications /1, 2/. One advantage of such ceramic sensors is that they can be employed in severe environments: such as high temperatures, magnetic fields, harsh atmospheres and in some aggressive liquids. Realised with the use of Low Temperature Cofired Ceramic (LTCC) materials and technology and offering advantageous features for 3D structuring /3/ (structures with cavities and channels, and buried electronic components, such as conductors, resistors or other functional layers) they have the potential to be an alternative to micro-machined sensors in silicon /6-9/. The most common application is a diaphragm-type ceramic pressure sensor. Depending on the sensing principle, the pressure-induced deformation of the thin ceramic diaphragm is converted into an electrical signal, which is proportional to the changes of the characteristics of the thick-film sensing structure on it (thick-film piezoresistors, thick-film piezoelectric structures or a capacitive sensing structure). The appropriate electronics for the sensors' signal processing can be realised directly on the ceramic structure, i.e., the 3D ceramic structure can be used as a package substrate at the same time.

In order to ensure low power consumption, the capacitive sensing principle is one of the most appropriate methods /4-5/. In addition, the ceramic capacitive sensors have further advantages: a very high sensitivity and, accordingly, a potentially high resolution, robustness, good stability, and drift-free measurement capability. However, they traditionally require more complex interfacing circuits, which represented a major disadvantage in the past. Generally, the capacitive sensing utilises the deformation-induced capacitance change to convert the information of the applied pressure into the electrical signal, such as changes of the oscillation frequency, time, charge, and voltage. The translation from voltage or current to a digital word requires an additional analogue-to-digital converter (ADC). The expected variance in capacitance is generally of the order of several pF or less. In many cases the signal capacitance is

much smaller than the parasitic capacitances present in the measuring circuit, which represents a difficult interfacing task. However, a modification of the conventional sigma delta ADC architecture has been identified as a suitable basis for a monolithic Capacitance to Digital Converter (CDC) /12/. The circuit is parasitic insensitive, and can be configured to work with both a floating and a grounded configuration /16/.

Precision capacitive-sensor interface products are based on a well-established sigma-delta (ΣΔ) conversion technology. Converters utilizing the ΣΔ principle offer excellent linearity and very high resolution, and are ideal for most sensor-interfacing applications. In a conventional voltage input ΣΔ converter, the unknown charge is derived from charging a fixed capacitor to an unknown input voltage, while in the CDC realization, the voltage is fixed and the capacitor is variable. Such an arrangement maintains the high precision and accuracy that is typical for ΣΔ ADCs /13/. Modern implementations enable the measurement of capacitances in the atto Farad (aF) range /15, 16/, with an effective noise resolution of 21 bits and a corresponding resolution down to 4aF. They offer measurements of common-mode capacitance up to 17pF on the 4pF range with a 4fF measurement accuracy. These implementations offer complete sensor solutions; however, their application is limited to an indication of temperature and by the humidity dependence problem /17, 18/ of capacitive sensors, while not offering an effective implementation for the compensation of these unwanted quantities.

This work reports on the results of a case study of a thick-film capacitive pressure-sensor module made with LTCC technology. The electronics for the signal processing and power managing, based on a capacitance-to-digital conversion, were realised with the use of an Analog Devices AD7746, which was placed directly on the ceramic structure, close to the sensing capacitor electrodes. The sensor is connected via an interface module to the I^2C - USB converter, which is used to interface the sensor to the host computer (PC). The prototype sensors were characterised in the pressure range 0-1 bar. The stability and the temperature dependence of the sensors' characteristics were discussed and an effective method for temperature compensation is presented. The sensor nonlinearity and temperature sensitivity were analyzed. In order to achieve the compensation and linearization, an effective method of temperature compensation based on a two-dimensional rational polynomial description of the sensor characteristic was employed.

2 Ceramic capacitive pressure sensors

2.1 Theory of capacitive sensing

The construction of the LTCC-based capacitive pressure sensor consists of a circular, edge-clamped deformable diaphragm that is bonded to a rigid ring and the base substrate. One electrode deposited on the rigid substrate and one electrode deposited on the deformable diaphragm form a parallel-plate air-gap capacitor. The operation of the capacitive pressure sensor is based on changing the air gap between the electrodes as a result of the applied pressure (Figure 1).

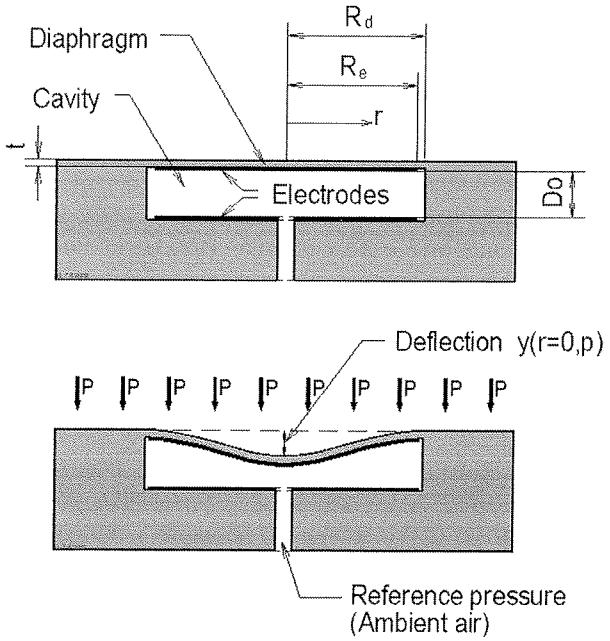

Fig. 1: The construction of the capacitive pressure sensor (above). The deflection of the diaphragm under the measuring pressure applied to the exterior surface of the diaphragm (below).

The capacitance between the electrodes on the deflected diaphragm and the rigid substrate can be expressed with equation (1)

$$C(p)=\varepsilon_0\cdot\varepsilon_r\cdot\int_0^{R_e}\frac{2\cdot\pi\cdot r\cdot dr}{D_0-y\,(r,p)} \qquad (1)$$

where ε_0 and ε_r are the dielectric permittivity of free space and the relative dielectric permittivity of the dielectric, R_e is the radius of the electrode, r is the distance from the centre of the electrode/diaphragm, D_0 is the distance between the electrodes at zero pressure, p is the measuring pressure and $y(r,p)$ is the deflection of the diaphragm when the pressure is applied. For a clamped circular diaphragm $y(r,p)$ can be calculated from (2)

$$y(r,p)=\frac{3p\left(1-\nu^2\right)\left(R_d^2-r^2\right)^2}{16\,E\,t^3} \qquad (2)$$

where t and R_d are the thickness and the radius of the diaphragm, E is the Young's modulus and n is the Poisson's ratio of the diaphragm. Substituting equation (2) into (1) allows preliminary calculations of the sensitivity in the sensor's design phase. Notice that depending on how the pressure is applied, i.e., on the exterior surface of the diaphragm or in the interior of the cavity (or equivalently, if the pressure or an under-pressure is applied), $y(r,p)$ with a

positive or negative sign should be considered. However, the sensor's sensitivity to the applied pressure depends on the area of the electrodes and the initial distance between them. Accordingly, the realization of a very small distance between the electrodes is essential if we are to achieve a high resolution.

2.2 LTCC-based capacitive sensing structure

In a typical capacitive pressure-sensor construction the thick-film ceramic pressure sensor consists of a ceramic capsule, i.e., a cylindrical cavity (air gap), closed with a thin flexible ceramic diaphragm parallel to a rigid reference substrate. The thick-film electrodes of the sensing capacitor were made on the diaphragm and the substrate plane inside the cavity in co-processing with the LTCC structure. The cross-section of the LTCC-based capacitive pressure sensor considered in this case study is schematically presented in Figure 2. The important dimensions of the prototype sensors were as follows: a diaphragm diameter of 9 mm and a thickness of 200 mm, an electrode diameter of 8.5 mm, and air gap between the electrodes of 50-70 µm. Such a sensor provides a total capacitance change of approximately 1.5 pF for an applied pressure in the range of 0-1 bar. A detail of the parallel-plate air-gap capacitor (cross-section of the LTCC-based sensor structure) is shown in Figure 3. Figure 4 shows the prototype of the LTCC-based capacitive pressure-sensor module with AD7746/45. In order to minimise the stray capacitances that adversely influence the sensitivity to the pressure loads the CDC was placed on the same ceramic substrate, as close as possible to the capacitor electrodes. In this realisation the top surface of the diaphragm is covered with a 3-µm-thick Au film with the same dimensions as the electrode inside the ceramic capsule.

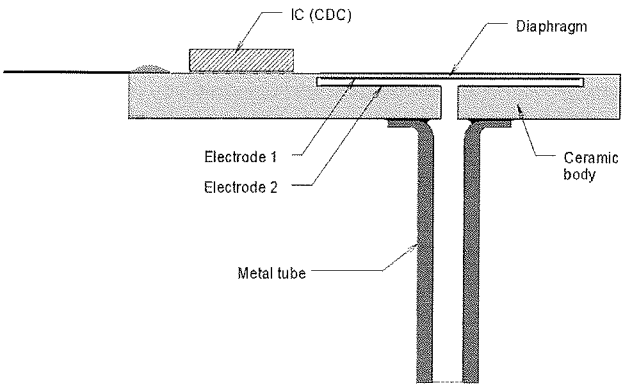

Fig. 2: Schematic representation of the cross-section of the sensor structure (not to scale)

3. Capacitive sensor characterization systems

The generalized layout of the capacitive-sensor measurement system is depicted in Figure 5. The sensor is connected via the interface module to the I^2C - USB converter, which is used to interface the sensor to the host PC. A dedicated electronic interface module was designed. This module enables data transmission and the control of the CDC AD7746. The module itself is based on a CY8C24794 Programmable System on Chip (PSoC) circuit.

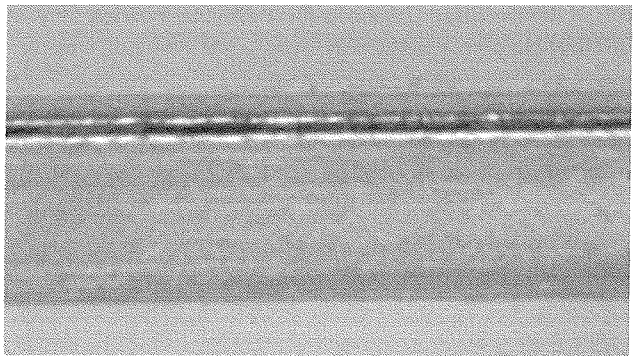

Fig. 3: A detail of the cross-section of the LTCC structure with the air gap between the cofired thick-film electrodes on the diaphragm and the rigid base.

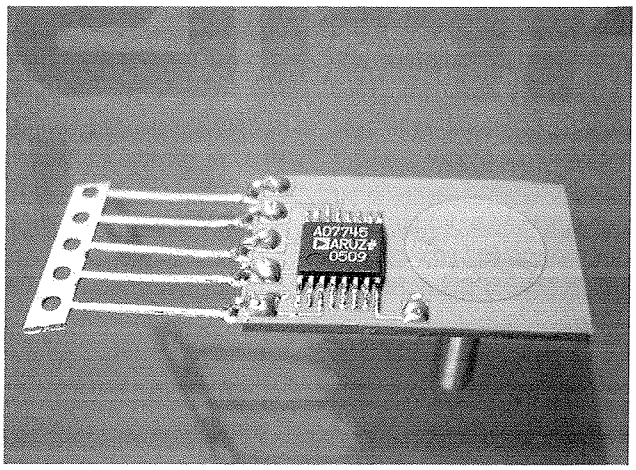

Fig. 4: Prototype of the capacitive ceramic pressure sensor with the AD7745.

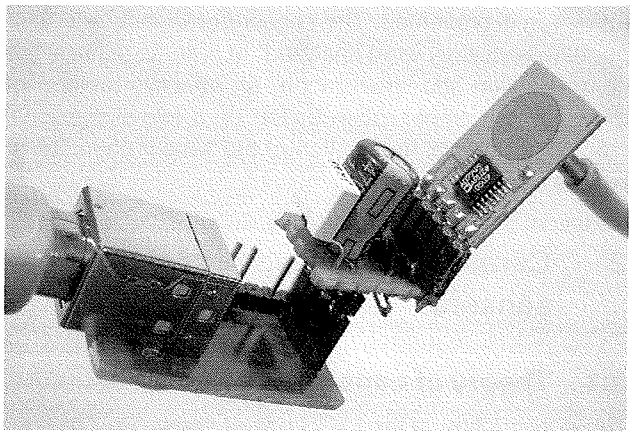

Fig. 5: Capacitive sensor evaluation module

The hardware is used to directly map the CDC to the controlling PC. The corresponding PC software performs the functions of CDC status and data reading. In fact, the controlling software implements all the functions of the AD7746: from the capacitance channel setup to the temperature sensor channel setup, as well as the channel excitation, the common mode capacitance setting, the offset and the gain of the capacitive measurement channel.

The measurement-range optimization was performed in order to obtain the maximum span of the CDC measurement range. The measured device, the LTCC capacitive sensor /18/, exhibits a negative slope for the sensor characteristic. Therefore, the measurement-range optimization must be performed at the maximum pressure readout with a minimum pressure applied and vice versa. This also imposes the order of the compensation algorithms, i.e., the offset compensation is performed before the gain compensation. The sensor offset response is compensated by setting the AD7746 registers CAPDACA and CAPOFFSET. The register value CAPDACA value affects the coarse setting of the offset response and the CAPOFFSET affects the fine setting of the sensor response. The procedure of offset setting is composed of the coarse and fine offset settings. Because of the negative sensor characteristic slope, the fine offset value is initially set at maximum and the coarse value is altered from its initial zero value in such manner that the sensor response is maintained at its maximum value. The setting of the CAPDACA register is performed by a successive approximation approach, starting at the MSB of the CAPDACA register. The subsequent bits are tested against the raw sensor output. If the sensor output exceeds the maximum sensor readout ($FFFF_{16}$) when the corresponding bit is set to 1, then the bit is set to zero and the algorithm advances towards the lower bits.

After the coarse register was set, the CAPOFFSET register is processed in a similar manner. The result of this algorithm is a maximum sensor response value at the applied offset pressure.

After a successful optimization of the offset value, the gain parameter is set in a similar manner. The minimum sensor response is set with an alteration of the CAPGAIN register, which actually changes the clock rate of the front-end of the CDC. The procedure starts with the minimum setting of the CAPGAIN register. The bits of the CAPGAIN register are tested according to the described successive approximation algorithm, just that the bit-testing criterion is now the minimum CDC readout. The result of this algorithm is a minimum sensor response at the maximum applied pressure.

From the capacitive channel output data, where the 0x000000 code represents the zero scale (0 pF), and the 0xFFFFFF code represents the full scale (+4.096 pF), the capacitance can be calculated using the following expressions:

$$C_{sens} = C_0 + C_{offset} + C_S \quad (3)$$

$$C_0 = \frac{Code}{128} \cdot 17pF \quad (4)$$

$$C_{offset} = \frac{Code}{65536} \cdot 1pF \quad (5)$$

$$C_S = (Code\text{-}/0xFFFFFF)*Cref \quad (6)$$

where the *Code* is the corresponding CDC readout and C_{ref} is 4.096 pF.

For the temperature sensor on a chip, the temperature can be calculated from the code (readout of the temperature channel) using the following equation /16/:

$$\text{Temperature (°C)} = (Code/2048)\ \ 4096. \quad (7)$$

3.1. Characterisation of the ceramic capacitive-sensing structure

Initially, the measurements of the prototype sensor were performed for a determination of the optimal settings of the AD7746 and the tested LTCC capacitive sensing structure. The typical sensor characteristic, obtained in an up and down scan of the pressure range 0-700 mbar, at room temperature (25°C ± 0.5 °C) is presented in Figure 6. In order to assess the repeatability the up and down scans were repeated several times. It is evident from Figure 7 that the repeatability was very good and that the tested sensor exhibits practically no hysteresis. For the pressure loads up to 300 mbar the characteristic is almost linear (R^2 = 0.9998), and only for a wider pressure range, over 1 bar, does the deviation from an ideal straight line indicate the necessity for sensor characteristic linearization.

From the CDC readouts the capacitance was calculated using formula (3). As a result, the variation of the capacitance over the pressure range was assessed, which showed a typical sensitivity of 1.8 fF/mbar.

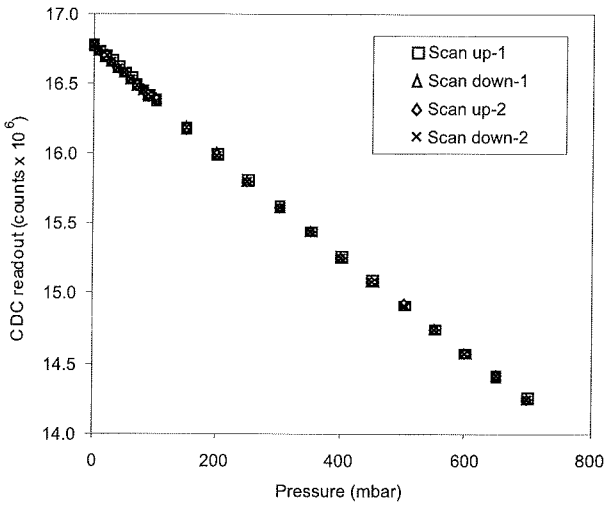

Fig. 6: Initial measurements of the randomly selected test sensor characteristics

In the following, the resolution and the temperature dependence of the sensor's characteristics were measured.

The sensor and the interface electronic circuit were placed in the temperature chamber and the measurement of the raw response was repeated at different temperatures for the temperature range 10-75 °C and for a relative humidity of the air of 30 %. A minimum temperature of 10 °C was selected for the initial measurements in order to avoid potential problems with the humidity control and freezing at the lower temperatures, and to limit affecting the sensors characteristics due to the temperature and humidity dependence of the permittivity of air. These measurements also revealed the susceptibility of the initial electronic circuit design to electromagnetic interference and pointed out the necessity for further improvement of the design in future. During the measurements at the stabilized temperatures in the temperature chamber, switching of the chamber compressor affected the sensor readout and impaired the signal-to-noise ratio.

Figure 7 shows the readouts from the CDC for continuous measurements of the unloaded sensor (C_0), and the ambient temperature, obtained from the on-chip temperature sensor by using relation (7), for the compressor switched ON and OFF. According to Figure 7, the peak-to-peak noise of the sensors signal measured for the compressor switched on was almost two times higher than in the case when the compressor was switched off. Being aware of this effect we continued the characterisation of the capacitive sensing element for its temperature compensation for the stabilised readouts.

The stabilized raw CDC readouts obtained at the different temperatures for different pressure loads are presented in Figure 8. Figure 9 shows the temperature dependence of the sensor with no pressure applied.

The typical characteristics obtained from measurements of several sensing elements (expressed in terms of the capacitance changes) were as follows: the average sensitivity was 1.7 fF/mbar, the temperature dependence of the sensor with no pressure applied, C_0, was 9 fF/°C and the temperature dependence of the sensitivity was less than 2 aF/mbar/°C. The sensors exhibited practically no hysteresis. However, the deviation from an ideal straight line for the wider pressure range and the temperature dependence of the sensor's characteristic indicated the necessity for characteristic linearization.

3.2 Temperature compensation

As the CDC produces a digital capacitance readout, we focused our work on digital implementations of the temperature compensations. In the case of the investigated pressure sensor the temperature compensation requires an accurate mathematical description of the sensor's characteristic pressure and temperature axis. The most adaptable and versatile digital description of the sensor characteristic is achieved with a Taylor expansion, recommended by the IEEE1541.2 standard /19/. Its major drawback is the use of floating-point calculation coefficients and an

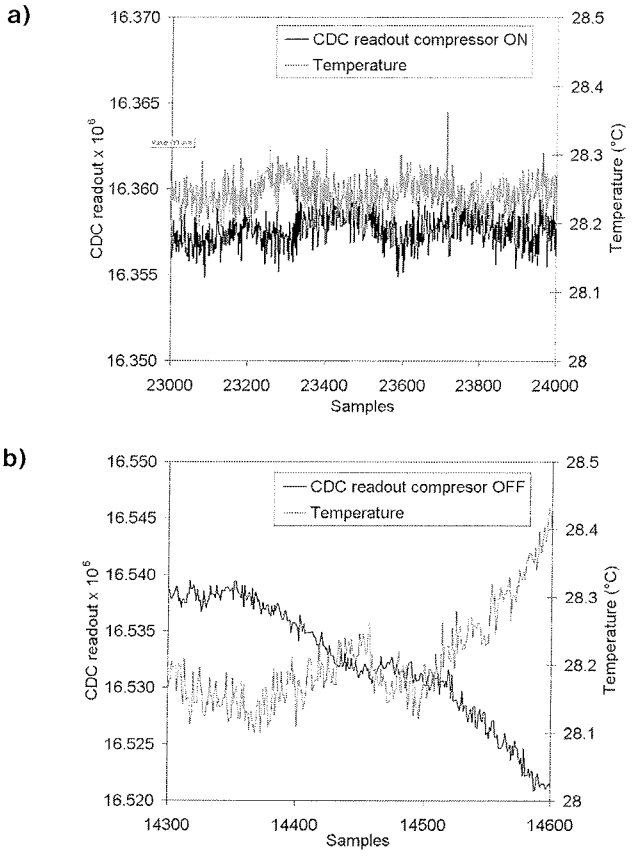

Fig. 7 a: CDC response of C_0 versus number of samples measured with the compressor switched ON, b: CDC response of C_0 versus number of samples measured with the compressor switched OFF

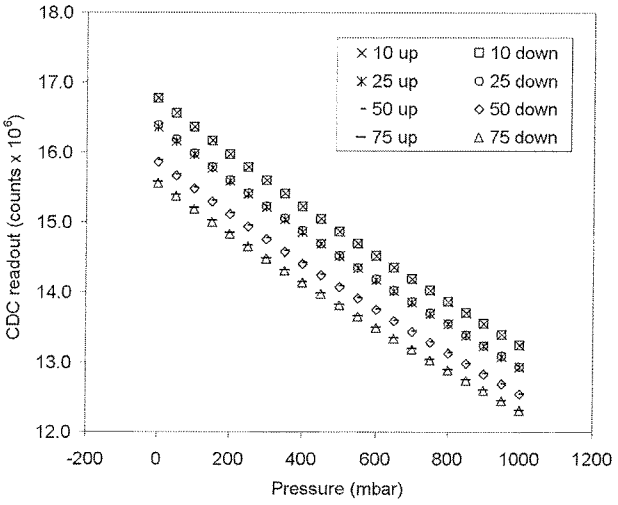

Fig. 8: CDC readouts versus pressure characteristics (for the pressure sweep up and down) at the different temperatures

orthogonal mesh of calibration points. The degree of approximating the polynomial defines the size of the calibration point mesh.

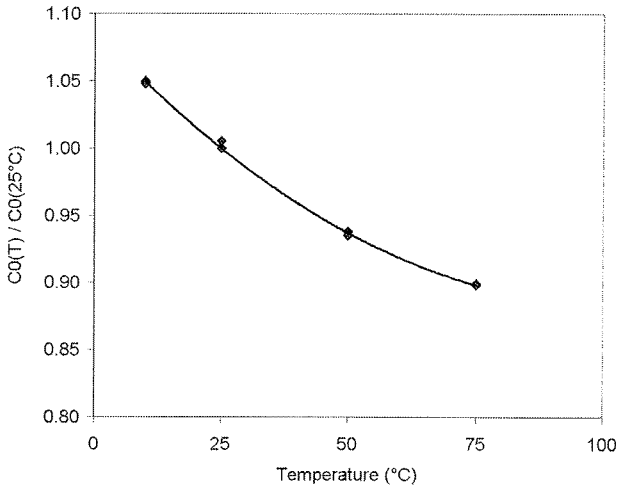

Fig. 9: The temperature characteristic of the sensor output with no pressure applied (C_0) measured in the temperature range -25°C to 75°C.

In order to accommodate the above-mentioned drawbacks, the temperature variations of a typical sensor characteristic can be described by means of a rational polynomial description (8), where A_0 through A_6 are the calibration coefficients of the pressure sensor, which effectively covers the sensor nonlinearity in the pressure and temperature direction to the second order.

$$p = \frac{A_0 + \Delta P + A_1 \cdot \Delta P^2 + A_2 \cdot \Delta T + A_3 \cdot \Delta T^2}{A_4 + A_5 \cdot \Delta T + A_6 \cdot \Delta T^2} \quad (8)$$

Note that in a given formulation of the characteristic description, the actual temperature and capacitance readouts have only an indirect significance on the final measured quantity p, since the calculation of (8) does not depend on the actual value of the capacitance or temperature.

Pressure and temperature measurements are represented by an offset-corrected raw pressure and temperature value. The Δp represents an offset-corrected raw readout from the capacitive sensor, ΔT represents the offset-corrected raw readout from the temperature sensor residing on the sensor signal conditioner. In order to minimize the calibration error, the raw pressure readout p_{oc} and the raw temperature readout T_{oc} are offset according to equation (9) by the corresponding values $p_{ocOFFSET}$ and $T_{ocOFFSET}$ respectively.

$$\Delta p = p_{oc} - p_{ocOFFSET}$$
$$\Delta T = T_{oc} - T_{ocOFFSET} \quad (9)$$

The solution for the unknown coefficients $A_0 ... A_6$ can be found by solving a system of linear equations, obtained from the calibration data. The calibration points for a given sensor are ordered into a seven-point calibration scenario. The calibration scenario represents a sequence of calibration points, comprised of boundary values that define the pressure and temperature calibration interval. The scenario is constructed by setting three temperature points, and pressure points at the endpoints of the corresponding calibration interval. In the case of the presented sensor, the following calibration points were obtained with the pressure-sensor characterization system.

3.2.1 Temperature-compensation evaluation

Software for the acquisition, analysis and calibration of the capacitive sensors was designed. Table 1 summarizes the evaluation of the experimental data depicted in Figure 6. Seven calibration points were used for the evaluation of the calibration coefficients.

Table 1: Input calibration data.

CP#	P_{CAL} (mbar)	T(°C)	pOC	TOC
1	0	10	32746	16424
2	1000	10	25858	16424
3	0	50	30995	16584
4	500	50	27512	16584
5	1000	50	24492	16584
6	0	75	30405	16684
7	1000	75	24037	16684

Additional test points were obtained during the acquisition stage of the calibration process. Test points were obtained at 10 °C, 25 °C, 50 °C and 75 °C in the interval from 0 mbar to 1000 mbar in 50 mbar steps, resulting in a set of 175 test points, which were used in the evaluation process for an assessment of the temperature error.

The calibration dataset was taken from the calibration points in Table 1 and the coefficients were determined. Equation (9) was evaluated at the test points in Table 2. The calibration error, Í, was calculated using the expression

$$\varepsilon = \left| \frac{P_{CAL} - P_{EVAL}}{FS} \right| \cdot 100\% \quad (10)$$

where P_{CAL} represents the calibration pressure point, P_{EVAL} represents the evaluation pressure and FS represents the output pressure span. The evaluation of the system of linear equations based on equation (10) yields the calibration coefficients summarized in Table 2.

Table 2: Calculated calibration coefficients.

A0	A1	A2	A3	A4	A5	A6
-6547	-1703	5148	-4246	-29413	-1307	1990

Equation (9) was evaluated at 175 test-points gathered during the acquisition process using the calibration coefficients in Table 2. The pressure and temperature offset values $p_{ocOFFSET}$ and $T_{ocOFFSET}$ were selected at 30000 and 16500 respectively. The results are summarized in Figure 10, which shows the calibration error ε calculated using equation (10). Figure 3 also shows the upper and lower admissible calibration temperature error band for a typical sensor application.

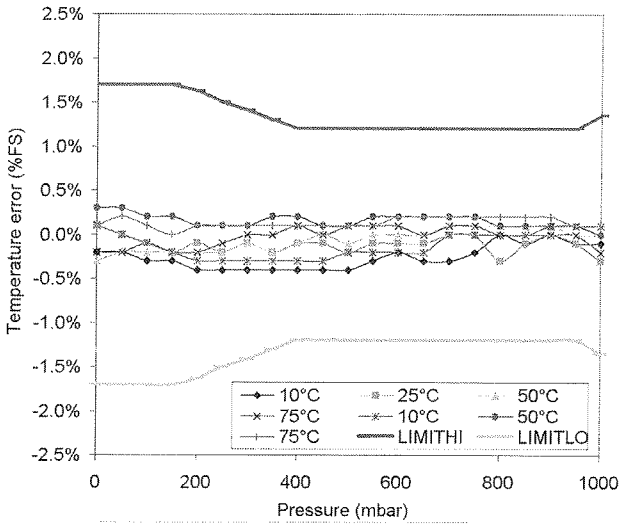

Fig. 10: Evaluation error at the test-point data.

An implementation of a digital temperature compensation method, developed for piezoresistive pressure sensors, to the field of capacitive sensors was presented in order to achieve an effective compensation and linearization based on a two-dimensional rational polynomial description. The evaluation results of the sensor response were compared against a reference pressure source and the most effective digital temperature compensation was proposed. The proposed digital compensation yields a maximum 0.4% FS error on the compensation range 10 °C to 75 °C and enables 16-bit integer arithmetic, thus making the proposed approach appropriate for use in modern sensor signal conditioner integrated circuits.

3.4 Power consumption

The power consumption was measured at different CDC settings. The supply current was obtained from measurements of the voltage drop in a 100-ohms serial resistor by using a LeCroy 9310C oscilloscope. The results obtained for the idle system and for two different sampling rates, i.e., 90 samples per second (SPS) and 9 SPS, are presented in Figure 11.

It was shown that the power consumption of the idle system of typically 2 mW at the supply voltage of 5V increased for a higher sample rate and did not exceed 5 mW in any case. A further reduction of the power consumption, generally attributed to the very lower clock frequency of the CDC, can be achieved only by turning off the CDC during inactive operation intervals.

4. Conclusions

A capacitive pressure sensor aimed at applications in a wireless sensor system was made using LTCC materials and technology. The tested prototype sensors proved to meet the functional demands imposed by the targeted application on a laboratory scale.

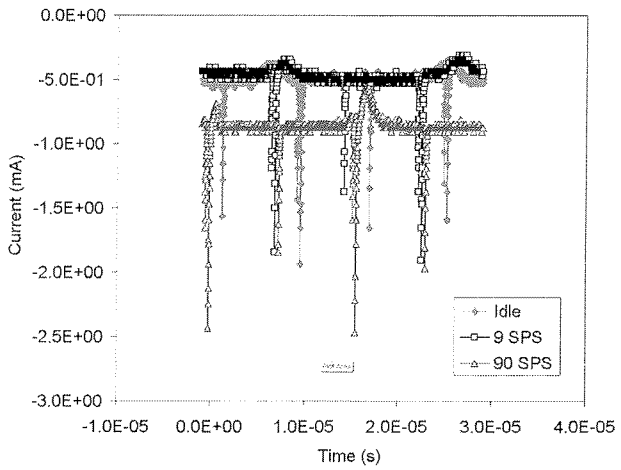

Fig. 11: The current measured for an idle CDC and for two different sampling rates

The typical characteristics of the capacitive sensing elements were as follows: a sensitivity of 1.7 fF/mbar, a temperature dependence of 9 fF/°C and a temperature dependence of the sensitivity of less than 2 aF/mbar/°C. The electronics for the sensor's signal processing, based on the capacitance-to-digital conversion, was realised by use of an Analog Devices AD7746. The sensor characterization system with the corresponding software for evaluation of the sensor's nonlinearity and the temperature sensitivity was built and tested. Digital temperature compensation, performed with a two-dimensional rational polynomial approximation, resulted in a typical temperature error of less than 0.4% FS on the compensation range 10 °C to 75 °C. This enables 16-bit integer arithmetic, making the proposed approach appropriate for use in modern sensor signal conditioner integrated circuits. The power consumption, estimated at the supply voltage of 5V, did not exceed 5 mW.

With smart power management, a significant reduction of the power consumption level and better power efficiency could be achieved in a continuation of this work.

5. Acknowledgements

The financial support of the Slovenian Research Agency and the company HYB d.o.o. in the frame of the project L2-0186 is gratefully acknowledged. The authors wish to thank Mr. Mitja Jerlah (from the HYB Company) for producing the test sensors.

Literature

/1./ M. Prudenziati, editor, Handbook of Sensors and Actuators, vol. 1: Thick film sensors, Elsevier, 1994.

/2./ N.M. White, J.D. Turner, Thick film sensors: past, present and future. Meas. Sci. Technol. 8, 1-20 (1997)

/3./ K. A. Peterson, K. D. Patel. C. K. Ho, S. B. Rohde, C. D. Nordquist, C. A. Walker, B. D. Wroblewski, M. Okandan, Novel microsystem applications with new techniques in low-temperature

co-fired ceramics, Int. J. Appl. Ceram. Technol., 2, (5), (2005), 345-363

/4./ R. Puers, "Capacitive sensors: when and how to use them", Sensors and Actuators A, 37-38 (1993) 93-105

/5./ W. Bracke, R. Puers, C. Van Hoof, Ultra Low power Capacitive Sensor Interfaces Springer 2007.

/6./ C. B. Sippola, C. H. Ahn, "A thick film screen-printed ceramic capacitive pressure microsensor for high temperature applications", Journal of Micromechanics and Microengineering, Vol.16, pp. 1086-1091, 2006.

/7./ M.G.H Meijernik, E. Nieuwkoop, E.P. Veninga, M.H.H. Meuwissen, M.W.W.J. Tijdink, "Capacitive pressure sensor in post-processing on LTCC substrates", Sensors and Actuators A, 123-124, 2005, 234-239

/8./ S. T. Moe, K. Schjolberg-Henriksen, D. T. Wang, E. Lund, J. Nysaether, L. Furuberg, M. Visser, T. Fallet, R.W. Berstein, Capacitive differential pressure sensor for harsh environments, Sensors and Actuators (2000) 30-33.

/9./ G. Blasquez, X Chauffleur, P. Pons, C. Douziech, P. Favaro, Ph. Menini, Intrinsic thermal behaviour of capacitive pressure sensors: mechanisms and minimisation, Sensors and Actuators 85 (2000) 56-69.

/10./ L. K. Baxter, Capacitive Sensors, copyright 6-26-00, http://www.capsense.com/capsense-wp.pdf

/11./ Winncy Y. Du, Scott W. Yelich, Resistive and Capacitive Based Sensing Technologies, Sensors & Transducers, ISSN 1726-5479, 2008, IFSA, http://www.sensorsportal.com/HTML/DIGEST/P_SI_29.htm

/12./ S. R. Norsworthy, R. Schreier, G. C. Temes, *"Delta-Sigma Data Converters"* IEEE Press, 1997, Wiley-IEEE Press, ISBN: 978-0780310452

/13./ J. C. Candy, G. C. Temes, "Oversampling Delta-Sigma data converters", IEEE Press, Publisher: Wiley-IEEE Press, 2008, ISBN: 978-0879422851

/14./ O'Dowd, J. Callanan, A. Banarie, G. Company-Bosch, E "Capacitive sensor interfacing using sigma-delta techniques" *Sensors*, 2005 IEEE, pp.-951-954, ISBN: 0-7803-9056-3, Digital Object Identifier: 10.1109/ICSENS.2005.1597858

/15./ M. Bingesser, Teddy Loeliger, Werner Hinn, Johann Hauer, Stefan Mödl, Robert Dorn, Matthias Völker "Low-noise sigma-delta capacitance-to-digital converter for Sub-pF capacitive sensors with integrated dielectric loss measurement" *Proceedings of the conference on Design, automation and test in Europe,* Munich, Germany, 2008, pp. 868-872.

/16./ Analog Devices AD7746 Evaluation Board - EVAL-AD7746EB, Revision 0, May 2005. Available on: http://www.analog.com/static/imported-files/eval_boards/252730993EVAL_AD7746EB_0.pdf

/17./ S. Pratt "Environmental Compensation on the AD7142: The Effects of Temperature and Humidity on Capacitance Sensors" Analog Devices Application Note AN-829, 2005. http://www.analog.com/static/imported-files/application_notes/577315308337353595863 3AN829_0.pdf

/18./ D. Belavič, M. S. Zarnik, M. Hrovat, S. Maček, M. Kosec, "Temperature behaviour of capacitive pressure sensor fabricated with LTCC technology" *Inf. MIDEM, 2009*, vol. 38, no. 3, pp. 191-196.

/19./ IEEE Std. 1451.2 D3.05-Aug1997 "IEEE standard for a smart transducer interface for sensors and actuators - Transducer to microprocessor communication protocols and transducer electronic data sheet (TEDS) formats" Institute of Electrical and Electronics Engineers, September 1997.

Marina Santo Zarnik[1], Matej Možek[2], Srečko Maček[3], Darko Belavič[1]

[1]HIPOT-RR d.o.o., 8222 Otočec, Slovenia
[2]Faculty of Electrical Engineering, 1000 Ljubljana, University of Ljubljana, Slovenia
[3]Jožef Stefan Institute, 1000 Ljubljana, Slovenia

Prispelo (Arrived): 10.11.2009 *Sprejeto (Accepted): 09.03.2010*

Informacije MIDEM
Strokovna revija za mikroelektroniko, elektronske sestavine dele in materiale

NAVODILA AVTORJEM

Informacije MIDEM je znanstveno-strokovno-društvena publikacija Strokovnega društva za mikroelektroniko, elektronske sestavne dele in materiale - MIDEM. Revija objavlja prispevke s področja mikroelektronike, elektronskih sestavnih delov in materialov. Ob oddaji člankov morajo avtorji predlagati uredništvu razvrstitev dela v skladu s tipologijo za vodenje bibliografij v okviru sistema COBISS.
Znanstveni in strokovni prispevki bodo recenzirani.

Znanstveno-strokovni prispevki morajo biti pripravljeni na naslednji način:

1. Naslov dela, imena in priimki avtorjev brez titul, imena institucij in firm
2. Ključne besede in povzetek (največ 250 besed).
3. Naslov dela v angleščini.
4. Ključne besede v angleščini (Key words) in podaljšani povzetek (Extended Abstract) v angleščini, če je članek napisan v slovenščini
5. Uvod, glavni del, zaključek, zahvale, dodatki in literatura v skladu z IMRAD shemo (Introduction, Methods, Results And Discsussion).
6. Polna imena in priimki avtorjev s titulami, naslovi institucij in firm, v katerih so zaposleni ter tel./Fax/Email podatki.
7. Prispevki naj bodo oblikovani enostransko na A4 straneh v enem stolpcu z dvojnim razmikom, velikost črk namanj 12pt. Priporočena dolžina članka je 12-15 strani brez slik.

Ostali prispevki, kot so poljudni cčlanki, aplikacijski članki, novice iz stroke, vesti iz delovnih organizacij, inštitutov in fakultet, obvestila o akcijah društva MIDEM in njegovih članov ter drugi prispevki so dobrodošli.

Ostala splošna navodila

1. V članku je potrebno uporabljati SI sistem enot oz. v oklepaju navesti alternativne enote.
2. Risbe je potrebno izdelati ali iztiskati na belem papirju. Širina risb naj bo do 7.5 oz.15 cm. Vsaka risba, tabela ali fotografija naj ima številko in podnapis, ki označuje njeno vsebino. Risb, tabel in fotografij ni potrebno lepiti med tekst, ampak jih je potrebno ločeno priložiti članku. V tekstu je treba označiti mesto, kjer jih je potrebno vstaviti.
3. Delo je lahko napisano in bo objavljeno v slovenščini ali v angleščini.
4. Uredniški odbor ne bo sprejel strokovnih prispevkov, ki ne bodo poslani v dveh izvodih skupaj z elektronsko verzijo prispevka na disketi ali zgoščenki v formatih ASCII ali Word for Windows. Grafične datoteke naj bodo priložene ločeno in so lahko v formatu TIFF, EPS, JPEG, VMF ali GIF.
5. Avtorji so v celoti odgovorni za vsebino objavljenega sestavka.

Rokopisov ne vračamo. Rokopise pošljite na spodnji naslov.

Uredništvo Informacije MIDEM
MIDEM pri MIKROIKS
Stegne 11, 1521 Ljubljana, Slovenia
Email: Iztok.Sorli@guest.arnes.si
tel. (01) 5133 768, fax. (01) 5133 771

Informacije MIDEM
Journal of Microelectronics, Electronic Components and Materials

INSTRUCTIONS FOR AUTHORS

Informacije MIDEM is a scientific-professional-social publication of Professional Society for Microelectronics, Electronic Components and Materials - MIDEM. In the Journal, scientific and professional contributions are published covering the field of microelectronics, electronic components and materials.
Authors should suggest to the Editorial board the classification of their contribution such as : original scientific paper, review scientific paper, professional paper...
Scientific and professional papers are subject to review.

Each scientific contribution should include the following:

1. Title of the paper, authors' names, name of the institution/company.
2. Key Words (5-10 words) and Abstract (200-250 words), stating how the work advances state of the art in the field.
3. Introduction, main text, conclusion, acknowledgements, appendix and references following the IMRAD scheme (Introduction, Methods, Results And Discsussion).
4. Full authors' names, titles and complete company/institution address, including Tel./Fax/Email.
5. Manuscripts should be typed double-spaced on one side of A4 page format in font size 12pt. Recommended length of manuscript (figures not included) is 12-15 pages
6. Slovene authors writing in English language must submit title, key words and abstract also in Slovene language.
7. Authors writing in Slovene language must submit title, key words and extended abstract (500-700 words) also in English language.

Other types of contributions such as popular papers, application papers, scientific news, news from companies, institutes and universities, reports on actions of MIDEM Society and its members as well as other relevant contributions, of appropriate length , are also welcome.

General informations

1. Authors should use SI units and provide alternative units in parentheses wherever necessary.
2. Illustrations should be in black on white paper. Their width should be up to 7.5 or 15 cm. Each illustration, table or photograph should be numbered and with legend added. Illustrations, tables and photographs must not be included in the text but added separately. However, their position in the text should be clearly marked.
3. Contributions may be written and will be published in Slovene or English language.
4. Authors must send two hard copies of the complete contributon, together with all files on diskette or CD, in ASCII or Word for Windows format. Graphic files must be added separately and may be in TIFF, EPS, JPEG, VMF or GIF format.
5. Authors are fully responsible for the content of the paper.

Contributions are to be sent to the address below.

Uredništvo Informacije MIDEM
MIDEM pri MIKROIKS
Stegne 11, 1521 Ljubljana, Slovenia
Email: Iztok.Sorli@guest.arnes.si
tel.+386 1 5133 768, fax.+386 1 5133 771